ALMA MATER STUDIORUM - UNIVERSITA' DI BOLOGNA

DEIS - DIPARTIMENTO DI ELETTRONICA, INFORMATICA E SISTEMISTICA

DOTTORATO DI RICERCA IN INGEGNERIA ELETTRONICA, INFORMATICA E DELLE TELECOMUNICAZIONI

CICLO XXIII - ING-INF/01

Numerical Study of Graphene as a Channel Material for Field-Effect Transistors

Tesi di Dottorato

Presentata da Roberto Grassi

Coordinatore del Corso di Dottorato:

Chiar.ma Prof.ssa Ing. PAOLA MELLO

Relatore:

Chiar.mo Prof. Ing. MASSIMO RUDAN

Esame Finale: anno 2011

Contents

Abstract

Graphene, a monolayer of carbon atoms arranged in a honeycomb lattice, has been isolated only recently from graphite. This new material presents ideal properties that make it a promising candidate for building future nano-electronic devices. The fact that carrier moves inside it almost without scattering and its atomic thickness suggest that field-effect transistors (FETs) made of graphene as channel material would be faster and less affected by short-channel effects than their silicon counterparts.

However, there is a major obstacle for the application of graphene in electronics: the absence of a band gap. Digital transistors requires a band gap for closing the conductive channel when the device is in the off state. Graphene, instead, has a zero band gap, leading to a very limited on/off current ratio.

Several ways have been proposed in the literature to open a band gap in graphene. In this thesis, two of these ideas are studied by means of numerical simulations: graphene nanoribbons (GNRs) and hydrogenated graphene.

Graphene nanoribbons are narrow strips of graphene, where a band gap is induced by the quantum confinement of carriers in the lateral dimension. The experimental GRN-FETs are still far from being ideal, mainly due to the large width and to edge roughness, thus numerical studies are needed to evaluate their theoretical performance. A code is developed for this purpose. Due to the importance of capturing quantum effects in the operation of graphene devices, a full-quantum transport model is employed: the electron dynamics is described by a tight-binding (TB) Hamiltonian model and transport is solved within the formalism of the non-equilibrium Green's functions (NEGF). Furthermore, two simplified approaches, the non-parabolic effective mass (NPEM) model and the mode-space tight-binding (MS TB) method, are developed to reduce the computational times and thus allow intensive simulation tasks. The code is used for simulation studies of two different architectures: conventional and tunneling FETs. The simulations show the great potential of conventional narrow GNR-FETs, but highlight at the same time the leakage problems in the off-state due to various tunneling mechanisms. The leakage problems become more severe as the

width of the devices is made larger, and thus the band gap smaller, resulting in a poor on/off current ratio. The tunneling FET architecture can partially solve these problems thanks to the improved subthreshold slope; however, it is also shown that edge roughness, unless well controlled, can have a detrimental effect in the off-state performance.

The second part of this thesis deals with hydrogenated graphene. The chemical modification of the graphene surface is one of the method currently under study to modify the graphene electronic band structure. In particular, it is known that fully hydrogenated graphene behaves likes an insulator. This suggests the idea of creating a regular pattern, i.e. a superlattice, of hydrogen clusters on the graphene surface: in this way, the hydrogenated regions will act as a confinement potential for the graphene regions left uncovered. A recent experiment has shown that such a patterned hydrogenation is possible for graphene grown on an iridium substrate. Here, pattern-hydrogenated graphene is simulated by means of a TB model. A model for hydrogenation that mimics the preferential asdorption observed experimentally, including disorder, is developed. The results of a novel calculation, generalizing the usual band structure analysis to disordered structures, confirm the band gap opening measured by angle-resolved photoemission spectroscopy (ARPES) and give indications about the scaling of the band gap as a function of the key engineering parameters, i.e. the size of the superlattice unit cell and the size of the hydrogen cluster. Due to disorder, states located inside the gap region are observed. Transport simulations of the conductance of finite samples allow to understand the transport mechanism through both the gap and the band states.

Chapter 1

Introduction

In this short chapter, graphene is introduced and its main properties are summarized (Sect. 1.1). The emphasis is placed on the bandgap problem, which is an outstanding technological bottleneck for the application of graphene in nanoelectronics. Exploring through numerical simulations possible solutions to this problem is the main motivation for this thesis. A brief introduction is also given to the modeling tools that can be used to describe charge transport in graphene in an atomistic and quantum-mechanical way (Sect. 1.2).

1.1 Graphene properties and band gap problem

Graphene is a monolayer of carbon atoms arranged in a honeycomb lattice, as shown in Fig. 1.1. Graphene is the building block of graphite, which can be viewed as a stack of weakly bonded graphene layers. Also, carbon nanotubes (CNTs) can be regarded as originating from a graphene sheet that is rolled around an axis. Therefore, graphene properties have been theoretically known for a long time [1]. However, until recently, it was believed that graphene, as well as all 2D crystals, could not exist in a stable state due to thermodynamic arguments. In a famous experiment carried out in 2004, a research team at Manchester University demonstrated for the first time the possibility of isolating graphene layers from graphite [2]. The employed technique was based on a repetitive exfoliation of a graphitic block using adhesive tape and the subsequent deposition of the flakes onto an oxidized silicon wafer. Graphene layers were then identified by using an optical contrast technique and patterned for electrical characterization. Although the samples studied in the first paper [2] were not true single-layer but few-layer graphene, the paternity of graphene is commonly attributed to the authors of [2]: A. Geim and K. Novoselov have received the 2010 Nobel Prize in physics for their work on graphene. Single-layer graphene was subsequently characterized,

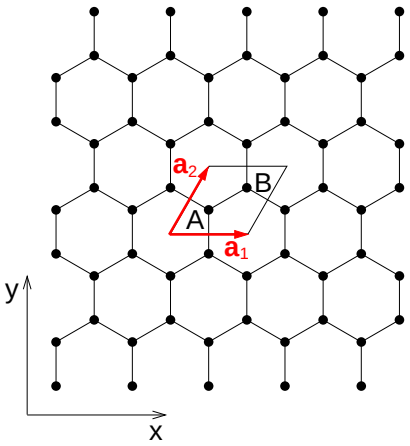

Figure 1.1: Graphene honeycomb lattice: $\mathbf{a}_1$ and $\mathbf{a}_2$ are the primitive lattice vectors; the unit cell, made of an A and B atom, is highlighted.

revealing its unique properties [3, 4].

Other techniques to fabricate graphene have been developed during the subsequent years: epitaxial growth on top of silicon carbide has been first proposed as a method to obtain large areas of graphene, as needed by electronic applications [5]; recently, the chemical vapor deposition of graphene on metal substrates like nickel and copper, followed by the transfer on insulating substrates, has emerged as a viable process to obtain high-quality graphene sheets of arbitrary size [6].

Graphene properties have been first reviewed in [7]. Here, the more interesting properties for the application in nanoelectronics are shortly summarized. As already said, graphene is a pure 2D crystal with atomic thickness. Hence, it is an ideal material for use in electronics: the monolayer thickness ensures a very good control of short channel effects in transistor applications and also makes graphene a promising material for flexible electronics. However, the most intriguing property is perhaps the exceptionally high carrier mobility that has been measured in graphene. Values as large as 10,000 $\mathrm{cm}^2/\mathrm{Vs}$ have been obtained with a very weak temperature dependence: this indicates that a very low concentration of impurities and defects is present in graphene and limiting the mobility, while electron-phonon interactions are strongly suppressed. As a consequence, the electron mean free path in graphene has been estimated to be in the order of one micrometer: this make it possible to fabricate graphene devices operating in the ballistic regime, i.e. where electrons can move from a source to a drain contact without suffering from scattering. An excellent switching speed is expected for these devices. In addition, graphene can sustain high current densities exceeding those of copper at comparable dimensions: therefore, it can also be employed for the fabrication of low-resistance interconnects.

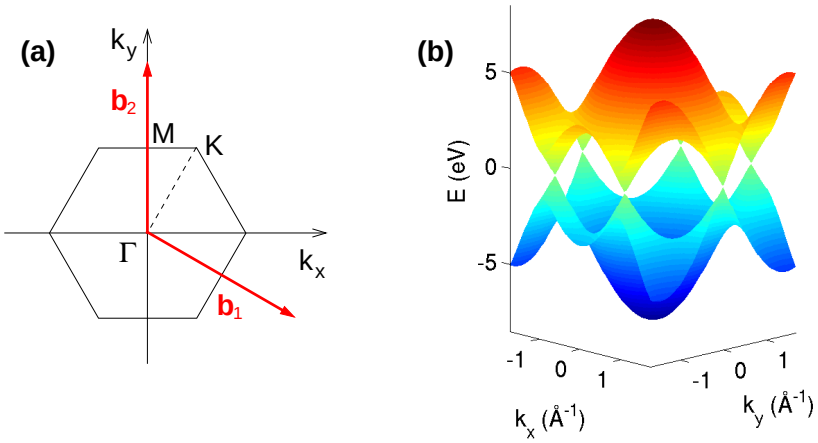

Figure 1.2: (a) Graphene Brillouin zone: $\mathbf{b}_1$ and $\mathbf{b}_2$ are the primitive vectors of the reciprocal lattice. (b) Graphene bandstructure from the simple TB model in (B.30) with $\gamma = -2.6$ eV.

However, graphene is not an ordinary semiconductor, but a semimetal (or zero gap semiconductor). A good description of the dispersion relation in graphene around the charge neutrality point (i.e. intrinsic Fermi level) can be obtained with the simple tight-binding (TB) model presented in the next section. The resulting bandstructure is plotted in Fig. 1.2 together with the indication of the graphene Brillouin zone. The bandstructure is made of a valence and a conduction band which intersect which each other at the K points of the Brillouin zone*. Under charge neutrality conditions, the Fermi level is at the intersection energy, but can be shifted with the application of a vertical electric field to create a majority of holes or electrons. The dispersion relation around each K point can be well approximated by a conical surface up to at least 1 eV. Besides, being the graphene lattice formed of two sublattices A and B, its wavefunction has two components (pseudo-spin). As a result of these two properties, the effective mass Hamiltonian describing the electron dynamics in graphene at low energies is analogous to the one of massless Dirac fermions in relativistic quantum mechanics, but with the spin being replaced by the pseudo-spin and the speed of light being replaced by the Fermi velocity. This analogy leads to many intriguing physical phenomena, which have been experimentally verified after the isolation of graphene.

Due to the absence of a bandgap, graphene is not suitable for use in nanoelectronic devices such as field-effect transistors (FETs). Even if the conductivity of graphene can be modulated by an applied electric field, the absence of a bandgap leads to very a very small on/off current ratio (tipically around 10). One of the

*In Fig. 1.2, the conduction and valence bands are perfectly symmetrical to each other. This is an effect of the adopted TB model. More realistic models result in an asymmetry at high energies.

main problem in graphene research is thus to find a successful method to open a bandgap in graphene. Several ways have been proposed in the literature.

For instance, the patterning of graphene nanoribbons (GNRs), i.e. narrow strips of graphene, induces a bandgap due to the confinement of carriers along the transversal direction. Graphene nanoribbons have been obtained using either lithographic etching [8] or chemical processes [9]. Theoretical calculations predict that the energy gap of GNRs depends on its specific orientation [10]. GNRs can be classified in either zigzag or armchair depending on the shape of their edges: if the edges are oriented along a zigzag direction (such as the x one in Fig. 1.1), the GNR is always metallic; instead, if the edges are along an armchair direction (such as the y one in Fig. 1.1), the GNR is semiconducting with a width-dependent gap. Interestingly, a bandgap, inversely proportional to the nanoribbon width, is always observed in the experiments, irrespective of the orientation [11]. GNR FETs with widths ranging from several tens of nanometers down to 2 nm have been fabricated and experimentally characterized, demonstrating the possibility of achieving high on/off ratios [9]. The obtained results, however, are still far from satisfactory: the devices are affected by edge roughness, due to the difficulty of achieving a good edge control, and metallic contacts are used as source/drain regions, due to the lack of a successful technique for doping graphene. Also, the large scale fabrication of nanoribbons remains a challenge.

Another method for opening a bandgap in graphene is by modifying its electronic structure by chemically attaching different atoms or molecules to its surface. The hydrogenation of graphene is of particular interest. By angle-resolved photoemission spectroscopy (ARPES), A recent experiment has shown that a bandgap is induced in graphene grown on an iridium substrate, after the exposure to hydrogen atoms [12]. Thanks to the presence of the substrate, a regular pattern of hydrogen clusters is formed on the graphene surface, leading to a confinement effect similar to the one in GNRs.

While several other methods for opening a bandgap have been proposed, as for example graphene bilayer [13] or strained graphene [14], only GNRs and pattern-hydrogenated graphene are considered in this thesis. Numerical simulations are performed to study the performance of GNR-FETs as well as the electronic and transport properties of pattern-hydrogenated graphene.

1.2 State-of-the-art modeling techniques

The tight-binding (TB) Hamiltonian model, treated within the non-equilibrium Green's functions (NEGF) formalism, represents the state-of-the-art model for the quantum and atomistic description of transport in graphene-related materials. A full-quantum transport model is needed to accurately describe the operation of GNR-FETs in the subthreshold region, where different tunneling mechanisms

dominate transport [15, 16]. Also, an atomistic Hamiltonian is required to capture atomistic details of the graphene structure, such as irregular edges in nanoribbons or the bonding with hydrogen atoms in pattern-hydrogenated graphene.

1.2.1 Tight-binding model

In the TB method, a discrete representation is used [17]. A discrete basis is formed by selecting a certain number of atomic orbitals for each atom of the structure under consideration. If the structure is periodic, one can label these orbitals as $|\mathbf{l}, q\rangle$, where $\mathbf{l}$ is the lattice vector and q the orbital index inside each unit cell. The Hamiltonian then is represented as a matrix, whose matrix elements

$$\langle \mathbf{l}_1, q_1 | H | \mathbf{l}_2, q_2 \rangle \,. \tag{1.1}$$

are the hopping integrals between orbital pairs. Instead of explicitly calculating these matrix elements, that is by taking into account the Coulomb potential generated by each atom and the expression of the atomic orbitals, the TB method treats them as parameters, which can be fitted against experimental data or the results of first-principle models. The following approximations are usually done to reduce the number of parameters: (i) three-center integrals are neglected, i.e. when evaluating the matrix element between an orbital in atom A and an orbital in atom B, the effect of a third atom C is neglected; (ii) orbitals on different atoms are considered orthogonal; (iii) coupling is limited to orbitals on nearest-neighbor atom pairs.

For carbon-based material, a good basis is obtained by selecting the $2s$, $2p_x$, $2p_y$, and $2p_z$ orbitals, which are the ones occupied by valence electrons [1]. For graphene though, due the planar geometry, the $2p_z$ orbitals turn out to be completely decoupled from the other ones. The bands associated to the $2p_z$ orbitals are the ones that are close to the neutrality point and thus responsible for conduction. The basis made of one $2p_z$ orbital per carbon atom is thus sufficient. By applying the approximations listed above, only one parameter remains, the one that describes the coupling between nearest-neighbor $2p$ orbitals, oriented as in Fig. 1.3 (the onsite energy, i.e. the matrix element calculated between an

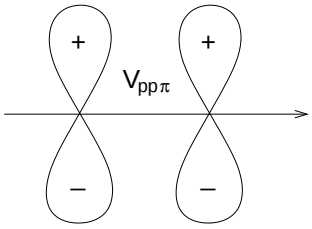

Figure 1.3: Schematic representation of the hopping integral between $2p_z$ orbitals in graphene.

orbital and itself is the energy reference). Within this model, the bandstructure of graphene associated to the $2p_z$ orbitals (π and π^* bands) can be obtained by solving a simple 2×2 eigenvalue problem (see Eq. B.30). The result is plotted in Fig. 1.2. It is interesting to notice that the absence of bandgap is related to the symmetry between the two graphene sublattices: if the onsite energies of the A and B atom were different, the calculated bandstructure would show an energy gap between the π and π^* bands. This symmetry breaking, for example, is responsible for the bandgap opening in bilayer graphene under an applied perpendicular electric field.

1.2.2 Non-equilibrium Green's functions formalism

The NEGF formalism provides a microscopic theory for quantum transport [18]. A detailed introduction to Green's functions would require the use of complicated formalisms, such as Fock space and the language of second quantization, which are commonly used in many-body theory [19] but are beyond the scope of this introduction. Here, the different quantities are simply listed and their physical meaning is explained. A detailed description of the solution scheme is given in Sec. 2.1.

The NEGF formalism can be seen as the quantum analogue of the Boltzmann equation. While Boltzmann's equation combines Newton's law with a statistical description of interactions, the NEGF formalism combines quantum dynamics with an analogous description of interactions. Steady-state transport is considered here.

In the semiclassical case of Boltzmann's equation, the electrons are described by a function $f(\mathbf{r};\mathbf{k})$, which gives the number of electrons in each single-particle state (r is the position and $\mathbf{k}$ the momentum over $\hbar$). In the quantum case, instead one has a number of Green's functions: $G^{r/a/</>}(\mathbf{r},\mathbf{r}';E)$ (E is the electron energy). It should be noticed that each of these quantities depends on two position variables: in the TB description, $\mathbf{r} \to (\mathbf{l}, q)$ and thus each of the above quantities, at fixed E, becomes a square matrix as the Hamiltonian, with a size equal to the total number of orbitals. The diagonal terms of the Green's functions have a similar meaning to the semiclassical distribution function, as they are related to the population of one-particle states. On the other hand, phase correlations, which give rise to quantum interference effects, are contained in the off-diagonal terms.

The different Green's functions are not all independent from each other. Introducing the matrix notation $G^{r/a/</>}(E)$ and dropping for simplicity the dependence on energy, one has the following relations:

$$G^a = G^{r\dagger}\,, \tag{1.2}$$

$$\mathrm{i}(G^r - G^a) = \mathrm{i}(G^> - G^<)\,. \tag{1.3}$$

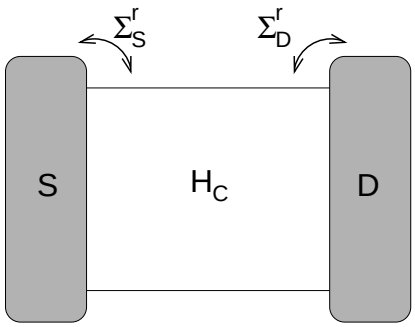

Figure 1.4: Schematic representation of the interaction model between the device region and the leads.

The quantity at the LHS of (1.3) is called the spectral function $A = \mathrm{i}(G^r - G^a)$: its diagonal elements give the density of available states at each single particle state (i.e the local density of states or LDOS). The two quantities at the RHS, $\mathrm{i}G^>$ and $-\mathrm{i}G^<$, have a similar meaning, but for empty and occupied states, respectively. Therefore, the diagonal entries of (1.3) can also be read as

$$\#\text{ available states} = \#\text{ empty states} + \#\text{ occupied states}\,. \tag{1.4}$$

The use of different types of Green's function is needed to account for the antisymmetry of electrons: Pauli's exclusion principle is already contained in (1.3).

As far as scattering terms are concerned, these are represented by self-energies $\Sigma^{r/a/</>}$ (again matrix notation is used and energy dependence is dropped), which are completely analogous to their Green's functions counterparts:

$$\Sigma^a = \Sigma^{r\,\dagger}\,, \tag{1.5}$$

$$\mathrm{i}(\Sigma^r - \Sigma^a) = \mathrm{i}(\Sigma^> - \Sigma^<)\,. \tag{1.6}$$

The quantity $\Gamma = \mathrm{i}(\Sigma^r - \Sigma^a)$ is related to the rate of loss of electrons due to scattering, while $\mathrm{i}\Sigma^>$ and $-\mathrm{i}\Sigma^<$ to the rate of out-scattering and in-scattering of electrons, respectively. Again, these functions take into account phase correlations and antisymmetry.

The Green's functions satisfy the equations

$$G^r = \left[(E + \mathrm{i}0^+)I - H_C - \Sigma^r\right]^{-1}\,, \tag{1.7}$$

$$G^{</>} = G^r \Sigma^{</>} G^a\,. \tag{1.8}$$

It is interesting to note that if Σ^r is not Hermitian, the resultant effective Hamiltonian $H + \Sigma^r$ is not Hermitian either: this situation corresponds to a loss of particles, in accordance with the meaning attributed to Γ.

In conclusion, it has to be pointed out that the self-energies can describe as well the effect of leads which are attached to a device region, as shown in Fig. 1.4.

Indeed, in this thesis, incoherent scattering mechanisms are not considered, so the self-energies due to leads are the only relevant ones.

Part I

GRAPHENE NANORIBBON FETs

Chapter 2

Efficient modeling and solution approaches for GNR FET simulation

As already discussed in Sect.1.2, the TB Hamiltonian combined with the NEGF formalism provides the state-of-the-art model for describing quantum transport in carbon related materials. Since it uses atomic orbitals as basis functions, it can take into account the precise atomic structure of the material and thus also describe the effect of atomistic defects, such as irregular edges in GNRs. However, this deep physical insight is achieved at the expense of long computational times, which are not practical for device optimization studies.

Here, two simplified approaches are presented for the simulation of transport in armchair GNR devices. They both exploit the fact that a graphene nanoribbon behaves as a confined structure in the transverse direction: due to confinement, the 2D graphene dispersion relation splits up in many 1D subbands, whose separation in energy increases as the width of the GNR is decreased. If the subband index is a good quantum number, i.e. if the electrons travel through the device without changing subband, a large computational advantage can be achieved by considering a separate transport problem for each subband and by simulating only those subbands that lie in the energy window under interest. This is the idea behind the two methods that are presented here.

The first method, called non-parabolic effective mass (NPEM), makes the assumption that each conduction subband is only coupled to its symmetrical valence subband. An eigenvalue problem that uses the TB Hamiltonian is solved for each unit cell of the device, in order to find the energy extremum of each subband, as well as the corresponding eigenvector. Then, a 1D NEGF problem

along the longitudinal direction is set up for the lowest pairs of conduction and valence subbands, by using an effective mass Hamiltonian, where the effective mass is made dependent on the electron kinetic energy to account for the non-parabolicity of the subband dispersion relation. Although this method is not completely rigorous, it is shown to have a good accuracy in all the different operating regions of the device.

A second method, called mode-space tight-binding (MS TB), has been developed to rigorously treat the separation of the transport problem in the transverse and longitudinal directions and the coupling between different subbands. As similar methods in the literature, it relies on a change of representation from real space (RS), where the unknown functions and the Hamiltonian are expressed in terms of atomic orbitals, to mode space (MS), where the basis is instead made of a convenient subset of the transverse eigenvectors, that is modes. The novelty of the method presented here consists in a numerical slab-by-slab calculation of the modes and a novel algorithm to evaluate the coupling bewteen them, and thus to identify the modes that need to be treated as coupled in the transport calculation. For ribbons with smooth edges, the method gives almost exact results. Its applicability to irregular GNRs is also discussed.

The chapter is organized as follows. Sect. 2.1 describes the RS solution of the TB model, which is used as a benchmark to evaluate the accuracy of the two simplified approaches. The NPEM method is presented in Sect. 2.2, while the MS TB in Sect. 2.3.

2.1 Benchmark model: real space tight-binding

In this section, the adopted TB model for GNRs is introduced and the general procedure for solving the NEGF equations in real space is summarized.

Before entering into the details of the model, it is usefel to clarify the physical structure under study. This is represented in Fig. 2.1-top. A GNR of the armchair type is used as the channel material of an FET. The ribbon is sandwiched between two oxide layers and the electrostatic potential over it is modulated by the field-effect of one or two gate contacts. The source and drain ends of the GNR are assumed to be doped and to be connected to two semi-infinite leads, made of the same GNR as the device region. The two leads are conceptually supposed to be connected to two large contacts that maintain them in equilibrium. Therefore, the particles injected from each of the two leads into the device can be described by an equilibrium Fermi distribution. However, the Fermi levels of the source and drain leads, E_{FS} and E_{FD}, are in general different: their difference is equal, apart from the electronic charge q, to the applied voltage V_{DS}. The purpose of the simulation is to compute the current I_{DS} that flows from source to drain as a function of the applied voltages V_{DS} and V_{GS}, in a steady-state condition.

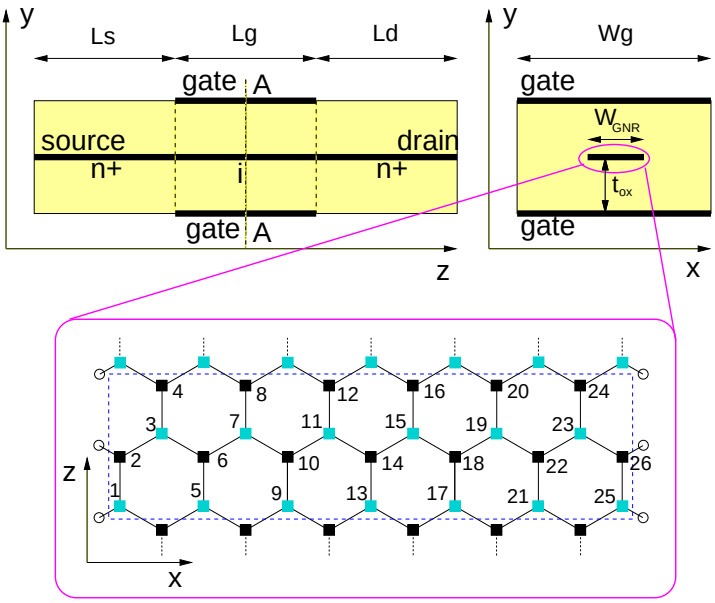

Figure 2.1: Top: longitudinal (left) and transverse (right) cross-section of the reference GNR device. A double-gate geometry with gate-aligned source and drain regions is shown only as an example: the actual structure can be different. Bottom: one-dimensional elementary cell or slab of an $N_a = 13$ armchair GNR.

Charge transport is assumed to occur only inside the GNR. This can be viewed as a periodic structure along the longitudinal direction z: for an armchair ribbon, the unit cell or slab is made of two rows of dimers and its length is equal to $\Delta z = 3a_{\mathrm{CC}}$, with $a_{\mathrm{CC}} = 1.42$ Å the carbon interatomic distance. For reference, a slab taken from an $N_a = 13$ armchair GNR, with N_a equal to the number of dimers, is shown in Fig. 2.1-bottom.

The TB Hamiltonian is introduced to quantum-mechanically describe the electron dynamics inside the GNR. A a set of orthogonal p_z orbitals, one for each carbon atom, is in general sufficient to describe transport in graphene-related materials. Indicating with $|l, \alpha\rangle$ the orbital associated with the atom α within the slab l, the generic matrix element of the Hamiltonian is written as

$$\langle l, \alpha | H | m, \beta \rangle \equiv H_{l\alpha,m\beta} = t_{l\alpha,m\beta} + \delta_{l\alpha,m\beta} U_{l\alpha} \ , \tag{2.1}$$

where $\delta_{l\alpha,m\beta}$ is the Kronecker delta and $U_{l\alpha}$ is the electrostatic potential energy at the (l, α) atom site. For graphene, one can obtain an accurate model by simply setting the $t_{l\alpha,m\beta} = t_1$ if the atoms (l, α) and (m, β) are first nearest neighbor (1NN), while $t_{l\alpha,m\beta} = 0$ otherwise (the value $t_1 = -2.6$ eV is tipically used). However, it has been demonstrated in [20], that, when applied to armchair GNRs, this model does not correctly take into account the effect of the edge terminations, resulting in a bad estimation of the energy gap. In the same paper,

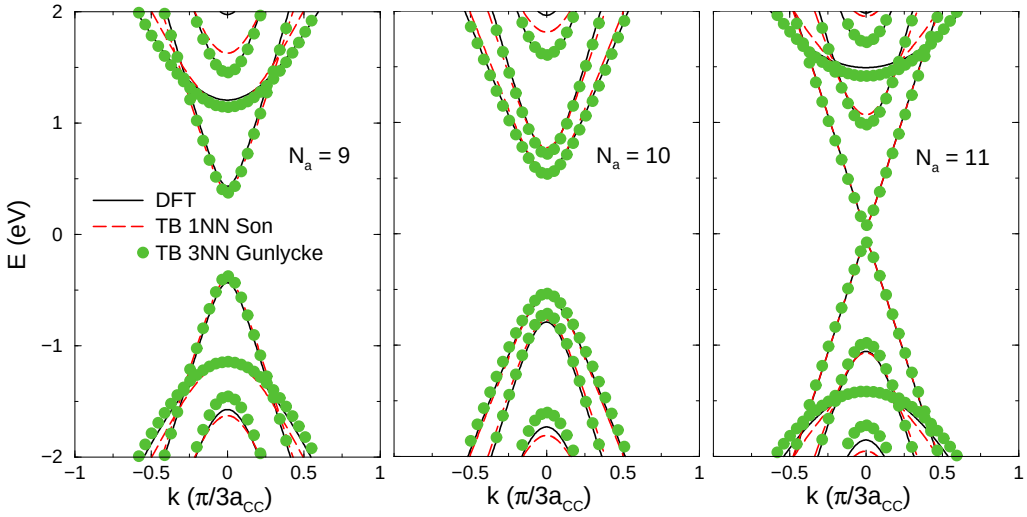

Figure 2.2: Energy dispersion relationship vs. wavevector normalized to the slab length $3a_{CC}$, for three different armchair GNRs corresponding to (from left to right) $N_a = 9, 10, 11$. Three models are compared: DFT (the author is grateful to Dr. Blanca Biel for providing this data), TB with first nearest-neighbor interactions and parameters from [20], TB with interactions up to third nearest-neighbor atoms and parameters from [21].

a simple correction of the model has been suggested to describe the passivation of the edges by hydrogen atoms: $t_{l\alpha,m\beta} = t_1$ for the internal 1NN atom pairs and $t_{l\alpha,m\beta} = t_1(1 + \delta_1)$ for the 1NN atom pairs along the edges of the GNR (with values $t_1 = -2.7$ eV and $\delta_1 = 0.12$). A more refined model, additionally setting $t_{l\alpha,m\beta} = t_3$ for third nearest-neighbor (3NN) atom pairs (with values $t_1 = -3.2$ eV, $\delta_1 = 0.0625$, $t_3 = -0.3$ eV), has also been proposed in the literature [21].

Bandstructure calculations have been performed to check the validity of the 1NN model with edge correction and of the 3NN model. Since the ribbon is a periodic structure in just one dimension, its bandstructure is one-dimensional. Denoting with $H_{l,m}$ the submatrix of H relative to the (l, m) pair of slabs, the dispersion relation $E(k)$, with k the longitudinal wavevector, can be obtained by solving the eigenvalue problem

$$\left(H_{l,l} + H_{l,l+1}e^{\mathrm{i}k\Delta z} + H_{l,l+1}^{\dagger}e^{-\mathrm{i}k\Delta z}\right) v = Ev\,, \tag{2.2}$$

where $U_{l\alpha}$ is set identically equal to zero. Since the size of the matrix in parenthesis is $2N_a \times 2N_a$, the equation gives $2N_a$ bands. These bands are called "subbands" to highlight the fact that they physically originate from the quantization of the same conduction or valence band of bulk graphene. Fig 2.2 compares the bandstructure resulting from the two TB models with the result of a DFT [22]

calculation. Three GNRs with different width are considered, corresponding to the three cases $N_a = 3n$, $N_a = 3n + 1$ and $N_a = 3n + 2$, with integer n. As is well known in the literature [20], the three families give rise to very different bandstructures, even if the GNRs differ from each other for just one atomic row. It can be seen that, for all the three values of N_a, the energy gaps and the shape of the first two subband pairs around the extrema are well reproduced by both TB models. Some discrepancies are detected at higher energies, which should be not so important for the device electrical characteristics. Furthermore, it is interesting to note that both TB models preserve the simmetry between the two graphene sublattices, resulting in conduction and valence subbands that are symmetric with each other. Unless otherwise stated, the simulations presented here are carried out with the 1NN model.

In the RS approach, the transport problem is formulated within the NEGF formalism [18, 23] using the Hamiltonian described above. The retarded Green's function G^r at the energy E is defined by $AG^r = I$, where $A = (E + \mathrm{i}\eta)I - H$, being η an infinitesimal positive quantity (the quantity A should not be confused with the spectral function, for which the same symbol is used elsewhere in this thesis). This matrix equation is of infinite dimension because it describes the entire structure made of the device region plus the two semi-infinite source and drain leads:

$$\begin{pmatrix} A_S & A_{SC} & 0 \\ A_{CS} & A_C & A_{CD} \\ 0 & A_{DC} & A_D \end{pmatrix} \begin{pmatrix} G^r_S & G^r_{SC} & G^r_{SD} \\ G^r_{CS} & G^r_C & G^r_{CD} \\ G^r_{DS} & G^r_{DC} & G^r_D \end{pmatrix} = \begin{pmatrix} I_S & 0 & 0 \\ 0 & I_C & 0 \\ 0 & 0 & I_D \end{pmatrix} . \quad (2.3)$$

Nevertheless, it can be proved [18] that if one can solve the problem in the leads,

$$\begin{aligned} A_S g^r_S &= I_S \\ A_D g^r_D &= I_D \,, \end{aligned} \quad (2.4)$$

then it is possible to define two self-energies Σ^r_S and Σ^r_D

$$\begin{aligned} \Sigma^r_S &= A_{CS} g^r_S A_{SC} \\ \Sigma^r_D &= A_{CD} g^r_D A_{DC} \,, \end{aligned} \quad (2.5)$$

such that the problem in the device region becomes

$$(A_C - \Sigma^r_S - \Sigma^r_D)\, G^r_C = I_C \,. \quad (2.6)$$

In the following, G^r_C will be simply indicated as G^r, so that (2.6) takes the form

$$[(E + \mathrm{i}\eta)I - H_C - \Sigma^r_S(E) - \Sigma^r_D(E)]\, G^r(E) = I \,, \quad (2.7)$$

where the explicit dependence on energy has been introduced. Assuming that the electrostatic potential in the first/last slab of the device region is replicated

periodically in each slab of the semi-infinite source/drain lead, the self-energies $\Sigma^r_{S/D}$ can be numerically computed using an iterative algorithm [24] (see also App. C.2). In the simulations presented in this chapter, the convergence factor η is set equal to zero inside the device region (in order to guarantee current conservation) and to 10^{-5} eV in the leads.

The electron/hole correlation functions are given by

$$G^{</>}(E) = G^r(E)\left[\Sigma_S^{</>}(E) + \Sigma_D^{</>}(E)\right]G^a(E)\,, \tag{2.8}$$

where $G^a = G^{r\dagger}$ is the advanced Green's function. The self-energies $\Sigma_S^{</>}$ describe the in-scattering of electrons/holes from the source lead into the device region and, according to the previously mentioned hypothesis of thermalized contacts, are given by

$$\Sigma_S^{<}(E) = \mathrm{i}\Gamma_S(E) f_S(E)\,, \tag{2.9}$$

$$\Sigma_S^{>}(E) = -\mathrm{i}\Gamma_S(E)\left[1 - f_S(E)\right]\,, \tag{2.10}$$

where $\Gamma_S = \mathrm{i}(\Sigma_S^r - \Sigma_S^a)$ is the broadening function and $f_S(E) = \{\exp[(E - E_{FS})/(k_B T)]+1\}^{-1}$ the Fermi function of the source lead (similar definitions hold for the drain lead and a common temperature T is assumed for both contacts).

From (2.8), one can calculate the electron and hole numbers at the (l,α) atom site as

$$n_{l\alpha} = -2\mathrm{i}\int_{E_i(l,\alpha)}^{\infty}\frac{\mathrm{d}E}{2\pi}\,G^{<}(l,\alpha;l,\alpha;E)\,, \tag{2.11}$$

$$p_{l\alpha} = 2\mathrm{i}\int_{-\infty}^{E_i(l,\alpha)}\frac{\mathrm{d}E}{2\pi}\,G^{>}(l,\alpha;l,\alpha;E)\,, \tag{2.12}$$

where $E_i(l,\alpha)$ is the intrinsic Fermi level, assumed equal to the potential energy $U_{l\alpha}$*, and the factor of 2 in front of both equations is due to spin degeneracy. The current is instead calculated as

$$I = \frac{2q}{h}\int_{-\infty}^{\infty}\mathrm{d}E\,2\Re\left\{\mathrm{Tr}\left[H(l,l+1)G^{<}(l+1,l;E)\right]\right\}\,, \tag{2.13}$$

*This approximation turns out to work well for armchair GNRs, because, as discussed in Sect. 2.2, the application of a non-uniform electrostatic potential over the slab, such as the one found inside a typical device, does not alter significantly the shape of the bandstructure, the main effect being a rigid shift of the subbands rougly equal to the average value of the electrostatic potential energy over the slab. If this approximation does not hold, one is forced to compute the net charge as

$$n_{l\alpha} - p_{l\alpha} = -2\mathrm{i}\int_{-\infty}^{\infty}\frac{\mathrm{d}E}{2\pi}\,G^{<}(l,\alpha;l,\alpha;E) - 1\,,$$

i.e. by starting the integration from an energy below the minumum of the lowest valence subband and by accounting for the +1 charge associated with each nucleus. If transport is coherent, the analycity of G^r with respect to the energy variable can be exploited to convert the integration along the real axis in a contour integration in the complex energy plane, where the number of discretization points can be drastically reduced [25].

where the symbols $\Re$ and Tr indicate the real part and the trace on the orbital index, respectively. Since only coherent transport is considered here, it can be proved that (2.13) is also equivalent to

$$I = \frac{2q}{h} \int_{-\infty}^{\infty} \mathrm{d}E\, T(E) \left[f_S(E) - f_D(E) \right] , \tag{2.14}$$

where $T(E)$ is the transmission function of the Landauer formalism [18]:

$$T(E) = \mathrm{Tr} \left[\Gamma_S G^r \Gamma_D G^a \right] . \tag{2.15}$$

Consider now the computational complexity of the above solution scheme. First, it should be noticed that, since only coherent transport is treated here, particles cannot exchange energy between each other or with external degrees of freedom and thus all energies are decoupled from each other. Second, the cumbersome matrix inversion in (2.7) can be partially avoided. Let N denote the number of slabs in the simulation domain. Due to the fact that H is a block-tridiagonal matrix, with each block representing the coupling between a pair of slabs, the only non-null block of Σ_S^r is $\Sigma_S^r(1,1)$ and the only non-null block of Σ_D^r is $\Sigma_S^r(N,N)$. As a consequence, by directly expanding (2.11), (2.12) and (2.14), it can be derived that the only blocks of G^r which are needed to compute charge and current are those lying on the first and last columns, i.e. $G_{i,1}^r$ and $G_{i,N}^r$, with $i = 1, \ldots, N$. A recursive algorithm can be used to compute just these blocks [23]. The computational cost of this algorithm is roughly $O(N_x^3 N)$[†], where $N_x = 2N_a$ is the size of each matrix block, while the memory cost is $O(N_x^2 N)$. It is worth mentioning that, in the presence of incoherent scattering, a similar recursive algorithm has been developed to solve (2.8), with the same scaling law of the computational and memory costs. The methods that will be presented later in this chapter essentially transform the TB NEGF problem in many independent problems, each one with $N_x < 2N_a$, thus resulting in a computational advantage.

The electrostatic potential energy $U_{l\alpha}$ entering into the Hamiltonian is calculated by self-consistently solving the 3D Poisson equation. The box integration method is used on a discretization grid of prismatic elements with a triangular base, matching the hexagonal graphene lattice. The electron and hole charge given by (2.11) and (2.12) is directly assigned to the box surrounding the (l, α) atom.

2.2 Non-parabolic effective mass approach

The method presented here is an extension of the one used in [26] for modeling transport in CNTs. CNTs are characterized by a bandstructure very similar

[†]The dependence of the computational time with respect to N_x is due to inversion and multiplication operations on matrices of size $N_x \times N_x$: since these operations can take advantage of the sparsity of H, the power-of-3 relationship is usually a pessimistic estimation.

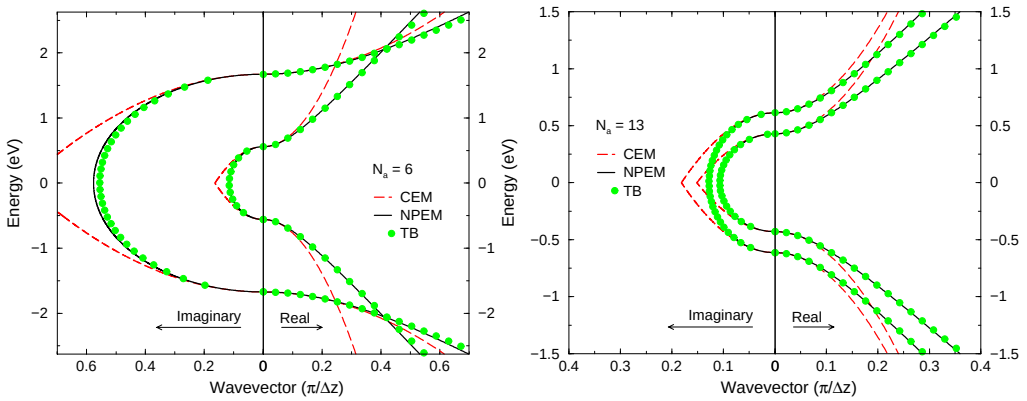

Figure 2.3: Energy dispersion relationships for the two lowest conduction/valence subbands pairs of an $N_a = 6$ (left) and an $N_a = 13$ (right) GNR calculated with the TB model, the EM model with non-parabolic corrections (NPEM) and the constant EM (CEM) model, as a function of the normalized wavevector. The left part of each plot corresponds to energies within the gap.

to the one of GNRs: indeed, a CNT can be thought of as originating from a graphene sheet too, which, instead of being cut in a narrow strip, is rolled in a tube. Therefore, at the first order of approximation, the bandstructure of both GNRs and CNTs can be interpreted as the quantized version of the graphene dispersion relation; however, in the transverse direction, particle-in-a-box boundary conditions are imposed for GNRs, while periodic ones for CNTs. In [26], it was suggested to treat transport separately for each pair of conduction and valence subbands and to model the 1D transport associated to each pair with an effective mass Hamiltonian that includes non-parabolic corrections. While in [26] the electrostatic potential was assumed to be uniform in the angular direction (gate-all-around geometry), this is not the case for the device structure considered here (Fig. 2.1-top): the electrostatic potential over each slab is in general non-flat and its shape can change from one slab to the other. Hence, modifications to treat the transverse problem are needed.

2.2.1 Formulation

In principle, the energy dispersion relationships (subbands) $E(k)$ should be calculated for every slab l of the ribbon, starting from the TB Hamiltonian (2.1) with the potential energy $U_{l\alpha}$ repeated periodically throughout the device. As an example, Fig. 2.3 reports the results of such calculations for the first two subbands (symbols) of an $N_a = 6$ and an $N_a = 13$ GNR, respectively, using a potential identically equal to zero. The portions of the dispersion relationships with energies in the gaps and purely imaginary k, corresponding to vanishing

states, have been computed by solving the generalized eigenvalue problem

$$\begin{pmatrix} EI - H_{l,l} & -H_{l,l+1} \\ I & 0 \end{pmatrix} \begin{pmatrix} v \\ w \end{pmatrix} = e^{-\mathrm{i}k\Delta z} \begin{pmatrix} H^{\dagger}_{l,l+1} & 0 \\ 0 & I \end{pmatrix} \begin{pmatrix} v \\ w \end{pmatrix}, \qquad (2.16)$$

which is obtained from (2.2) using the definition $w = e^{\mathrm{i}k\Delta z}$. It can be seen that the conduction and valence subband of each pair join together in the complex k plane, revealing that they are actually a single branch of the bandstructure. As is well known, increasing N_a leads to reduced gaps and energy separation between the subband minima. Also shown in the same figures are the dispersion relationships (solid lines) obtained with the non-parabolic expression

$$\left(E - \frac{E_g^b}{2}\right)\left(\frac{1}{2} + \frac{E}{E_g^b}\right) = \frac{\hbar^2 k^2}{2m_b^\star} \qquad (2.17)$$

where b is the subband index, $E_g^b = E_c^b - E_v^b$ is the energy gap and $m_b^\star$ the effective mass, used as a fitting parameter. The two sets of curves are in excellent agreement over an extended range of energies, including those in the gap. To show the importance of the non-parabolic correction in (2.17), the figures also report the parabolic dispersion relationship obtained by setting the second factor in parenthesis in (2.17) equal to one. It should be noticed that the main problem with this constant effective mass (CEM) model occurs for energies lying in the gap, leading to an inaccurate estimation of the tunneling currents, as described in the next section.

Similar eigenvalue calculations have been repeated with non-flat potentials typical of slabs in the channel of GNR-FETs and almost identical results have been obtained. This suggests the possibility of neglecting the differences in the shape of the energy dispersion relationships relative to the minima among the different slabs of the device.

The square moduli of the eigenfunctions for the lowest subband relative to $k = 0$ and to the k value corresponding to $E = 0.4\,\mathrm{eV}$ above the bottom of the subband are plotted in Fig. 2.4 as a function of the atom index within the slab, for the $N_a = 13$ GNR. The two curves are almost identical, indicating the possibility of neglecting the k-dependence of the transverse wavefunctions.

The above considerations lead to the following simplifications in the solution of the transverse problem. For a given width (i.e. N_a) the full subband structure is calculated only once for a slab with zero potential, extracting the effective masses of the lowest subbands to be considered in the successive transport calculations. The eigenvalue calculation based on TB is then repeated for every slab of the device only at $k = 0$, so as to obtain E_c^b, E_v^b as well as the eigenfunction χ^b as parametric functions of the longitudinal coordinate z.

The transport problem is then treated within the NEGF formalism, by solving a 1D transport equation in the longitudinal direction for every pair of conduction/valence subbands. The transport Hamiltonian is written within the EM

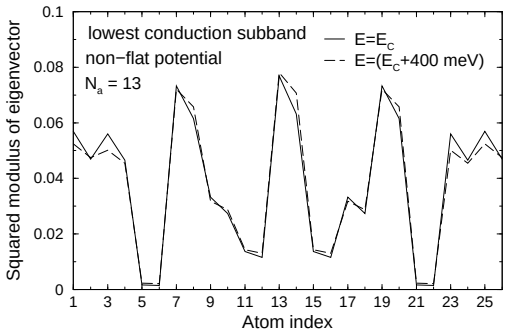

Figure 2.4: Square moduli of the eigenvectors of the lowest conduction subband calculated with the TB model at the two indicated energies for an $N_a = 13$ GNR vs. the atom index within the slab (the atom numbering is the same as in Fig.2.1-bottom).

approximation for a carrier with total energy E in subband b using the functions $E_c^b(z)$ and $E_v^b(z)$ as potential energy profiles. From (2.17) a parabolic Hamiltonian is derived with matrix elements

$$H_b(z,z';E) = \begin{cases} \left[E_c^b(z') - \dfrac{\hbar^2}{2}\dfrac{\mathrm{d}}{\mathrm{d}z'}\left(\dfrac{1}{m_b(z',E)}\dfrac{\mathrm{d}}{\mathrm{d}z'}\right)\right]\delta(z-z') & \text{if } E > E_i^b(z) \\ \left[E_v^b(z') + \dfrac{\hbar^2}{2}\dfrac{\mathrm{d}}{\mathrm{d}z'}\left(\dfrac{1}{m_b(z',E)}\dfrac{\mathrm{d}}{\mathrm{d}z'}\right)\right]\delta(z-z') & \text{if } E < E_i^b(z) \end{cases}, \tag{2.18}$$

with the position-dependent effective mass

$$m_b(z,E) = \begin{cases} m_b^\star\left[1 + \dfrac{E - E_c^b(z)}{E_g^b(z)}\right] & \text{if } E > E_i^b(z) \\ m_b^\star\left[1 + \dfrac{E_v^b(z) - E}{E_g^b(z)}\right] & \text{if } E < E_i^b(z) \end{cases}, \tag{2.19}$$

where $E_i^b(z)$ is the intrinsic Fermi level, assumed equal to the midgap.

The expression in (2.18) can be justify by the following consideration. The proper Hamiltonian matrix describing a 2-band structure with the dispersion relation in (2.17) should be

$$H_b^{2-\mathrm{b}}(k) = \begin{pmatrix} E_c^b & \mathrm{i}c_b k \\ -\mathrm{i}c_b k & E_v^b \end{pmatrix} \tag{2.20}$$

with $c_b^2 = \hbar^2 E_g^b/(2m_b^\star)$. An effective mass Hamiltonian is then obtained by substituting k with $-\mathrm{i}\,\mathrm{d}/\mathrm{d}z$ and by letting E_c^b and E_v^b varying along z with the electrostatic potential:

$$H_b^{2-\mathrm{b}} = \begin{pmatrix} E_c^b(z) & c_b\frac{\mathrm{d}}{\mathrm{d}z} \\ -c_b\frac{\mathrm{d}}{\mathrm{d}z} & E_v^b(z) \end{pmatrix} \tag{2.21}$$

In principle, one should use this Hamiltonian to correctly describe the coupling between a conduction subband and the corresponding valence subband. In the wavefunction formalism, one has a 2-component wavefunction $v^b(z) = [v_1^b(z)\ v_2^b(z))]^T$ and a system of 2 coupled equations corresponding to $H_b^{2-\mathrm{b}} v^b = Ev^b$. It can then be proved that (2.18)-top is the effective Hamiltonian for $v_1^b(z)$ while (2.18)-bottom the effective Hamiltonian for $v_2^b(z)$. Therefore, the implicit approximation in (2.18) is to assume that $v_1^b(z)$ is the dominant component for $E > E_i^b(z)$, while $v_2^b(z)$ the dominant one for $E < E_i^b(z)$. However, the continuity of the wavefunction and of its derivative must be ensured at $E = E_i^b(z)$ to give a physical solution. In the NEGF formalism, this is obtained by changing the sign of the matrix $A_b = EI - H_b$ used for calculating the retarded Green's function,

$$\int \mathrm{d}z'' A_b(z, z''; E) G_b^r(z'', z'; E) = \delta(z - z')\,, \tag{2.22}$$

whenever the particle is in a region for which $E < E_i(z)$, that is[‡]

$$A_b(z, z'; E) = \begin{cases} E + \mathrm{i}\eta - H_b(z, z'; E) & \text{if } E > E_i^b(z) \\ -E + \mathrm{i}\eta + H_b(z, z'; E) & \text{if } E < E_i^b(z) \end{cases}, \tag{2.23}$$

The discretization is done using the standard box integration method. The discretization step Δz is equal to the slab length $3a_{cc}$, so that each grid point corresponds to a slab. After discretization the NEGF formalism is similar to the TB case.

It is worth noting that the lead problem (2.4) can be solved analytically. Consider for example the case of a source lead. By exploiting the periodicity of A, it is possible to extract from the first of (2.4) the recursive relation

$$g_{0,0}^r = \left[A_{0,0} - A_{-1,0}^\dagger g_{0,0}^r A_{-1,0}\right]^{-1}. \tag{2.24}$$

In the EM case, this becomes a scalar equation whose solution is

$$g_{0,0}^r = \frac{X \pm \sqrt{X^2 - 1}}{|A_{-1,0}|}\,, \tag{2.25}$$

with $X = A_{0,0}/(2|A_{-1,0}|)$ and the root is chosen such that $\Im g_{0,0}^r < 0$. The limit $\eta \to 0$ can be directly evaluated as

$$g_{0,0}^r = |A_{-1,0}|^{-1} \times \begin{cases} X - \mathrm{i}\sqrt{-X^2 + 1} & \text{if } X^2 - 1 \le 0 \\ X + \sqrt{X^2 - 1} & \text{if } X^2 - 1 \ge 0 \text{ and } X \le 0 \\ X - \sqrt{X^2 - 1} & \text{if } X^2 - 1 \ge 0 \text{ and } X \ge 0 \end{cases}, \tag{2.26}$$

with $X = A_{0,0}|_{\eta=0}/(2|A_{-1,0}|)$.

[‡]The real part of the retarded Green's function is artificially changed of sign below the mid-gap: this makes impossible to properly include incoherent scattering mechanisms in the model.

The electron and hole numbers at the (l, α) atom site read

$$n_{l\alpha} = -2\mathrm{i} \sum_b |\chi^b_{l\alpha}|^2 \int_{E^b_i(z_l)}^{\infty} \frac{\mathrm{d}E}{2\pi} G^<_b(l,l;E)\,, \tag{2.27}$$

$$p_{l\alpha} = 2\mathrm{i} \sum_b |\chi^b_{l\alpha}|^2 \int_{-\infty}^{E^b_i(z_l)} \frac{\mathrm{d}E}{2\pi} G^>_b(l,l;E)\,, \tag{2.28}$$

where the summations are extended over all the subbands. Such carrier numbers are introduced into the RHS of Poisson's equation, which is solved as described in Sect. 2.1. Once global convergence is achieved, the total current is calculated as

$$I = \frac{2q}{h} \int_{-\infty}^{\infty} \mathrm{d}E \sum_b 2\Re\left\{H_b(l,l+1;E) G^<_b(l+1,l;E)\right\}\,. \tag{2.29}$$

2.2.2 Results

The simulations are focused on a double-gate GNR-FET topology, as depicted in Fig. 2.1-top. The $N_a = 13$ and $N_a = 6$ GNR widths are 1.48 nm and 0.7 nm, respectively. The remaining parameters are: $L_S = L_G = L_D = 10$ nm, $W_G - W_{\mathrm{GNR}} = 4$ nm, $t_{\mathrm{ox}} = 1$ nm, and $\varepsilon_{\mathrm{ox}} = 3.9$ (SiO_2). The gate-aligned source and drain regions are doped with an uniform molar fraction equal to 10^{-2}, while the channel is intrinsic.

A remark is necessary at this point on the validity of the assumption of uniformly distributed doping concentration. In experimental carbon nanotube devices, heavy doping concentrations have been generated either chemically or electrostatically [27], and the same can be assumed for GNRs. In case of chemical doping, due to the very small number of carbon atoms in the source and drain

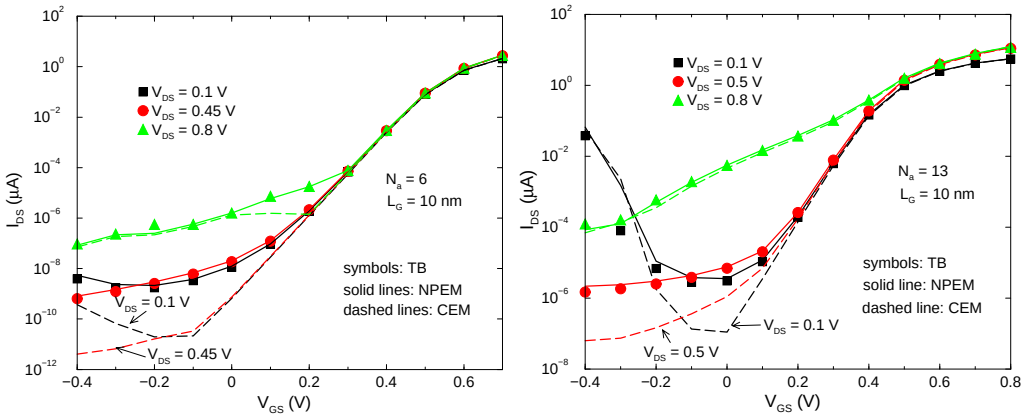

Figure 2.5: Turn-on characteristics of the $N_a = 6$ (left) and the $N_a = 13$ (right) GNR-FET for different V_{DS} computed with the different approximations defined in the text.

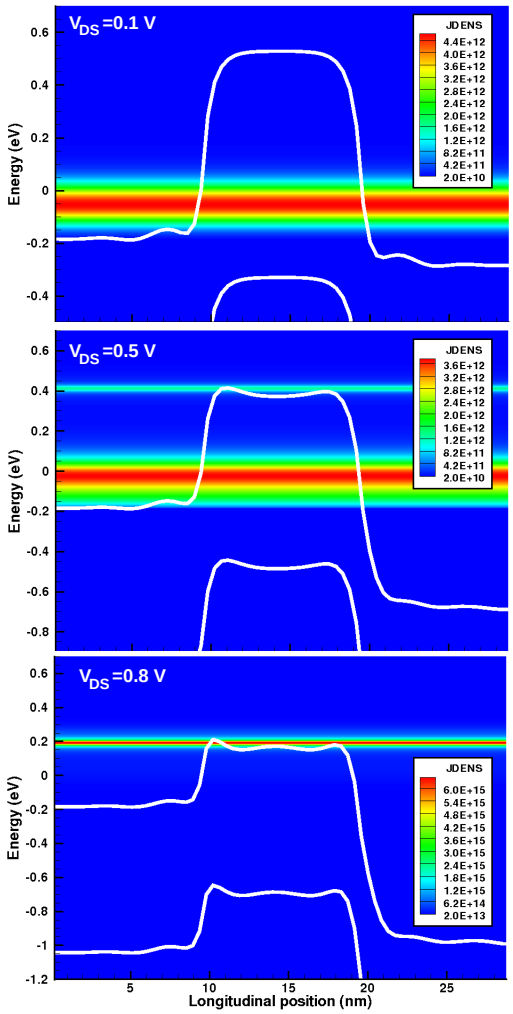

Figure 2.6: Current density spectra in the $N_a = 13$ GNR-FET calculated with the NPEM model at $V_{\mathrm{GS}} = -0.1\,\mathrm{V}$ and $V_{\mathrm{DS}} = 0.1\,\mathrm{V}$ (top), $V_{\mathrm{DS}} = 0.5\,\mathrm{V}$ (center) and $V_{\mathrm{DS}} = 0.8\,\mathrm{V}$ (bottom).

regions, the assumption of average doping concentration is clearly an idealization, whose consequences should be carefully analyzed depending also on the device architecture. The main reason for its widespread use is to avoid the computational complexity of a statistical analysis carried out with respect to the position of the doping atoms. In case of electrostatic doping, the doping level must be interpreted as an effective value which contributes to fixing the electrostatic potential within source and drain regions, therefore the assumption of uniformity is justified.

The turn-on characteristics of the GNR-FETs, computed with the TB, the NPEM and the CEM models are reported in Figs. 2.5 for different V_{DS} values. From both figures it can be seen that the NPEM model agrees remarkably well

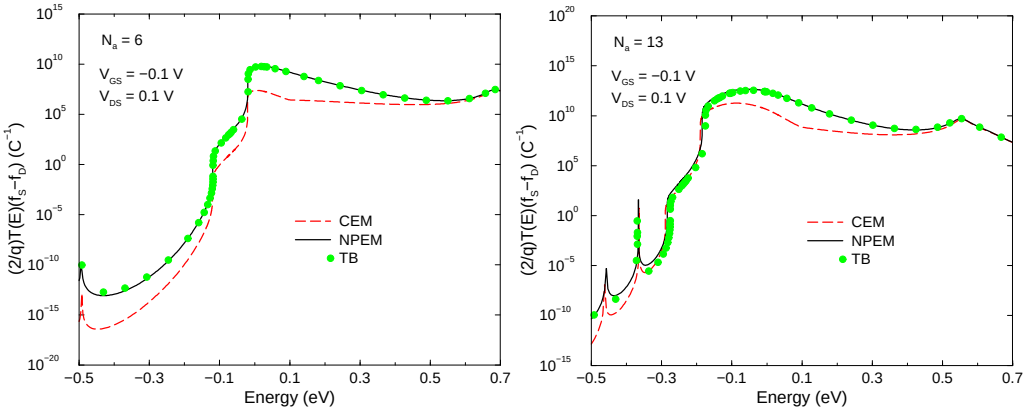

Figure 2.7: Current density spectrum in the $N_a = 6$ (left) and the $N_a = 13$ (right) GNR-FET calculated with the TB, NPEM and CEM models at $V_{\mathrm{GS}} = -0.1\,\mathrm{V}$ and $V_{\mathrm{DS}} = 0.1\,\mathrm{V}$.

with the TB model, while the CEM model suffers from clear limitations in certain bias regions, especially at low V_{GS}. To better understand the origin of such limitations in the different operating regimes, Fig. 2.6 reports the current density spectra, equal (apart from a factor $2/q$) to the integrand of (2.29), for the $N_a = 13$ FET at $V_{\mathrm{GS}} = -0.1\,\mathrm{V}$ and at the same three V_{DS} values of Fig. 2.5-right. At $V_{\mathrm{DS}} = 0.1\,\mathrm{V}$ transport is mainly due to direct tunneling (DT) near the Fermi level (0 eV). It can also be argued that, if V_{GS} is further reduced and the potential energy is thus increased, the conduction and valence bands will face each other at the source and drain junctions, making band-to-band-tunneling (BTBT) possible. This explains the current rise at negative gate voltages in the turn-on characteristics. The $N_a = 6$ FET exhibits a similar behavior, although to a much lesser extent due to the larger energy gap.

At $V_{\mathrm{DS}} = 0.5\,\mathrm{V}$, the conduction and valence bands face each other at the channel-to-drain junction. This generates a positive charge in the channel due to valence electrons tunneling into the drain, leaving behind holes. This positive charge is responsible for the reduction of the source-to-channel barrier visible in the figure. As a consequence, the current rise at low V_{GS}, which is clearly visible for $V_{\mathrm{DS}} = 0.1\,\mathrm{V}$, is suppressed in this case since BTBT from source to drain is quantitatively reduced. Similar considerations apply to the $N_a = 6$ device. At $V_{\mathrm{DS}} = 0.8\,\mathrm{V}$, the electrostatic effect of the positive charge accumulation in the channel is quite strong, considerably lowering the barrier height. Thus, the current becomes dominated by over-the-barrier rather than DT transport with a considerable degradation of the subthreshold slope in the turn-on characteristics. This effect is appreciable also in the $N_a = 6$ FET.

From the previous analysis, one can draw the conclusion that the simple CEM model looses accuracy, especially in the bias regions where the DT current

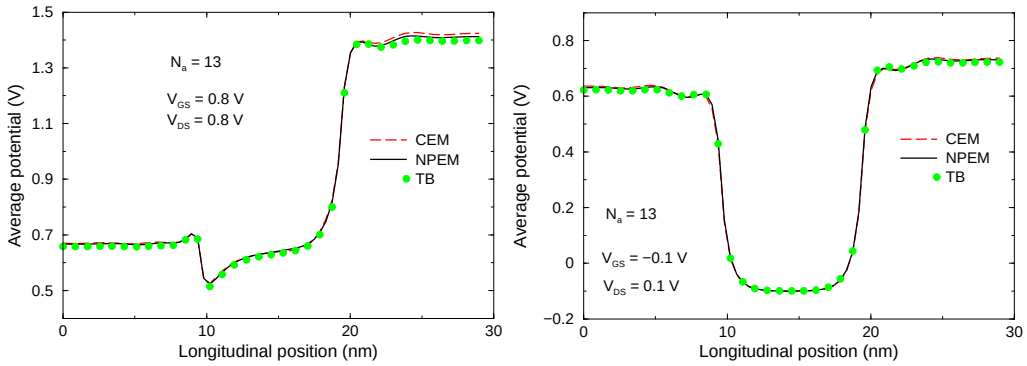

Figure 2.8: Electrostatic potentials averaged on a slab by slab basis in the $N_a = 13$ CNR-FET vs. the longitudinal coordinate in the ON (left) and OFF (right) bias state calculated with the TB, NPEM and CEM models.

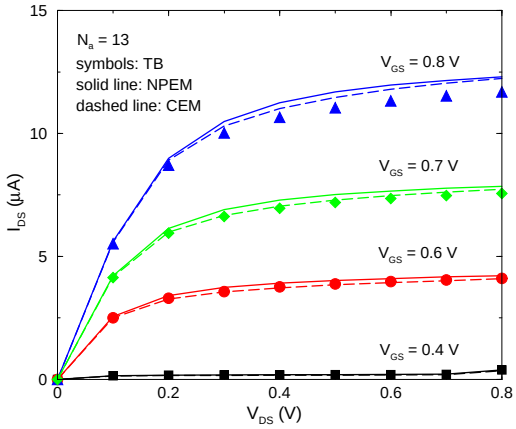

Figure 2.9: Output characteristics of the $N_a = 13$ GNR-FET calculated with the TB, NPEM and CEM models.

dominates. This can be ascribed to the poor energy dispersion relationship in the gap, already evidenced in Fig. 2.3. The introduction of non-parabolic corrections within the NPEM model greatly improves the physical description. To better appreciate the impact of the different approximations the current density spectra calculated with the TB, NPEM and CEM models for the same device and bias conditions as of Fig. 2.6-top are reported in Fig. 2.7-right using a vertical log scale. The agreement between the TB and the NPEM models is very good over the whole energy range. The same conclusion can be drawn for the $N_a = 6$ device (Fig. 2.7-left).

Fig. 2.8 show the electrostatic potentials averaged on each slab of the $N_a = 13$ device as a function of the longitudinal coordinate in the ON and OFF bias states (left and right plots, respectively). The three models agree fairly well with only

minor differences localized in the drain at high bias, including the CEM model. This can be understood by considering that in the ON state the current is due to over-the-barrier transport, where the CEM model works reasonably well while, in the OFF state, the DT current is small and does not perturb the device electrostatics.

Finally, the output characteristics has been analyzed: the result is reported in Fig. 2.9 for the $N_a = 13$ FET. Again, in the previous range of $V_{\mathrm{GS}} \geq 0.4\,\mathrm{V}$, tunneling effects are negligible and the three models provide results in substantial agreement.

2.3 Mode-space tight-binding approach

The application of the MS approach is well established with reference to the simulation of n-channel silicon nanowire FETs within the constant EM approximation, and it has been thoroughly discussed in [28, 29]. On the contrary, the MS approach is not usually adopted with a TB Hamiltonian, since the transverse modes have in general a dependence on k. Thus, even in the case of a flat electrostatic potential, the set of modes at a fixed k should be treated as coupled. However, it has been pointed out in [30] that, for CNTs, an exact decomposition in decoupled modes is possible in the case of a potential with cylindrical symmetry, as found in gate-all-around structures. This method has been extended in [31] to CNT-FETs with no cylindrical symmetry by considering only the lowest energy modes, calculated for a uniform electrostatic potential, all coupled with each other. More recently, an MS approach based on analytically defined modes has been applied to the TB Hamiltonian of GNR devices [32]. On the other hand, real GNRs are always seriously affected by edge roughness, due to the impossibility of achieving edge control with atomic precision using the currently-available technologies. Hence the Hamiltonian, as well as the electrostatic potential, vary from slab to slab, introducing an additional source of mode coupling.

Here, the application of the MS TB approach to the simulation of armchair GNR-FETs with both ideal and non-ideal edges is investigated. With respect to [31], the main features are a novel algorithm for mode selection and decoupling, which goes beyond the simple selection of the lowest energy modes, and the computation of modes on a slab-by-slab basis. As opposed to [32], the modes are numerically computed. Hence, the proposed methodology applies equally well to TB Hamiltonians with different approximation levels, i.e. number of interacting neighboring atoms.

2.3.1 Formulation

As presented before, the RS approach to the NEGF transport problem involves the solution of the equation defining the retarded Green's function (2.7), which

is repeated here for the reader's ease:

$$\left[(E+\mathrm{i}0^+)I - H_C - \Sigma_S^r(E) - \Sigma_D^r(E)\right] G^r(E) = I \ . \tag{2.30}$$

Only coherent transport is considered in this work, but the proposed method is applicable to the case of incoherent scattering as well.

The MS approach is defined as a change of representation. Given an unitary matrix V, (2.30) can be transformed into an MS equation

$$\left[(E+\mathrm{i}0^+)I - \widetilde{H}_C - \widetilde{\Sigma}_S^r(E) - \widetilde{\Sigma}_D^r(E)\right] \widetilde{G}^r(E) = I \ , \tag{2.31}$$

with

$$\widetilde{H}_C = V^\dagger H_C V \ , \tag{2.32}$$

$$\widetilde{G}^r(E) = V^\dagger G^r(E) V \ , \tag{2.33}$$

and similarly for $\widetilde{\Sigma}_{S/D}^r$. Once $\widetilde{G}^r$ is known, the RS solution can be reconstructed by inverting (2.33). Solving (2.31) instead of (2.7) is computationally advantageous if $\widetilde{H}_C$ can be written as a block diagonal matrix apart from an index reordering, thus giving rise to an independent problem for each block (mode decoupling). An additional simplification is achieved if only a subset of these independent problems gives a significant contribution to G^r in the simulated energy window, thus allowing one to neglect the other blocks (mode truncation). The accuracy and efficiency of the MS method depends on the degree with which these two simplifications can be safely carried out in practice. Thus, the selection of the modes to be retained in the calculations and the identification of the coupled and uncoupled modes play a crucial role in the MS approach.

Here, the transformation matrix V is chosen as a block diagonal matrix, which has in the columns of its block of index l the orthonormal eigenvectors at $k = 0$ (modes) of the slab l, computed with the electrostatic potential made periodic along the longitudinal direction.

As mentioned before, the TB modes are coupled even in the presence of a flat electrostatic potential. The mode coupling for the case of an ideal armchair GNR with uniform electrostatic potential, the Hamiltonian of which is periodic, can be studied by comparing the band structure of the RS Hamiltonian with that of the MS Hamiltonian obtained with a specific mode selection, i.e. using a specific subset of the eigenvectors at $k = 0$ (group of modes) as columns of the generic diagonal block of the transformation matrix. If the selected modes are sufficient to accurately reproduce the desired portion of the RS band structure, it means that it is reasonable to consider them uncoupled from the others.

To illustrate the point, Fig. 2.10 shows the energy dispersion relationships of the $N_a = 13$ GNR, computed with the RS and MS TB Hamiltonian with different groups of modes. The valence subbands are not shown, since they are

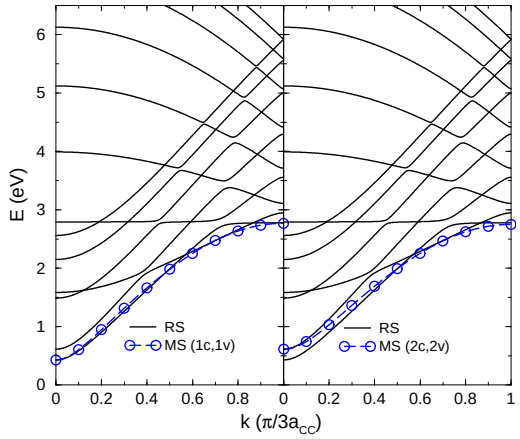

Figure 2.10: Subband structure of an $N_a = 13$ GNR for real k computed with the RS (solid line) and the MS TB (blue circles) using the first (left: 1c,1v) or the second (right: 2c,2v) conduction/valence mode pair at $k = 0$.

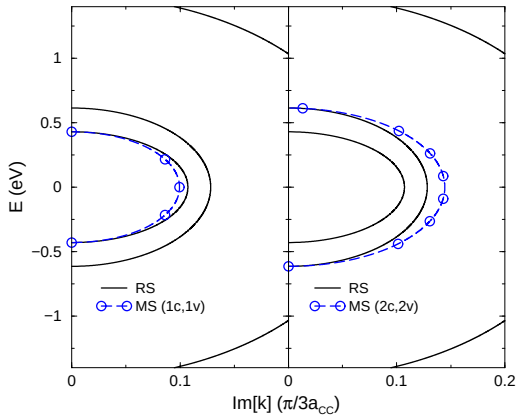

Figure 2.11: Subband structure of an $N_a = 13$ GNR for imaginary k computed with the RS (solid line) and the MS TB (blue circles) using the modes as in Fig. 2.10.

symmetrical in energy with respect to the conduction subbands with symmetry axis at $E = 0$. The mode selection is driven by the purpose of calculating the first two subband pairs with sufficient accuracy, at least near the energy extrema. At first a very simple selection criterion is used by considering two decoupled groups, each made of two modes: the first one, comprising the lowest energy conduction/valence mode pair at $k = 0$, gives the eigenvalues reported with blue circles on the left part of Fig. 2.10 and marked with MS (1c,1v); the second one, made of the next lowest conduction/valence mode pair at $k = 0$, gives the eigenvalues on the right part of the figure and marked with MS (2c,2v).

It is seen that this simple choice gives an almost exact reproduction of the

subband minima, but a wrong estimation of their curvatures (effective masses), especially for the second subband. Fig. 2.11 reports the same eigenvalue calculations for imaginary wavevectors, corresponding to energies in the gaps, which play a fundamental role when tunneling effects are important. It is seen that the MS lacks accuracy especially around the midgap.

From the previous considerations it turns out that more refined mode selection criteria must be identified, possibly accompanied by an easily implemented selection algorithm. To this purpose, the following considerations can be made. The eigenvalue problem for an ideal GNR with flat electrostatic potential and periodic Hamiltonian can be written as (same as Eq. 2.2)

$$\big(H_{l,l} + H_{l,l+1}e^{\mathrm{i}k\Delta z} + H_{l,l+1}^{\dagger}e^{-\mathrm{i}k\Delta z}\big)v(k) = E(k)v(k) \tag{2.34}$$

where $H_{l,l+1}$ is the Hamiltonian block relative to the adjacent slabs l and $l+1$ and $\Delta z = 3a_{\mathrm{CC}}$. Expanding the exponential functions to first order in k around $k = 0$, replacing $v(k)$ with the expansion in the eigenvectors corresponding to $k = 0$ and remembering that

$$\big(H_{l,l} + H_{l,l+1} + H_{l,l+1}^{\dagger}\big)v_m(0) = E_m(0)v_m(0)\,, \tag{2.35}$$

one obtains

$$\sum_m \big[E_m(0) + \big(H_{l,l+1} - H_{l,l+1}^{\dagger}\big)\mathrm{i}k\Delta z\big]c_m(k)v_m(0) = E(k)\sum_m c_m(k)v_m(0)\,. \tag{2.36}$$

Eq. (2.36) can be multiplied by $v_n(0)$ leading to

$$E_n(0)c_n(k) + \mathrm{i}k\Delta z\sum_m \big[v_n^{\dagger}(0)\big(H_{l,l+1} - H_{l,l+1}^{\dagger}\big)v_m(0)\big]c_m(k) = E(k)c_n(k) \tag{2.37}$$

where the orthonormality condition of the eigenvectors $v_m(0)$ has been exploited. The terms in square brackets in (2.37) are responsible for the coupling between modes to first order in k. Thus, it is reasonable to use such terms in the mode selection algorithm.

The considerations above lead to the following algorithm. In a first step, for each couple of modes n and m, the modulus of the quantity

$$C_{nm} \equiv v_n(0)^{\dagger}(H_{l,l+1} - H_{l,l+1}^{\dagger})v_m(0)\ , \tag{2.38}$$

is evaluated to judge about the mutual coupling of the two modes. Is interesting to note that C_{nm} is proportional to the momentum matrix element between the two modes. A threshold of 0.5 eV has been empirically found: if the modulus of C_{nm} is above the threshold, the two modes are considered to be coupled; otherwise, uncoupled. With this criterion the modes are split into several groups: a mode is considered to be coupled only with the other modes within the same group,

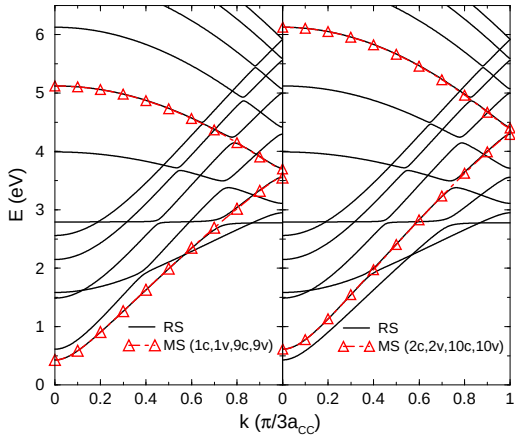

Figure 2.12: Subband structure of an $N_a = 13$ GNR for real k computed with the RS (solid line) and the MS TB (red triangles) using the group of coupled modes (1c,1v,9c,9v) (left) or (2c,2v,10c,10v) (right) at $k = 0$.

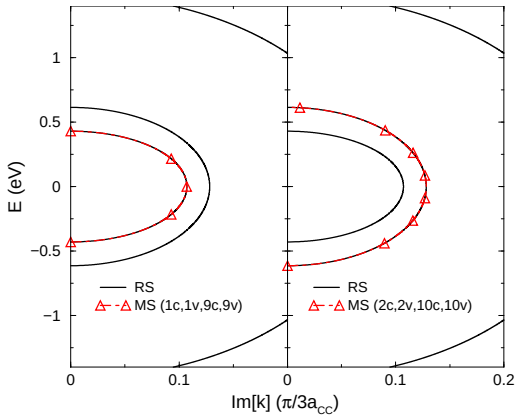

Figure 2.13: Same as in Fig. 2.12 for imaginary k.

but not with the ones belonging to different groups (decoupling criterion). In the second step, only the groups containing at least one of the N_b lowest energy conduction modes or one of the N_b highest energy valence modes are retained (truncation criterion), where N_b is the number of conduction/valence band pairs that are required to be computed with sufficient accuracy.

If the algorithm is applied to the $N_a = 13$ GNR setting $N_b = 2$, two decoupled groups, each formed of four modes, are obtained. The first group, denoted by (1c,1v,9c,9v), contains the 1-st and the 9-th conduction/valence mode pairs at $k = 0$, while the second, denoted by (2c,2v,10c,10v), contains the 2-nd and the 10-th conduction/valence mode pairs at $k = 0$. The eigenvalues calculated with the first and the second group MS Hamiltonian are reported in the left and right part of Fig. 2.12, respectively. With this choice the first two subbands are

perfectly reproduced up to relatively high energies. Looking at the figure, it is interesting to observe that the modes 9c and 10c, which the algorithm reveals to be strongly coupled with modes 1c and 2c, respectively, correspond to eigenvalues belonging to the branches that can be identified with the folded continuations of the branches relative to 1c and 2c, if the small gaps between subbands are ignored. Similar considerations apply to the modes 9v and 10v, which are not shown in the figure. This partly explains the result of the selection algorithm. In any case it should be noted that coupling the modes (1c,1v,2c,2v) does not improve the accuracy with respect to Fig. 2.10, suggesting that the simple selection criterion based on coupling modes looking at their eigenvalues does not work well. Finally, Fig. 2.13 reports the results of the proposed mode selection algorithm for imaginary k. Also in this case the first two branches are very well reproduced.

The algorithm described so far is used for the selection of modes prior to the simulation of devices with regular GNRs, i.e. when the GNR is made of the periodic repetition of an elementary slab. Indeed, as shown in the next section, it has been found that the presence of a non-uniform potential along the axis of a regular GNR does not represent a serious cause of mode coupling, so that the proposed selection criteria based essentially on the observation of the eigenvalues with flat potential are in general sufficient. In case of irregular edges, due to the extra coupling related with the irregular Hamiltonian, the algorithm needs some modification. The mode selection is applied on a slab by slab basis, as if each slab was repeated periodically along the longitudinal direction; finally, all the selected modes are considered coupled in one group only, to account for the effect of mode mixing. In any case, it must be noticed that the algorithm is used for the selection of the mode identifiers only (e.g. 1c, 2c, ...) and it is applied only once at the beginning of the simulation, but the actual modes corresponding to the selected identifiers are recalculated slab by slab for each iteration of Poisson's equation.

2.3.2 Results: ideal GNR-FETs

First, the same $N_a = 13$ ideal GNR-FET analyzed in Sect. 2.2.2 has been simulated. The potential profiles and the transmission coefficients, weighted with the difference between the Fermi functions at the source and drain contacts vs. energy, are computed with the RS and MS methods and the corresponding results are plotted in Fig. 2.14 for the OFF state and Fig. 2.15 for the ON state. Note that the second quantity is the normalized current spectrum (see Eq. 2.14). While in the OFF state the current is mainly due to electron tunneling, in the ON state transport is dominated by electron injection over the barrier. Thus, the accuracy of the MS TB is tested under different operating conditions. For the MS, two different sets of mode groups are considered, corresponding to the

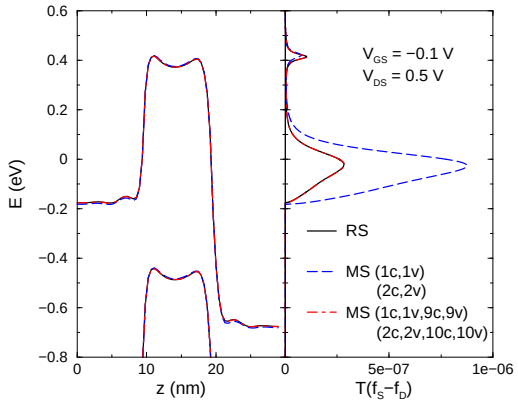

Figure 2.14: Simulation of the $N_a = 13$ ideal GNR-FET in the OFF state ($V_{\mathrm{GS}} = -0.1$ V, $V_{\mathrm{DS}} = 0.5$ V) performed with the RS and MS TB with 2 groups of 2 and 4 coupled modes. Left: band diagram. Right: transmission coefficient times Fermi function difference between source and drain vs. energy. Blue dashed line: 2 modes per group; red dashed-dotted line: 4 modes per group.

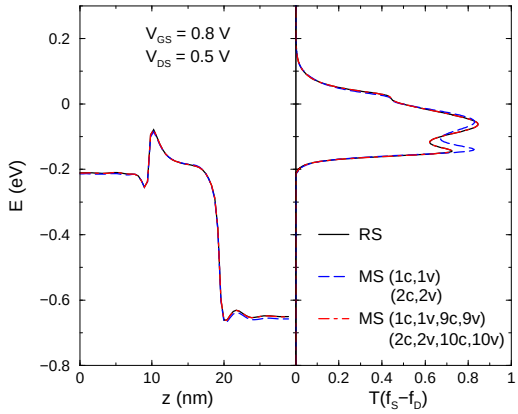

Figure 2.15: Simulation of the $N_a = 13$ ideal GNR-FET in the ON state ($V_{\mathrm{GS}} = 0.8$ V, $V_{\mathrm{DS}} = 0.5$ V) performed with the RS and MS TB with 2 groups of 2 and 4 coupled modes. Legend descriptions are as in Fig. 2.14.

choices already discussed in Figs. 2.10 and 2.12, respectively. Only very small differences between the two MS methods and the RS one can be detected in the potential profile curves (left part of Figs. 2.14 and 2.15). However, when one looks at the current densities (right part of the same figures), it appears that the MS approach with the groups of only two modes overestimates the tunneling current, in particular in the OFF state, due to the bad description of the energy dispersion relation in the bandgap, as shown in Fig. 2.11. On the contrary, the MS with the groups of four modes resulting from the application of the proposed selection algorithm is in perfect agreement with the RS in both the ON and OFF

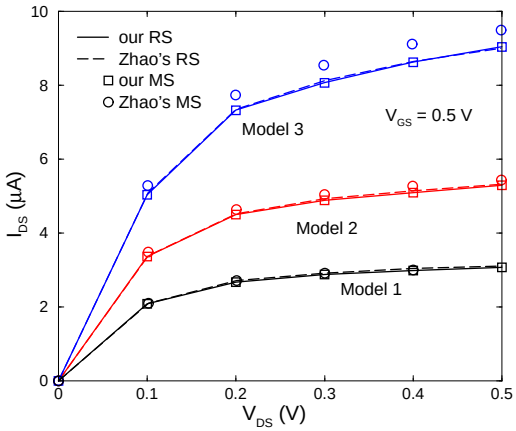

Figure 2.16: Output characteristic at $V_{\mathrm{GS}} = 0.5$ V of the benchmark $N_a = 12$ ideal GNR-FET simulated in [32] calculated with different solution methods (RS TB from this work: solid lines; RS TB from [32]: dashed lines; MS TB from this work: squares; MS TB from [32]: circles) and Hamiltonian models (pure 1NN with $t_1 = -2.7\,\mathrm{eV}$: model1; 1NN + edge distortion with $t_1 = -2.7\,\mathrm{eV}$ and $\delta_1 = 0.12$ as described in Sect. 2.1: model2; 3NN + edge distortion with $t_1 = -2.7\,\mathrm{eV}$, $\delta_1 = 0.12$ and $t_3 = -0.2\,\mathrm{eV}$: model3).

state. This confirms that the decoupling criterion, discussed in Sect. 2.3.1 for a uniform potential, behaves well even in the case of a spatially varying potential. Indeed, the NPEM method presented before was based on this assumption.

It is interesting to compare the MS approach presented here with the one in [32], where the modes are analytically computed. To ease the comparison, the same ideal GNR-FET with $N_a = 12$, simulated in [32], is used as benchmark device. The geometry is similar to that of the $N_a = 13$ GNR-FET, except for $t_{\mathrm{ox}} = 1.5\,\mathrm{nm}$ and the source/drain doping molar fraction $5 \cdot 10^{-3}$. Fig. 2.16 shows the output characteristics computed with different Hamiltonian models and solution methods (see caption for the model details). It should be noticed that the curves marked with model 3 refer to the same 3NN Hamiltonian used in [32]. The two RS TB set of curves (solid and dashed lines) obviously match, and have both been reported only to verify the consistency between the models and the device geometries. It can be noticed that the MS approach proposed in this work agrees very well with the RS TB for all of the Hamiltonian models, including the 3NN. On the other hand, the MS approach in [32], being based on a simplified analytical mode computation, slightly departs from the RS solution as the model becomes more complex.

To test the computational efficiency of the proposed method a structure of larger size has been simulated. A *p-i-n* tunneling FET (TFET) architecture, which is extensively studied for its great potential in low-voltage and low-power applications, has been chosen. The indication of CNTs as ideal material for

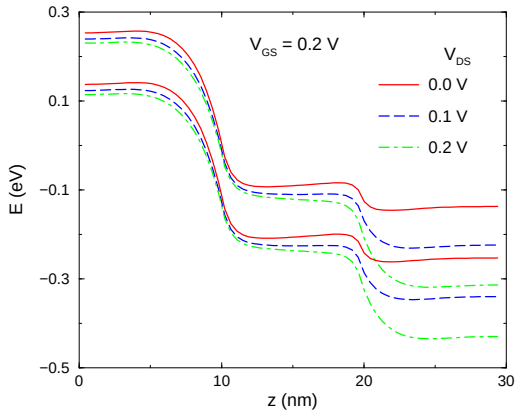

Figure 2.17: Band diagram of the simulated $N_a = 100$ ideal GNR tunnel FET with $V_{\rm GS} = 0.2$ V and $V_{\rm DS} = 0.0, 0.1, 0.2$ V performed with the MS TB with 10 groups of 4 coupled modes each. The MS TB approach coupling the same 40 modes in one group gives almost identical profiles (not shown in the figure).

TFETs was first given in [33]. Similar considerations apply to GNR-TFETs.

The simulated TFET is based on an $N_a = 100$ GNR with ideal edges, having a width of approximately 10 nm. The topology of this TFET is identical to Fig. 2.1-top, except for the use of a p-type source. The geometrical dimensions are the same of the $N_a = 13$ GNR-FET, apart from the GNR width. A doping molar fraction of 10^{-3}, symmetric for the source and drain regions, has been assumed. In this case the size of the numerical problem is such that the simulation of this device with the RS TB on a single processor becomes exceedingly tedious. So, in order to check the accuracy of the solution, it has been decided to compare the proposed MS TB approach, which leads to the selection of 10 groups of 4 modes, with a different MS TB solution obtained by using the same 40 modes all coupled together. In the former approach, the large number of groups (10) is necessary to cover a sufficiently large energy range extending above the source Fermi level, given the small spacing between the subbands due to the relatively large GNR width. The two methods give essentially identical results, confirming the validity of the mode decoupling procedure. For illustrating purpose, the band diagrams corresponding to $V_{\rm GS} = 0.2\,$V and three different drain bias conditions are reported in Fig. 2.17. It should be noticed that the bandgap is quite small ($\simeq$ 0.1 eV), which favors the band-to-band-tunneling (BTBT) at the source junction. However, for $V_{\rm DS} = 0.2\,$V there is already a sizable BTBT at the drain junction, which affects the potential in the channel, and ultimately leads to limitations in the supply voltage. As far as the numerical efficiency is concerned, the difference between the two tested MS approaches ranges between 40$\times$ and 60$\times$ depending on the bias conditions. The advantage with respect to the RS method is of course much larger.

2.3.3 Results: GNRs with irregular edges

In this section the assumption of ideal GNRs is removed and the behavior of the MS approach in case of irregular GNR edges is examined. First, a device formed by a simple junction between an $N_a = 13$ and an $N_a = 12$ GNR is considered. This can be thought of as a special type of heterojunction implemented using GNRs of different widths, which can find applications in the nanoelectronic world. Examples of experimental and theoretical studies of the transport across heterojunctions formed connecting together CNTs of different diameter can be found in [34] (Y-junctions) and in [35] (orbital filtering obtained with multiply connected CNTs). Fig. 2.18 shows the local density of states (LDOS) versus longitudinal coordinate and energy. This quantity is given by (see also Sect. B.1)

$$-\frac{1}{\pi}\Im\{\mathrm{Tr}[G^r(l,l;E)]\} \simeq -\frac{1}{\pi}\Im\{\mathrm{Tr}[\widetilde{G}^r(l,l;E)]\}\,, \tag{2.39}$$

where the trace is done on the orbital index in RS and on the mode index in MS, and the degree of approximation, of course, depends on mode decoupling and truncation. The larger energy gap in the $N_a = 13$ half and the perturbation produced by the junction on the subband structures of the two separate devices can be clearly appreciated. The comparison between the average LDOS at the junction and transmission coefficients obtained with the RS and MS TB is performed in Fig. 2.19. As explained in Sect. 2.3.1, in case of irregular edges all selected modes are treated as coupled in one group. The curves labeled with "8 modes" have been computed by coupling all of the eight modes resulting from the application of the algorithm with $N_b = 2$ (for the $N_a = 13$ side the modes are the ones indicated in Fig. 2.12), while, for the ones labeled with "12 modes", four

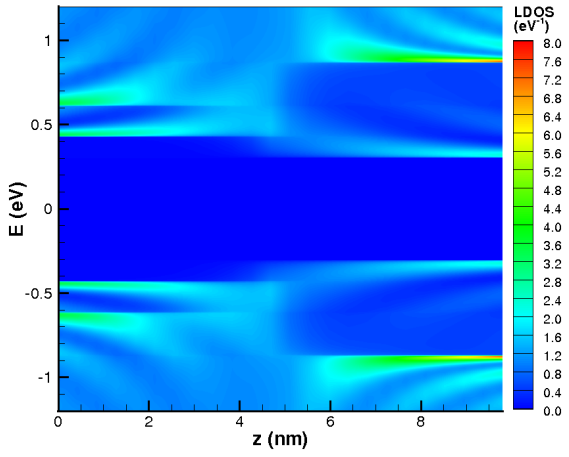

Figure 2.18: LDOS integrated over each slab vs. longitudinal coordinate and energy of an $N_a = 13$ and 12 GNR junction. The $N_a = 13$ GNR lies on the left half. Zero bias is applied.

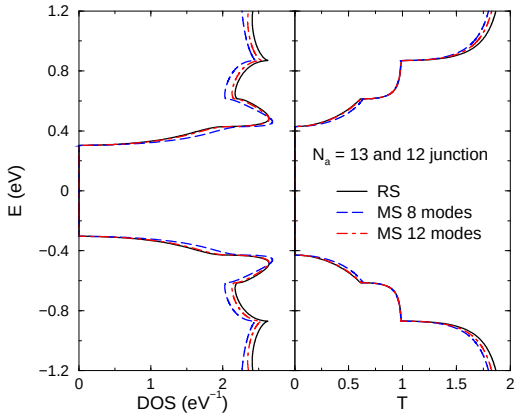

Figure 2.19: Simulation of the $N_a = 13$ and 12 GNR junction under zero bias performed with the RS and MS TB with 8 and 12 coupled modes. Left: LDOS integrated over the two slabs adjacent to the junction. Right: transmission coefficient vs. energy.

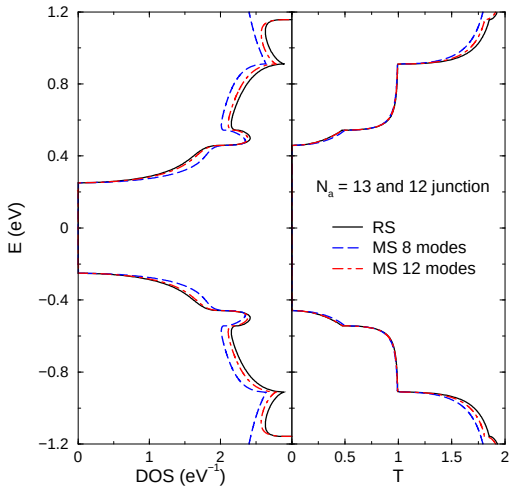

Figure 2.20: Simulation of the $N_a = 13$ and 12 GNR junction as in Fig. 2.19, but using the 3NN model from [21].

additional modes have been accounted for, corresponding to the application of the algorithm with $N_b = 3$, resulting in a clear improvement. It can be concluded that good results are obtained even with a limited number of modes, despite the junction-induced mode mixing.

It is interesting to observe that while the average DOS (left part of Fig. 2.19) exhibits an effective gap that nearly coincides with the smaller gap, i.e. the one of the $N_a = 12$ section, the transmission coefficient (right part of Fig. 2.19) significantly departs from zero only for energies corresponding to states that can propagate throughout the device, i.e. for energies outside of the larger gap, which

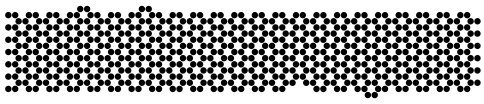

Figure 2.21: Channel of the $N_a = 13$ GNR with edge roughness used in the FET simulated in Figs. 2.22 and 2.23.

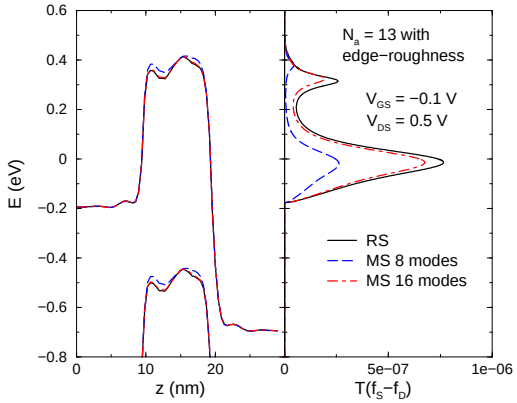

Figure 2.22: Simulation of the $N_a = 13$ GNR-FET with the rough channel of Fig. 2.21 in the OFF state ($V_{\rm GS} = -0.1$ V, $V_{\rm DS} = 0.5$ V) performed with the RS and MS TB with 8 and 16 coupled modes. Left: electrostatic potential energy averaged on each slab and shifted by $\pm E_G/2$, E_G being the gap of the $N_a = 13$ ideal GNR. Right: transmission coefficient times Fermi function difference between source and drain vs. energy.

is the one of the $N_a = 13$ section. This mismatch between DOS and transmission effective gap is typical of structures with irregular edges.

The simulation has been repeated by using a 3NN model to investigate the effect of a more refined Hamiltonian model on the mode-mixing. In this case the Hamiltonian model is taken from [21] and has been calibrated on *ab initio* calculations ($t_1 = -3.2$ eV, $\delta_1 = 0.0625$, $t_3 = -0.3$ eV). The DOS and transmission coefficients are shown in Fig. 2.20. Results are qualitatively similar to those of Fig. 2.19 and neither a degradation of the MS performance nor a need for an extended set of modes is revealed.

Finally, the impact of edge roughness is investigated. The same topology of the previous ideal $N_a = 13$ GNR-FET, but with the rough GNR channel shown in Fig. 2.21, has been simulated. Edge roughness is obtained from the nominal $N_a = 13$ GNR by randomly adding or removing atom pairs at the two edges independently, according to a predefined probability $P = 0.05$ as proposed in [36]. Figs. 2.22 and 2.23 report the results for the OFF and ON state, respectively. It is seen that, in order to have a good estimate of the current density, 16 coupled modes out of a total number of 26 for the $N_a = 13$ GNR need to be used.

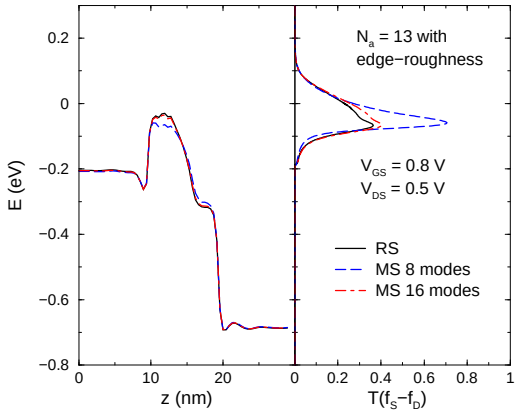

Figure 2.23: Simulation of the $N_a = 13$ GNR-FET with the rough channel of Fig. 2.21 in the ON state ($V_{\mathrm{GS}} = 0.8$ V, $V_{\mathrm{DS}} = 0.5$ V) performed with the RS and MS TB with 8 and 16 coupled modes. Legend descriptions are as in Fig. 2.22.

The 8 modes used before for the ideal GNR of Figs. 2.14 and 2.15 are definitely insufficient, even if treated as being all coupled in the same group.

2.4 Summary

In this chapter two efficient methods for the simulation of GNR-FETs have been presented and validated.

The NPEM model is based on the effective mass approximation. It is shown that by making the EM dependent on kinetic energy, and thus on position for an electron with a given total energy, the armchair GNR-FETs behavior can be simulated with good accuracy over all bias conditions, including those regions where tunneling through the energy gap dominates current transport. The NPEM model is highly attractive due to its remarkable computational time advantage with respect to RS TB, which can be estimated to be roughly two orders of magnitude for the devices and bias conditions investigated in this work.

The MS TB method is introduced to overcome the deficiencies of the NPEM model. It is based on a novel criterion for identifying the modes that need to be treated as coupled in the calculations. For ideal GNR-FETs, the decoupling into separate groups of coupled modes gives almost exact results with a computational advantage with respect to RS TB in the order of $60\times$ for a $N_a = 13$ GNR, and even more for larger GNRs. For irregular GNRs, mode coupling has to be taken into account to achieve accurate results, and thus the advantage over RS TB is reduced.

The proposed methods can be used for the systematic investigation and optimization of future GNR devices.

Chapter 3

Simulation studies of GNR-FETs

In this chapter, a simulation study is performed to investigate the performance limits of GNR-FETs for digital applications. Both conventional and tunneling FET architectures are considered. For the former architecture (Sect. 3.1), the study focuses on relatively wide GNR-FETs, as the ones that can be fabricated with the state-of-the-art technology. Since large widths result in small band gaps, the ON/OFF current ratio is the main limitation of these devices: the design parameter space is investigated in order to cope with this problem. For the tunneling FET architecture (Sect. 3.2), the investigation also provides some guidelines for the choice of the design parameters, showing the great potential for very good ON/OFF ratios at low supply voltages. The importance of a very good control on edge roughness is also highlighted.

3.1 Conventional FETs

Simulations of extremely narrow GNR-FETs ($N_a = 6$ and $N_a = 13$) have already been presented in Sect. 2.2.2. The main results are summarized in the following. From the turn-on characteristics (Fig. 2.5), the great potential of ideal and extremely-narrow graphene-based FETs can be fully appreciated. For example, from Fig. 2.5-right a current drive capability normalized to the GNR width ($W_{\mathrm{GNR}} = 1.5\,\mathrm{nm}$) as large as 8 mA/$\mu$m (at $V_{\mathrm{DS}} = V_{\mathrm{GS}} = 0.8$ V) is predicted, which by far exceeds that of present silicon devices at comparable supply voltages. On the other hand, the device suffers from limitations in turning the current off at the largest drain bias (Fig. 2.5-right, $V_{\mathrm{DS}} = 0.8$ V), due to the onset of BTBT effects at the drain end of the channel, that reduce the gate control over the

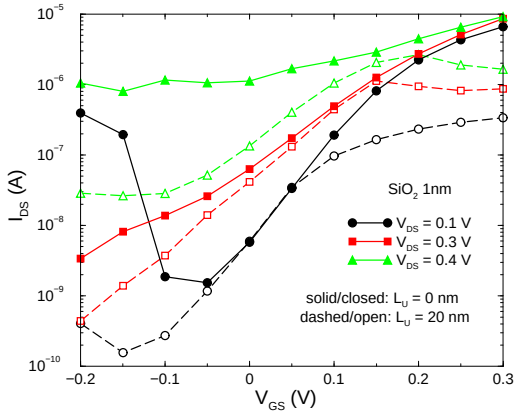

Figure 3.1: Turn-on characteristics of the $N_a = 40$ GNR-FET with $\varepsilon_{\rm ox} = 3.9$ and $t_{\rm ox} = 1\,$nm at various $V_{\rm DS}$, with ($L_U = 20$ nm) and without ($L_U = 0$) underlap.

channel.

Due to the formidable technological challenge in building GNRs of nanometer widths with well controlled edges, it is interesting to investigate how much the GNR width can be relaxed while maintaining an overall competitive device performance. Relaxing the GNR width means reducing the band gap; hence, the OFF-state current limitations are expected to become more severe, thus requiring a careful choice of the design parameters. This section presents a performance investigation of relatively wide (a few nanometers) GNR-FETs with small band gap using the NPEM model in Sect. 2.2. Being the $I_{\rm ON}/I_{\rm OFF}$ ratio the main limitation of small band gap devices, it is discussed how the design parameters ought to be chosen in order to mitigate the problem. The ratio $I_{\rm ON}/I_{\rm OFF} > 10^4$ is chosen as the acceptance criterion. The topology is the same as in Fig. 2.1-top with doped source/drain regions; however two intrinsic source/drain gate underlap regions of extension L_U have also been considered, where L_U is an optimization parameter. The gate length is fixed at $L_G = 20\,$nm, so as to prevent direct source-to-drain tunneling in the OFF state.

The turn-on characteristics of a $N_a = 40$ 4.8 nm-wide GNR-FET are shown in Fig. 3.1 for $V_{\rm DS} = 0.1$, 0.3 and 0.4 V with $L_U = 0$ and $L_U = 20\,$nm. Here $\varepsilon_{\rm ox} = 3.9$, $t_{\rm ox} = 1\,$nm, and the dopant molar fraction in the source and drain regions is equal to 10^{-3}. Clearly, for the self aligned device ($L_U = 0$) the $I_{\rm ON}/I_{\rm OFF}$ ratio rapidly deteriorates for $V_{\rm DS} > 0.3\,$V. This can be understood by looking at the conduction and valence band profiles of Fig. 3.2-left for $V_{\rm DS} = 0.4\,$V and $V_{\rm GS} = -0.1\,$V. As the band gap is only 0.29 eV, channel-to-drain BTBT occurs in the OFF state. The underlap regions make the potential profile at the drain junction smoother and effectively reduce $I_{\rm OFF}$, but degrade at the same time

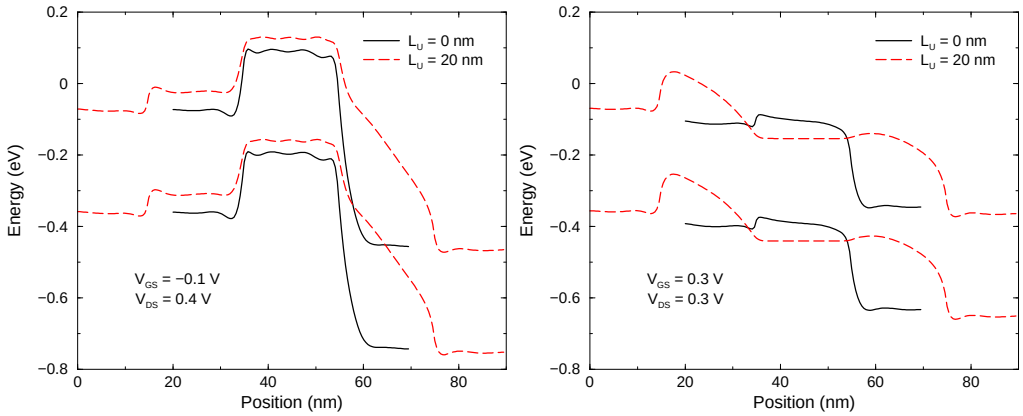

Figure 3.2: Conduction and valence band profiles for the GNR-FET of Fig. 3.1 at $V_{\rm GS}$ = -0.1 V and $V_{\rm DS}$ = 0.4 V (left) and at $V_{\rm GS} = V_{\rm DS}$ = 0.3 V (right), with (L_U = 20 nm) and without ($L_U = 0$) underlap.

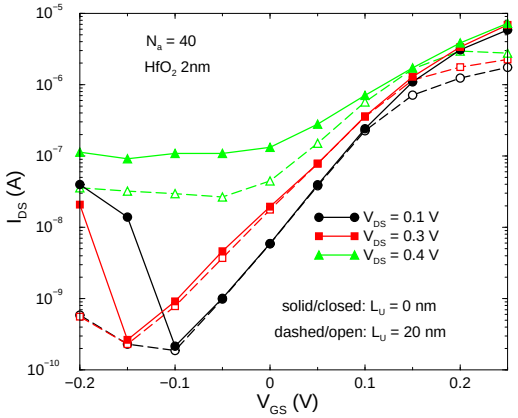

Figure 3.3: Turn-on characteristics of the $N_a = 40$ GNR-FET with $\varepsilon_{\rm ox} = 16$ and $t_{\rm ox} = 2$ nm at various $V_{\rm DS}$, with (L_U = 20 nm) and without ($L_U = 0$) underlap.

$I_{\rm ON}$. Fig. 3.2-right illustrates how the intrinsic underlap region at the source side creates a potential barrier in the ON state that limits the peak current and is not controlled by the gate.

The effect of a high-κ dielectric is investigated next. The turn-on characteristics with $\varepsilon_{\rm ox} = 16$ (HfO_2) and $t_{\rm ox} = 2$ nm are reported in Fig. 3.3 for the same values of $V_{\rm DS}$, both with and without underlap. From the comparison with Fig. 3.1, it appears that the increase of $\varepsilon_{\rm ox}$ has a beneficial effect mainly at low $V_{\rm GS}$, considerably lowering the OFF current. At $V_{\rm DS} = 0.4$ V the use of the underlap regions further reduces $I_{\rm OFF}$ which, however, remains unacceptably high. At $V_{\rm DS}$ = 0.1 and 0.3 V, the underlap regions simply deteriorate $I_{\rm ON}$ without any

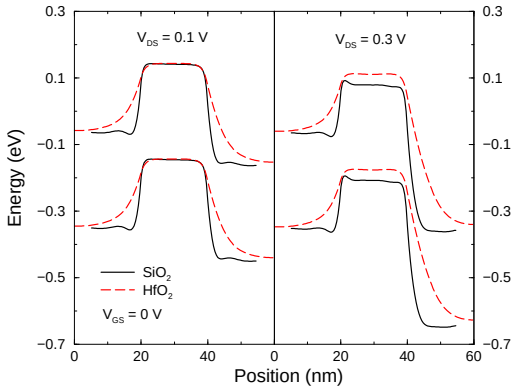

Figure 3.4: Conduction and valence band profiles for the $N_a = 40$ GNR-FET with $L_U = 0$, at $V_{\rm GS} = 0$ V and $V_{\rm DS} = 0.1$ V (left) and 0.3 V (right), with (HfO_2) and without (SiO_2) a high-κ material.

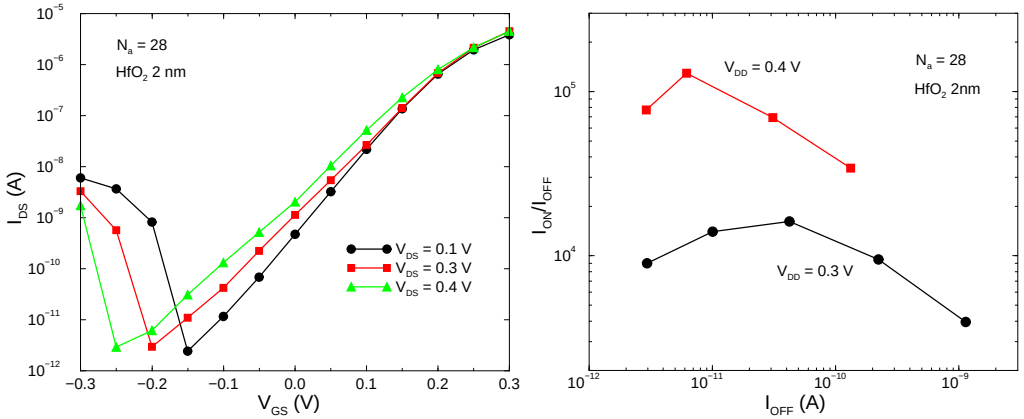

Figure 3.5: Left: turn-on characteristics of the $N_a = 28$ GNR-FET with $\varepsilon_{\rm ox} = 16$ and $t_{\rm ox} = 2\,$nm at various $V_{\rm DS}$ without underlap. Right: $I_{\rm ON}/I_{\rm OFF}$ ratio as a function of $I_{\rm OFF}$ (different gate work functions) for the same device. Two supply voltages of 0.3 V and 0.4 V are considered.

appreciable benefit on $I_{\rm OFF}$. The use of underlap regions can therefore be ruled out. The band profiles of Fig. 3.4 explain the origin of the OFF current improvement at low $V_{\rm GS}$ when a high-κ material is used: the improved electrostatic control of the gate on the channel potential dominates over the barrier lowering induced by BTBT at the drain junction.

From the previous analysis, it can be argued that a ratio $I_{\rm ON}/I_{\rm OFF} = 10^4$ cannot be achieved by the devices considered so far. In order to reach the target ratio, a device able to bear $V_{\rm DS} \simeq 0.4\,$V without any significant degradation of

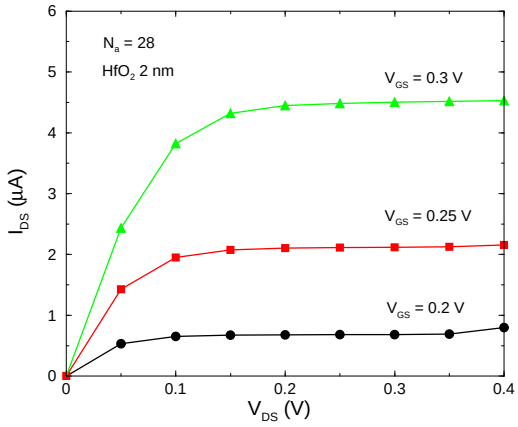

Figure 3.6: Output characteristics of the GNR-FET of Fig. 3.5 at $V_{\rm GS} = 0.2$, 0.25 and 0.3 V.

the OFF current is needed. Extrapolating from the previous considerations, an $N_a = 28$ 3.3 nm-wide GNR-FET, having $E_G = 0.41\,$eV, is selected. The turn-on characteristics, simulated with $\varepsilon_{\rm ox} = 16$, $t_{\rm ox} = 2\,$nm, a source/drain dopant molar fraction of $1.5 \cdot 10^{-3}$ and $L_U = 0$ are shown in Fig. 3.5-left, while Fig. 3.5-right illustrates the $I_{\rm ON}/I_{\rm OFF}$ ratio at 0.3 and 0.4 V supply voltages for different $I_{\rm OFF}$ values, i.e. different gate work functions. For this device, the maximum achievable current ratio is nearly 10^5 for a supply voltage of 0.4 V. Moreover, the output characteristics, shown in Fig. 3.6, exhibit a nearly ideal behavior, indicating that this device is not appreciably affected by short channel effects, apart from the small current increase at $V_{\rm DS} = 0.4$ V caused by the barrier lowering induced by BTBT at the drain junction. The current drive capability is 1.3 mA/μm (Fig. 3.6 at $V_{\rm GS} = 0.3$ V and $V_{\rm DS} = 0.4$ V) which is comparable with what obtained from silicon devices at 1 V supply. As the dynamic power scales with the square of the supply voltage, this lowering represents a nearly $6\times$ advantage with respect to silicon.

In conclusion of this section it can be stated that, even if the best performance is obtained from nanometer-wide GNR-FETs, the width can be somewhat relaxed up to $\simeq 3.5\,$nm while maintaining an acceptable ON/OFF current ratio in excess of 10^4. The resulting current drive capability for an ideal GNR-FET is comparable with that of silicon devices, with a definite advantage in terms of power dissipation.

3.2 Tunneling FETs

The tunneling transistor (TFET) has been proposed as the ideal architecture for carbon nanotube (CNT) FETs [33], capable of overcoming some limitations of

the conventional FET topology. The CNT-TFET is based on an intrinsic gated channel and source/drain regions with opposite types of doping, i.e., (*n-i-p* or *p-i-n*). The band-bending in the source-channel junction is responsible for gate-controlled BTBT current which is the main conduction mechanism, as opposed to thermal emission over the barrier for conventional FETs. Thus, a subthreshold slope (SS) better than 60 mV/dec can be achieved. A similar behavior is expected from GNR-TFETs. In this section a number of GNR-TFETs are simulated and guidelines for the optimal choice of the design parameters (gate topology, type and size of dielectric, source/drain doping concentrations) are provided, reaching similar conclusions as in [37]. Besides, the effect of edge roughness is taken into account via the direct simulation of rough GNR channels with randomly generated defects at the edges. Indeed, edge roughness is known to seriously limit the performance of conventional GNR-FETs [9], reducing the ON current and increasing the OFF leakage, due to the formation of localized states in the gap [36]. Regarding the solution approach, the simulations of GNRs with ideal edges are carried out with the MS TB in Sect. 2.3, while, in the case of GNRs with rough edges, the RS TB is used to accurately account for the mode-mixing.

The study starts with investigating the impact of some design parameters on the performance of ideal GNR-TFETs, with the purpose of understanding the key optimization issues. Two types of topologies are considered: the double gate (DG) topology, similar to Fig. 2.1-top but with p^+ source, and the single gate (SG) one, similar to the former but with one top gate and a 10 nm thick bottom dielectric. In all simulated devices $W_G - W_{\mathrm{GNR}} = 4\,\mathrm{nm}$.

The following general guidelines for the design of TFETs are known from the literature. In order to increase the ON current, the BTBT at the source junction must be favored, which suggests the use of GNRs with small band gap and the opportunity of having a high longitudinal electric field, i.e. band bending, at the same junction. In an ideal armchair GNR the band gap depends essentially on the ribbon width, while the shape of the electric field involves a number of parameters, such as the dielectric constant of the insulator, its thickness and the source doping concentration. On the other hand, the minimum leakage current for a given V_{DS} can be traced back to the three following mechanisms, which have different importance depending on the device parameters: thermal current (injection of conduction band electrons from the source and valence band holes from the drain), source-to-drain BTBT throughout the entire channel, and BTBT at the drain junction (responsible for current rise at low V_{GS}, similar to conventional FETs). All three conduction mechanisms can be reduced by making the band gap larger, in contrast with the large ON current requirement. Moreover, the condition for which the leakage current is given by BTBT at the drain junction can be avoided by making the maximum V_{DS} sufficiently smaller than the gap.

The turn-on characteristics of different devices have been simulated. The

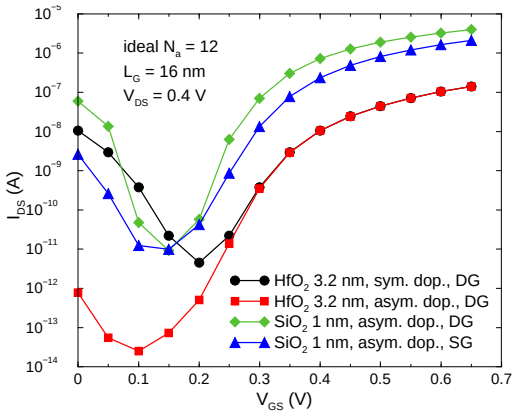

Figure 3.7: Turn-on characteristics of the ideal $N_a = 12$ GNR-TFETs with $L_G = 16\,\text{nm}$, source doping molar fraction $N_S = 5 \cdot 10^{-3}$ and $V_{\text{DS}} = 0.4\,\text{V}$. Legends: $\varepsilon_{\text{ox}} = 16$ for HfO_2, $\varepsilon_{\text{ox}} = 3.9$ for SiO_2, $N_D = N_S$ for sym. dop., $N_D = 10^{-3}$ for asym. dop., double (DG) or single (SG) gate topology.

results for an ideal $N_a = 12$ GNR ($W_{\text{GNR}} = 1.35\,\text{nm}$, $E_G = 0.61\,\text{eV}$) are reported in Fig. 3.7. The applied drain voltage $V_{\text{DS}} = 0.4\,\text{V}$ is sufficiently lower than E_G to ensure that the leakage current is not due to BTBT at the drain junction. First of all, the choice of the doping levels in the source and drain regions is investigated. The curves marked with black circles and red squares in Fig. 3.7 have been obtained with the same parameter set (please refer to the figure caption for details) except for the doping molar fraction in the drain, which is $5 \cdot 10^{-3}$ and 10^{-3}, respectively. The leakage current is clearly reduced for the lower drain doping level. The reason is better understood by observing the band diagram and current density plots of Fig. 3.8 relative to $V_{\text{GS}} = 0.2\,\text{V}$. The current is mainly due to BTBT into the channel, and the effect of the lower doping concentration is twofold: (i) reducing the drain degeneracy by shifting up the conduction band edge and, (ii) making the potential transition from channel to drain less abrupt, thus elongating the tunneling path. Both effects reduce the BTBT current.

Next, the effect of dielectric type and thickness is examined. To this purpose, the red squares and green diamonds curves of Fig. 3.7 must be compared. The former is obtained with 3.2 nm HfO_2 ($\varepsilon_{\text{ox}} = 16$); the latter with 1 nm SiO_2 ($\varepsilon_{\text{ox}} = 3.9$), all other parameters being the same. Despite the larger EOT and the lower $C_{\text{ox}} = \varepsilon_{\text{ox}}/t_{\text{ox}}$, the SiO_2 TFET exhibits strikingly larger currents. The band diagram and transmission coefficient plots of Fig. 3.9 for $V_{\text{GS}} = 0.55\,\text{V}$ reveal the importance of gate-source fringing. A thicker high-κ oxide increases the fringing and reduces the BTBT at the source. It is also seen that the transmission coefficient is quite large ($\max[T(E)] \simeq 0.2$), and thus the BTBT does not represent a serious bottleneck for achieving high ON currents.

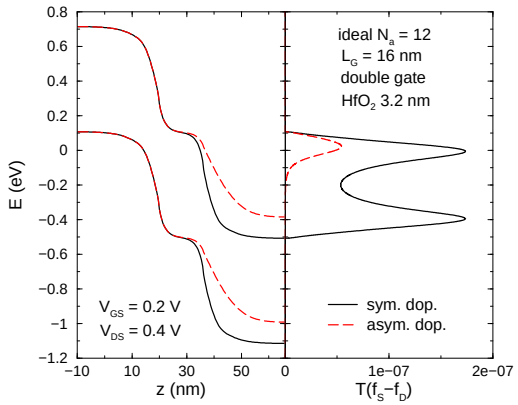

Figure 3.8: Band diagram (left) and transmission coefficient multiplied by the Fermi function difference between source and drain (normalized current density) vs. energy (right) for the $N_a = 12$ ideal GNR-TFET with $V_{\mathrm{GS}} = 0.2\,\mathrm{V}$ and $V_{\mathrm{DS}} = 0.4\,\mathrm{V}$ for different doping levels. Legends are as in Fig. 3.7.

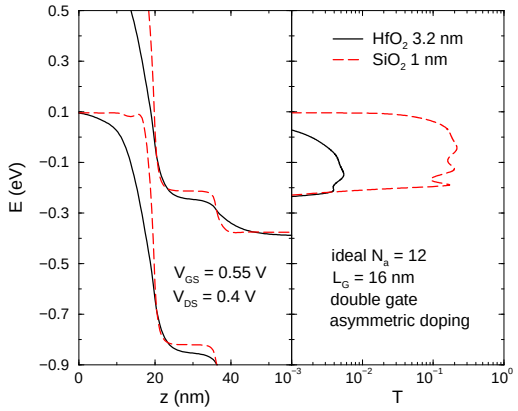

Figure 3.9: Band diagram (left) and transmission coefficient vs. energy (right) for the $N_a = 12$ ideal GNR-TFET with $V_{\mathrm{GS}} = 0.55\,\mathrm{V}$ and $V_{\mathrm{DS}} = 0.4\,\mathrm{V}$ for various types of dielectrics. Legends are as in Fig. 3.7.

The effect of removing the bottom gate is also checked by comparing SG (Fig. 3.7, blue triangles) and DG (green diamonds) topologies with the same parameters. It turns out that the DG TFET is preferable, since it leads to higher ON-currents and better SS. Regarding the performance of such devices, an ON-current of 1.89 mA/μm (Fig. 3.7, green diamonds, $V_{GS} = 0.55\,\mathrm{V}$) is obtained with an ON/OFF current ratio larger than 10^5. Hence, as compared to conventional FETs of similar width, TFETs easily provide large ON/OFF current ratios at the price of lower ON currents. Similar remarks apply to TFETs of different widths, as confirmed by the turn-on characteristics of $N_a = 13$ and $N_a = 40$

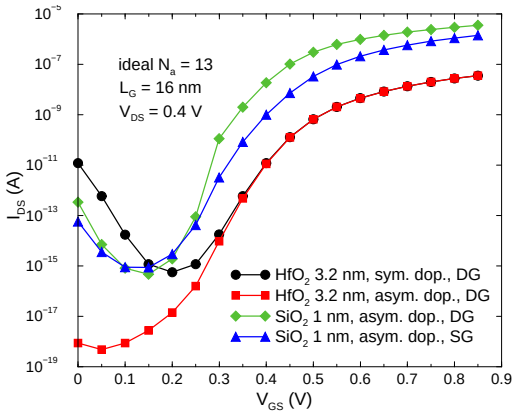

Figure 3.10: Same as in Fig. 3.7 but for a $N_a = 13$ GNR-TFET.

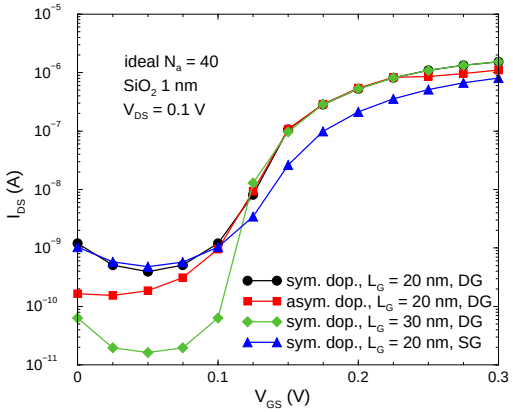

Figure 3.11: Turn-on characteristics of the ideal $N_a = 40$ GNR-TFETs with source doping molar fraction $N_S = 7 \cdot 10^{-4}$, 1 nm SiO_2 and $V_{DS} = 0.1\,V$. Legends: as in Fig. 3.7, except $N_D = 2 \cdot 10^{-4}$ for asym. dop. and the use of different gate lengths.

GNR-TFETs shown in Figs. 3.10 and 3.11, respectively. It should be noticed that the $N_a = 13$ TFET exhibits an ON/OFF current ratio of 10^9 at $V_{DS} = 0.4\,V$ which exceeds that of its $N_a = 12$ counterpart due to the slightly-larger band gap (Fig. 3.10, green diamonds). As far as the $N_a = 40$ GNR-TFET is concerned ($W_{GNR} = 4.8\,nm$, $E_G = 0.29\,eV$), the performance is in general rather poor due to the quite small band gap which forces the maximum $V_{DS} = 0.1\,V$ in order to avoid BTBT at the drain. Only the best configuration with 1 nm SiO_2 is considered for this device. Current leakage is dominated by BTBT through the channel. Increasing the gate length L_G helps suppress the leakage, as confirmed by the curve at $L_G = 30\,nm$ in Fig. 3.11. It is interesting to notice that, despite

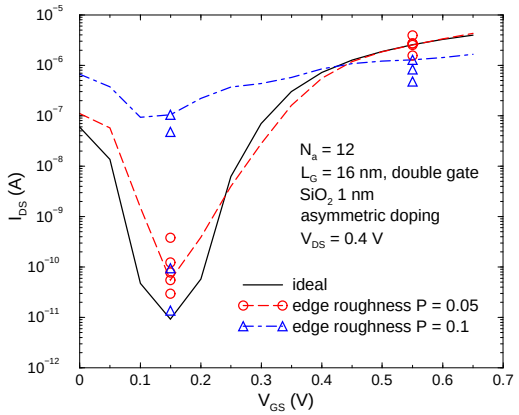

Figure 3.12: Turn-on characteristics of nominal $N_a = 12$ GNR-TFETs with edge roughness with different probabilities P (the ideal GNR corresponds to $P = 0$).

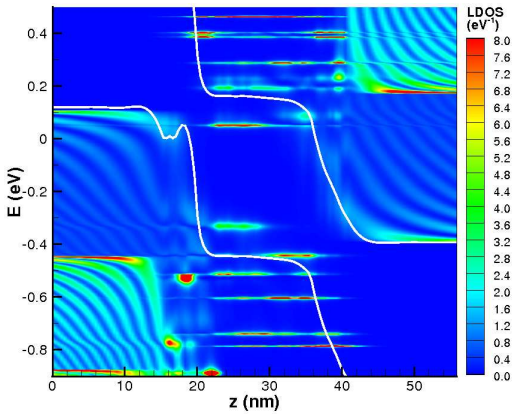

Figure 3.13: Local density of states (LDOS) integrated on each slab of the $N_a = 12$ rough GNR-TFET with $P = 0.1$, $V_{\mathrm{DS}} = 0.4\,\mathrm{V}$, $V_{\mathrm{GS}} = 0.15\,\mathrm{V}$.

the very low V_{DS}, a remarkable ON/OFF ratio larger than 10^4 can be achieved, indicating the great potential of graphene for low dynamic power applications.

Finally, the effect of edge roughness is examined for the case of the best performing nominal $N_a = 12$ GNR-TFET previously considered (Fig. 3.7, green diamonds). The edge defects are simulated by randomly adding or removing atom pairs at the two edges independently according to a predefined probability P, following the approach proposed in [38]. The turn-on characteristics for $P = 0$ (ideal case), and for two samples with $P = 0.05$ and $P = 0.1$ are plotted as lines in Fig. 3.12. It is seen that a moderate amount of defects can be tolerated, even if both the ON and OFF currents are deteriorated. However, a further increase

of roughness can lead to the impossibility of turning the device off. The reason for this can be traced back to the onset of states in the gap, which increase the BTBT through the channel, as shown by the local density of states in Fig. 3.13. Moreover, different implementations of the edge defects with the same probability P may lead to different results for the OFF and ON currents, as reported by symbols in Fig. 3.12. This effect proves a critical variability problem*.

3.3 Summary

A simulation study of both conventional and tunneling GNR-FETs has been presented.

Simulation results of conventional GNR-FETs indicate that extremely-narrow devices outperform the best Si-based transistors in terms of ON current density. However, it is also shown that GNR devices suffer a limitation in the maximum allowable supply voltage, due to the BTBT which occurs at the drain end of the channel and severely degrades the OFF leakage current. If the width is increased, the smaller energy gap limits the maximum allowable supply voltage even further. In order to achieve a minimum ON/OFF current ratio equal to 10^4, the maximum GNR width ought to be around 3.5 nm.

Some of the limitations of the conventional GNR-FETs can be removed with the TFET configuration, given the possibility of achieving an SS much better than 60 mV/dec. For ideal GNR-TFETs, high ON/OFF ratios can be obtained with the proper choice of design parameters, at the expense of a somewhat reduced ON current capability. Thus, GNR-TFETs are possible candidates for trading off high performance and low power operation. On the other hand edge roughness, unless well controlled, spoils the device performance, in particular in the OFF state, and is also responsible for a large variability problem.

*The variability is an indication of localization transport due to disorder (see also the discussion in Sect.4.4). As localization effects can be easily destroyed by room temperature dephasing effects, more realistic simulations including incoherent scattering might give different results.

Part II

PATTERN-HYDROGENATED GRAPHENE

Chapter 4

Modeling and simulation of pattern-hydrogenated graphene

In this chapter, a study of pattern-hydrogenated graphene is presented. The study is focused on investigating the potential of this material in solving the graphene bandgap problem, thus providing an alternative to the previously studied GNRs.

A large part of the current research effort on graphene is devoted to the study of the doping of graphene with different types of atoms and molecules to alter its electronic properties. The special interest on hydrogen atoms originates from an early DFT study [39], in which the full hydrogenation of graphene has been predicted to give rise to a new material, called graphane, exhibiting a bandgap of several electronvolts. In graphane, the carbon atoms acquire a sp^3 hybridization similar to the one in diamond, since the two graphene sublattices shift vertically in opposite directions, as a consequence of the bonding with hydrogen atoms on the top face, for one sublattice, and on the bottom face, for the other sublattice. The bandgap formation can be explained as a joint effect of the bonding with hydrogen atoms and the sp^3 hybridization, which together make the p_z electrons of graphene become localized around each carbon-hydrogen bond and no longer available for conduction. Since graphane behaves as an insulator, it has been suggested the intriguing possibility of patterning a GNR without using etching, but by creating two graphane regions separated by a strip of pristine graphene [40].

However, in the experiments [41], the hydrogenation turns out to be only partial and random. The reason is that only one face of graphene is accessible

for hydrogenation, preventing the formation of the complete graphane structure. Graphane-like structures, with a partial sp^3 hybridization, are only possible on top of the randomly occuring ripples, i.e. curved portions of the graphene surface. An insulating behavior of the resulting material has been observed, but its origin is debated: it could be due to an effect of localization [42, 43], a phenomenon that occurs in disordered materials as a consequence of coherent backscattering (see the discussion in Sect. 4.4), or to the spontaneous ordering of the adsorbates on the same graphene sublattice, with the consequent breaking of the symmetry between the two sublattices [44, 45].

Recently, a new experiment [12] has shown that the situation is different for graphene grown on an iridium (111) surface. Due to the slight mismatch between the lattice constant of graphene and the iridium surface, their composite structure forms a superlattice. As a consequence, the position of the ripples, instead of being random as in exfoliated graphene, coincides with specific points of the superlattice. Indeed, it has been shown experimentally that the hydrogenation occur preferentially at specific superlattice sites, leading to the formation of a periodic pattern of hydrogen clusters. By angle-photoemission spectroscopy (ARPES), a measurement by which it is possible to determine the electron distribution in energy and momentum, a bandgap opening has been observed. The origin of this bandgap has been ascribed to the confinement potential induced by the hydrogenated regions, behaving as portions of graphane, on the graphene regions that are left uncovered. Interestingly, the idea of opening a bandgap by the confinement effect of a regular array of defects is shared by the recently fabricated graphene nanomeshes (GNMs), also known as graphene antidot lattices, where the role of the hydrogen clusters is played by clusters of vacancies, i.e. holes of nanometer size inside the graphene sheet [46, 47]. The analogy between patterned hydrogenation and nanomesh will be stressed throughout the chapter.

The work reported here is a study of the bandgap opening in pattern-hydrogenated graphene by means of numerical simulations. The purpose is to reproduce the experimental bandstructure from ARPES and also to predict the transport properties of devices that use pattern-hydrogenated graphene as channel material. The transport simulation are carried out in a different way compared to the previous study of GNR-FETs: the low-temperature, near-equilibrium behaviour is investigated, in order to highlight the fundamental properties of the material, rather than the issues related to the specific device structure under consideration. The study addresses the dependence of the bandgap, as well as the conductance in the on and off states, on the parameters defining the patterned hydrogenation, i.e. the size of the superlattice unit cell and the size of the hydrogen cluster.

The chapter is organized as follows. In Sect. 4.1, the employed TB model is briefly discussed. Then, in Sect. 4.2, the atomic structure of the superlattice is clarified and the model for hydrogenation is introduced. The results of the

calculation emulating the ARPES measurement are presented in Sect. 4.3, while the ones of the transport calculation in Sect. 4.4.

4.1 Hamiltonian model

The simple tight-binding (TB) model from [42, 43] is employed to describe the composite structure of graphene with adsorbed hydrogen atoms. Within this model, the basis is made of a $2p_z$ orbital per carbon atom and a $1s$ orbital per hydrogen atom. In second-quantized notation, the Hamiltonian can be written as

$$\mathcal{H} = -\gamma \sum_{\langle l,m \rangle} c_l^\dagger c_m + \epsilon_H \sum_n d_n^\dagger d_n + \gamma_H \sum_n \left(c_{\alpha_n}^\dagger d_n + \text{h.c.} \right) , \tag{4.1}$$

where c_l (d_n) is the annihilation operator for the $2p_z$ ($1s$) orbital of the carbon (hydrogen) atom of index l (n), the first sum is restricted to nearest-neighbor atom pairs, and α_n is the index of the carbon atom bonded to the hydrogen atom of index n. The parameters describing the carbon-carbon hopping integral ($\gamma = 2.6$ eV), carbon-hydrogen hopping integral ($\gamma_H = 5.72$ eV), and hydrogen onsite energy ($\epsilon_H = 0$ eV) are taken from [43]. These couplings are pictorially represented in Fig. 4.1a. It should be noted that the use of a null ϵ_H preserves particle-hole symmetry, i.e. the symmetry between the conduction and valence bands.

This simple model does not account for the local change in hybridization of the carbon atoms from sp^2 to sp^3, induced by the bonding with hydrogen atoms, nor the difference between a hydrogen atom on the top or on the bottom side of the graphene sheet. Nevertheless, it captures the essential physics of the hydrogenation process, that is the removal of the p_z orbital of the hydrogenated carbon atom from the graphene π and π^* bands. Indeed, as explained in [42], the effect of each hydrogen atom at energy E can be recast in a effective retarded

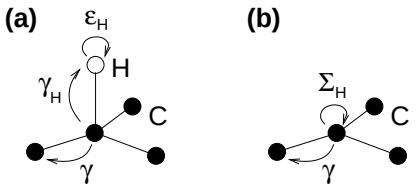

Figure 4.1: (a) Pictorial representation of the Hamiltonian model: black (whites) balls stand for carbon (hydrogen) atom; the arrows represent the different types of coupling between the corresponding orbitals. (b) Equivalent model, where the hydrogen atom is removed and its effect is included as an onsite self-energy Σ_H for the orbital of the attached carbon atom.

self-energy

$$\Sigma_H = \frac{\gamma_H^2}{E + \mathrm{i}\eta - \epsilon_H} \tag{4.2}$$

for the attached carbon orbital (Fig. 4.1b). Using the parameters above, it follows $\Sigma_H > 30$ eV for $0 < |E| < 1$ eV, that is a huge equivalent onsite potential, which effectively turns the hydrogenated carbon atom into a vacancy. This suggests the analogy between patterned hydrogenation and nanomesh.

4.2 Hydrogenation model

The interaction with the iridium substrate is neglected in the TB model. However, the substrate is taken into account for the generation of the hydrogen atoms. As anticipated above, graphene and iridium form a superlattice, due to the mismatch between their respective lattice constants: 10×10 graphene unit cells are commensurate with 9×9 iridium unit cells [48], giving rise to the superlattice unit cell represented in Fig. 4.2. Interestingly, the supercell preserves the symmetry of the graphene unit cell, that is can be divided in two regions that are equivalent to each other under reflection and exchange of the two graphene sublattices: the resulting superlattice is therefore of the honeycomb type. Denoting the superlattice with the rational number m/n, where m and n are the size of the supercell in units of the graphene and substrate lattice constants, respectively ($m/n = 10/9$ for graphene on iridium), it can be proved (see Sect. A.1) that the generation of a honeycomb superlattice is the consequence of m/n being equal to $(3M+1)/(3N)$ with $M, N \in \mathbb{Z}^+$.

It has been shown experimentally [12] that the hydrogen clusters tend to to form around the supercell regions that are highlighted by circles in Fig. 4.2, where

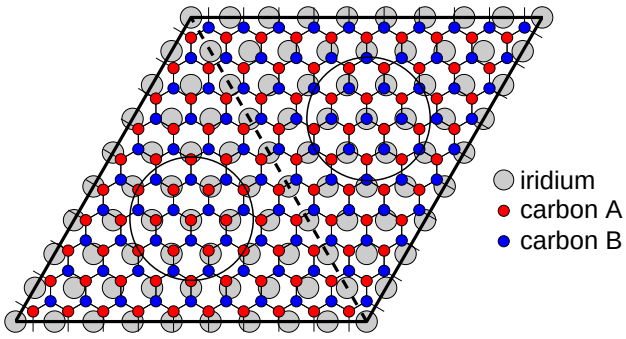

Figure 4.2: Top view of the supercell of graphene on iridium substrate. The two graphene sublattices are indicated with different colors. The supercell is symmetric under reflection across the dashed line, except for the interchange of the two graphene sublattices. The two circles highligth the regions of the supercell where the clusters tend to form.

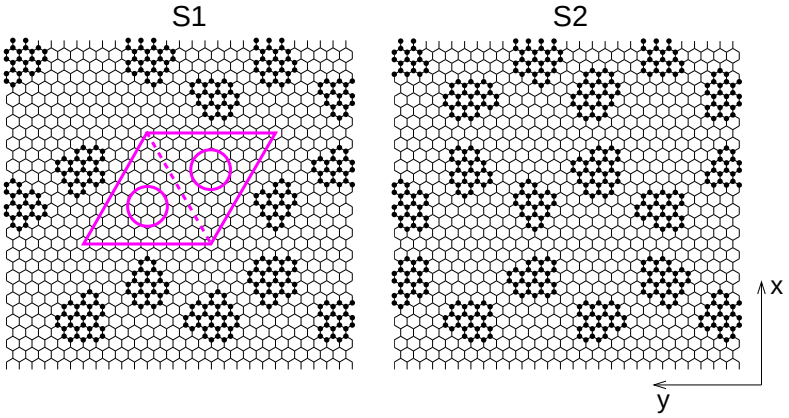

Figure 4.3: Top view of two hydrogenated samples with different cluster concentration. Hydrogen atoms are represented as black dots on the honeycomb graphene lattice and the iridium substrate is not shown. S1 is obtained with the model parameters $N_w = 4$, $n_c = 0.75$, while S2 with $N_w = 4$, $n_c = 1$. The highlighted region corresponds to a superlattice unit cell (Fig. 4.2).

one graphene sublattice sits on top of iridium atoms, while the other sublattice lies in between. The physical reason is that, in these regions, the graphene sheet can assume a local sp^3 hybridization similar to graphane, alternatively binding to hydrogen atoms on the top side and to iridium atoms on the bottom side.

Here, a hydrogenation model is developed to reproduce this preferential adsorption (details in Sect. A.2). The model takes as input two parameters: a discrete quantity N_w, which represents the cluster radius, and the cluster concentration n_c, which is equal to the ratio between the number of clusters and the number of half supercells. Two hydrogenated samples, generated with the same value of N_w but different n_c, are depicted in Fig. 4.3. Disorder is introduced both at the lattice level, i.e. the clusters have irregular edges, and at the superlattice level if $n_c < 1$, i.e. some clusters are randomly missing from the superlattice. It can be noticed that this model puts hydrogens atoms on top of both graphene sublattices, in contrast with the statement above that only one sublattice is expected to bind to hydrogen atoms. However, the doping of both sublattices allows to avoid the formation of defects, made of carbon atoms having two or three nearest neighbors being hydrogenated, that would otherwise result in pseudo dangling bonds (see the discussion in Sect. A.2).

In the following, it will be considered also the case of a bigger supercell, obtained by substituting iridium with a fictitious substrate with different lattice constant, so that 13×13 graphene unit cells are commensurate with 12×12 substrate unit cells (according to the rule provided above, this choice results again in a honeycomb superlattice). The cases of iridium and fictitious sustrate will be denoted as SL10 and SL13, respectively.

4.3 Results of "ARPES" simulation

In order to study the electronic properties of pattern-hydrogenated graphene, the calculation of the number of states per unit energy and unit momentum is performed [45]. This quantity is given, apart from a normalization factor, by the diagonal elements of the spectral function in momentum space, $A(\mathbf{k},\mathbf{k};E)$ ($\mathbf{k}$ being the momentum over $\hbar$ and E the energy). While this quantity becomes simply a measure of the bandstructure for periodic systems, it is a general concept, valid also for disorded systems, and, most importantly, it is the physical quantity measured by ARPES. A formal introduction to the $A(\mathbf{k},\mathbf{k};E)$ concept is given in App. B.

The simulation is done on samples composed of $N_1 \times N_2$ graphene unit cells ($N_1 = N_2 = 120$ for the SL10 case, $N_1 = N_2 = 117$ for the SL13 case) and periodic conditions are imposed on the boundaries. The calculation starts by computing the spectral function in real space $A(\mathbf{l},q;\mathbf{l}',q';E)$ (with $\mathbf{l}$ the graphene lattice vector and q the orbital index inside each graphene unit cell) and then by Fourier transforming the result to get $A(\mathbf{k},\mathbf{k};E)$, according to the formula

$$A(\mathbf{k},\mathbf{k};E) = \frac{1}{N_1 N_2} \sum_{q} \sum_{\mathbf{l}_1} \sum_{\mathbf{l}} e^{-\mathrm{i}\mathbf{k}\cdot\mathbf{l}} A(\mathbf{l}_1,q;\mathbf{l}_1-\mathbf{l},q;E)\,, \tag{4.3}$$

where only carbon orbitals are considered ($q = 1, 2$). When plotting this quantity, an additional prefactor $(a/2\pi)^2(\sqrt{3}/2)$ is used in front of (4.3), so that $A(\mathbf{k},\mathbf{k};E)/(2\pi)$ gives the number of states per unit energy, per unit $\mathbf{k}$, and *per graphene unit cell*. While in [45] the calculation of the spectral function in real space is done using wavefunctions, here the Green's function formalism [18] is used, together with a novel recursive algorithm for periodic structures (see Sect. C.1).

In Fig. 4.4, the calculated average $A(\mathbf{k},\mathbf{k};E)$, for two ensembles corresponding to the two realizations shown in Fig. 4.3, is plotted along a path in k-space that includes the graphene K point. It should be noted that, since particle-hole symmetry is preserved by the used TB model, the result for positive E can be simply obtained by mirroring the result for negative E. The two plots are directly comparable with Figs. 1b,c in [12], where the experimental ARPES for two different times of exposure to hydrogen is shown. From this comparison, it can be seen that data from simulations and experiment display similar features: in both cases the two valence branches, which for pristine graphene would have intersect at the Dirac point, seem to intersect at a lower energy; also, the signal of the states lying at the K point between $E = 0$ and the intersection energy gets suppressed with increasing hydrogen doping. Both these features can be interpreted as a bandgap opening. Interestingly, the absence of a clear repeated dispersion relation, which would be expected for a periodic superlattice structure, is confirmed by simulations: this indicate a strong effect of disorder. The presence

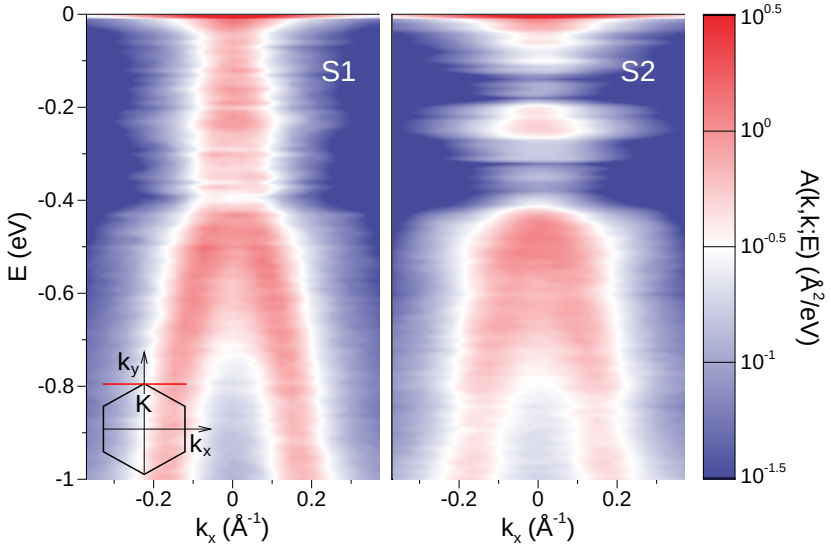

Figure 4.4: Calculated number of states per unit energy and unit **k** for two sets of hydrogenated samples that correspond to the cases S1 and S2 shown in Fig. 4.3. 50 samples are considered for each set, the plotted quantity being the average. The inset shows the direction within the graphene Brillouin zone along which the calculation is performed.

of the flat band at $E = 0$ in the simulation results is a well-known effect of the imbalance between the two graphene sublattices [49]: the absence of these states in the experimental ARPES could be related to bond relaxation and sp^3 hybridization, which are neglected in the simulations.

Here, it is proposed to define the bandgap edge as the energy corresponding to the intersection point. The bandgap is extracted for different sets of samples, corresponding to different values of cluster size, cluster concentration, and supercell size. The technique used for the extraction consists in a least-square fitting of the $A(\mathbf{k}, \mathbf{k}; E)$ intensity within a manually chosen range of energies (details in A.3). Different fitting curves are employed according to the shape of $A(\mathbf{k}, \mathbf{k}; E)$, as shown in Fig. 4.5. In order to find a universal law for the scaling of the bandgap with the various parameters, the extracted bandgap values (together with a measure of the broadening of each $A(\mathbf{k}, \mathbf{k}; E)$ plot as error bar) are plotted against the quantity ${N_H}^{1/2}/N_C$, where N_H and N_C are the average number of hydrogen and carbon atoms in the half supercell (Fig. 4.6). This is motivated by the fact that, for the case of triangular GNMs, a general relation $E_g \propto {N_{\text{rem}}}^{1/2}/N_{\text{tot}}$ at low defect concentration has been proposed [46], where N_{rem} and N_{tot} are the corresponding quantities of N_H and N_C for the nanomesh case, i.e. the number of removed atoms and the number of total atoms (before formation of the nanomesh) in the supercell, respectively. In [50], it was stated

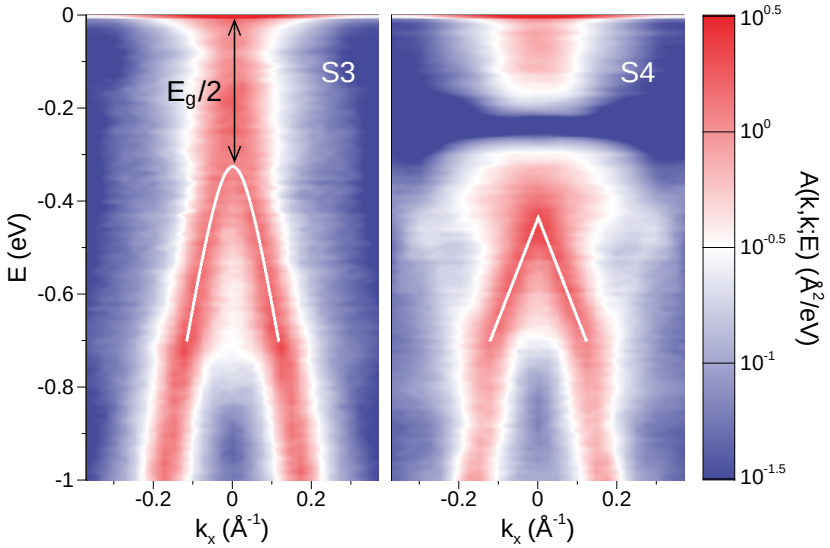

Figure 4.5: Number of states per unit energy and unit **k** for two set of hydrogenated samples corresponding to two different cluster sizes, i.e. N_w. Different fitting curves are used (white lines). The bandgap is extracted with respect to the fitting curve.

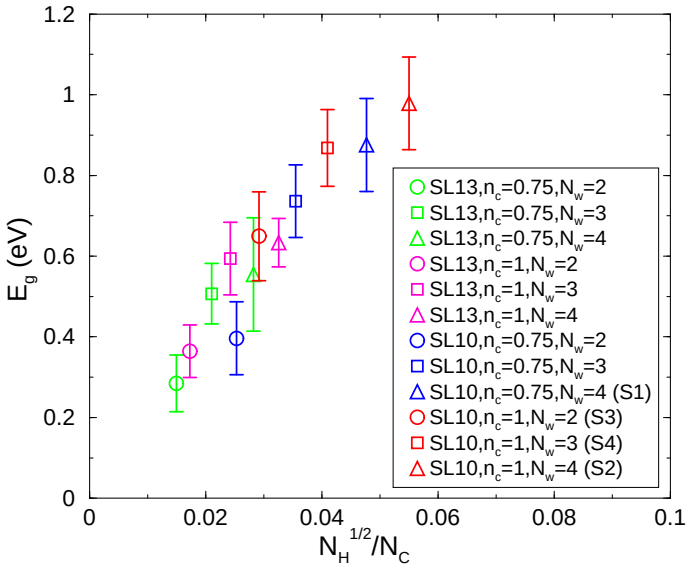

Figure 4.6: Bandgap extracted for the various sets of samples and plotted as a function of $N_H{}^{1/2}/N_C$, where N_H and N_C are the average number of hydrogen and carbon atoms in the half supercell, respectively. SL10 stands for graphene on iridium substrate (supercell made of 10×10 graphene unit cells, see Fig. 4.2), while SL13 refers to graphene on a fictitious substrate (supercell made of 13×13 graphene unit cells). The error bar is a measure of the broadening of the $A(\mathbf{k}, \mathbf{k}; E)$ plot.

that this relation does not hold for honeycomb GNMs, due to the presence of three different superlattice families (similar to what is predicted for graphene nanoribbons [20]). However, Fig. 4.6 suggests that, when disorder is included in the simulations, the scaling law $E_g \propto {N_H}^{1/2}/N_C$ can be valid at low defect coverage for honeycomb superlattices as well. By recalling the linear dispersion relation of graphene, $E \propto (k_x^2 + k_y^2)^{1/2}$, with $\mathbf{k}$ the wavevector with respect to the K point, and by applying the usual quantization rule $k_x^{(1)} = k_y^{(1)} = \pi/\Delta$ for a particle in a box of size Δ, one obtains $E_g \propto 1/\Delta$. The quantity $N_C/{N_H}^{1/2}$ can thus be interpreted as an effective (normalized) confinement length.

4.4 Results of conductance simulation

It is interesting to investigate the transport properties of pattern-hydrogenated graphene, both because successful techniques to transfer graphene grown on metal surfaces to insulating substrates have been recently developed [6], and because of the analogy with graphene nanomesh, for which field-effect transistors have been already fabricated [47]. Therefore, a three-terminal structure such as the one represented in Fig. 4.7a is considered: the purpose is to predict its low-temperature, low-bias conductance.

Contrary to previous simulations of GNRs, the electrostatic potential is not self-consistently calculated: as stated before, the emphasis is here on investigating the material properties rather than accurately simulating a device structure. As shown in Fig. 4.7b, a schematic profile of the potential energy along the device is assumed: the potential energy in the source and drain leads is kept fixed with respect to the Fermi level E_F, while the height V_{ch} of a square barrier in the channel region is varied to emulate the effect of the back gate. Graphene is

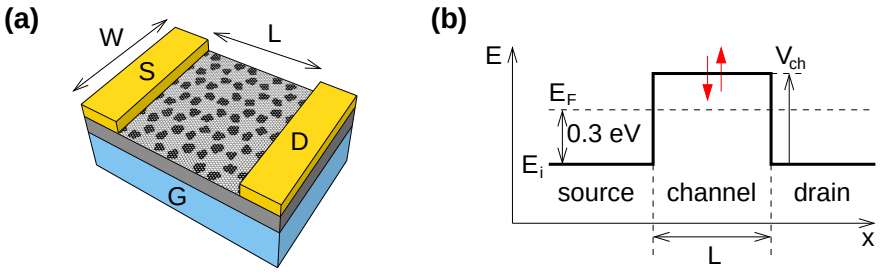

Figure 4.7: (a) Conceptual device under investigation: pattern-hydrogenated graphene is transferred to an insulating substrate and used as channel material of a field-effect transistor. (b) Profile of the potential energy used to simulate the structure in (a): the Fermi level in the leads E_F is kept fixed, while the barrier height V_{ch} is varied to reproduce the effect of the back gate. Pristine graphene is used for the leads.

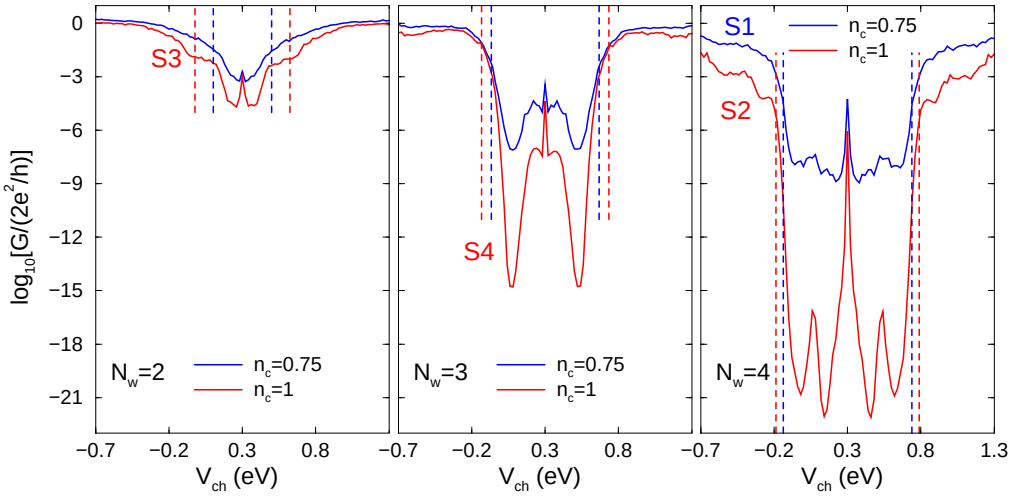

Figure 4.8: Zero-temperature conductance vs $V_{\rm ch}$ for various sets of samples with $W = L = 30$ nm and iridium substrate (SL10). From left to right, the cluster size, i.e. N_w, is increased; within the same plot, the cluster concentration n_c is varied. 100 samples are considered for each set and the average is done on the logarithm of the normalized conductance (a motivation for this type of averaging can be found in [51]). The vertical lines indicate the bandgap from Fig. 4.6.

aligned with its armchair direction along the longitudinal direction of the device, in order to avoid edge effects; only the channel is hydrogenated, the leads being made of pristine graphene. The zero-temperature conductance, proportional to the transmission function at $E = E_F$, is computed by using the standard Green's function technique [18]. A modified version of the algorithm in [24] is used to calculate the lead self-energies (see Sect. C.2).

Fig. 4.8 shows the simulated, ensemble averaged zero-temperature conductance versus $V_{\rm ch}$. The device size is kept fixed at $W = L = 30$ nm, while different sets of hydrogenated samples (all belonging to the SL10 case) are considered. It can be seen that patterned hydrogenation leads to a clear transport gap, increasing with N_w and n_c. Also, the transport simulations agree well with the previous "ARPES" results: the transport gap matches the bandgap from the $A(\mathbf{k}, \mathbf{k}; E)$ fitting (whose extension is indicated by vertical lines in Fig. 4.8 and the peaks in the transport gap region correspond to the gap states in $A(\mathbf{k}, \mathbf{k}; E)$. Interestingly, the G vs $V_{\rm ch}$ curve appears symmetrical, unlike what happens for pristine graphene [52].

It can be noticed that the conductance hardly reaches the quantum of conductance $2e^2/\hbar$ even in the on state, that is for $V_{\rm ch}$ values far away from the gap region. This is an indication of localization transport, which is commonly believed to occur in disordered materials, when the phase relaxation length l_ϕ is

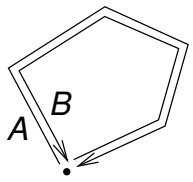

Figure 4.9: An electron undergoes several scattering events due to a random potential and comes back to the original position. Path B is the time-reversed version of path A, and vice versa.

much longer than the mean free path [53]. In this situation, as a consequence of quantum inteference, the probability for backscattering gets increased compared to the classical case, so that Ohm's law, i.e. $G \propto W/L$ in two dimensions, is not valid anymore.

To understand the physical reason for the increased backscattering probability, consider a case as the one illustrated in Fig. 4.9, where an electron starts its motion from a given position, scatters several times, and comes back to the starting position. Even in the classical picture, many trajectories starting and finishing at the same point are possible, due to the randomness of the scattering potential: according to the statistical approach, one has to associate a probability to each path and then sum the individual probabilities to get the overall probability for backscattering P. Considering a path A and its time-reversed counterpart B, one gets $P_{\rm cl} = P_A + P_B$, or, by introducing probability amplitudes, $P_{\rm cl} = |\psi_A|^2 + |\psi_B|^2$. If time-reversal symmetry is satisfied, then $\psi_A = \psi_B$ and thus $P_{\rm cl} = 2|\psi_A|^2$. Instead, in the quantum mechanical picture, one has to sum probability amplitudes instead of probabilities: this gives $P_{\rm qu} = |\psi_A + \psi_B|^2 = 4|\psi_A|^2$, that is twice the classical result.

One way to confirm the localization regime is to see how G changes with L, since the theory for localization predicts $G \propto \exp(-L/\xi)$, where ξ is the localization length. Focusing on the devices with complete clustering ($n_c = 1$), the simulations above are repeated for larger L: Fig. 4.10a collects the results of the extraction of the localization length at the various bias points, obtained by linear fitting the dependence on L of the logarithm of the normalized conductance, as shown in Fig. 4.10b for two particular $V_{\rm ch}$ values. The plots show that all samples are in the strong localization regime in the whole energy range under consideration. Also, the values of the localization length for the gap and band states are well separated from each other if $N_w < 4$. To illustrate this point, the average value of the localization length in the off and on state is extracted and plotted against ${N_H}^{1/2}/N_C$, as it has been done previously for the bandgap (Fig. 4.11, see caption for the definition of the on and off states). Samples belonging to the SL13 case are also included. It can be noticed that, for almost all the samples, the value of the localization length in the off state is about one order of magni-

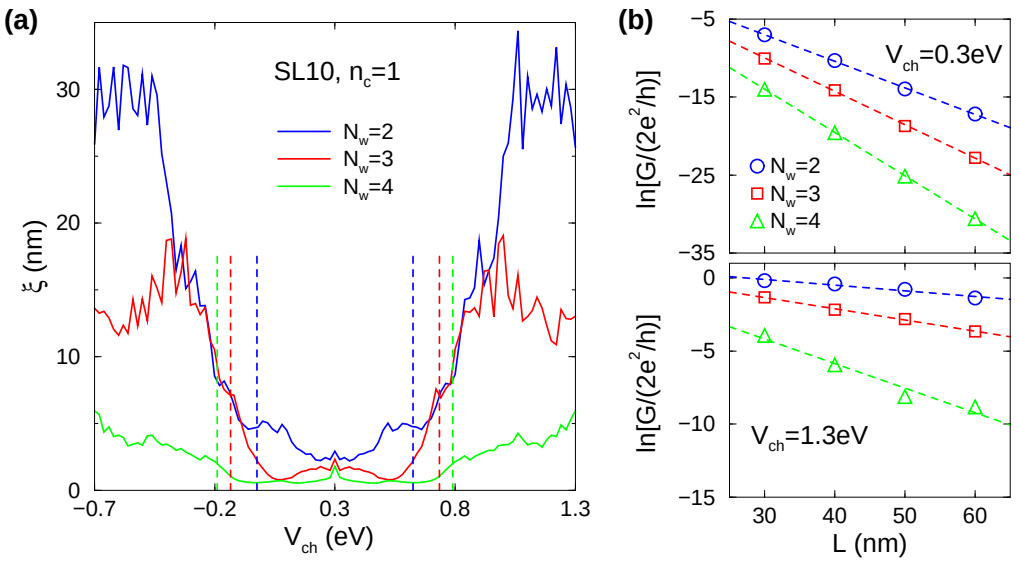

Figure 4.10: (a) Localization length vs $V_{\rm ch}$ for sets of samples with different cluster size and fixed supercell size (SL10) and cluster concentration ($n_c = 1$). The vertical lines indicate the bandgap from Fig. 4.6. (b) Example of the localization length extraction at two different $V_{\rm ch}$ points. The dashed lines indicate the fitting with the formula $\ln[G/(2e^2/h)] = \ln g_0 - L/\xi$.

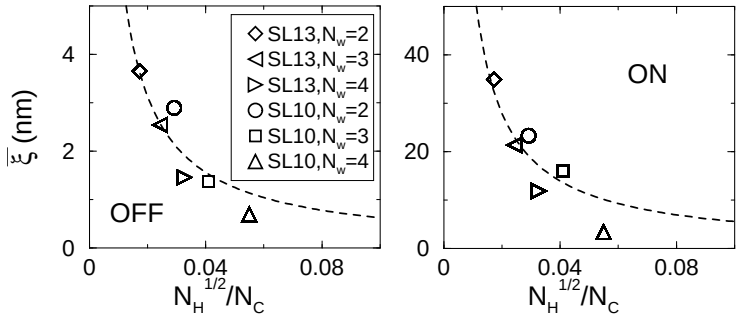

Figure 4.11: Average value of the localization length in the off and on state for various sets of samples with different supercell and cluster sizes, plotted as a function of ${N_H}^{1/2}/N_C$. The dashed lines indicate the fitting curve $\bar{\xi} \propto N_C/{N_H}^{1/2}$. The off state is defined as the bias region $|V_{\rm ch} - E_F| < E_G/2 - B$, where B is the half broadening from Fig. 4.6, while the on state as 0.65 eV $< |V_{\rm ch} - E_F| <$ 0.75 eV.

tude smaller than the corresponding value in the on state (values smaller than about 1 nm could also be due to ballistic transport through evanescent states from the leads [54]). Furthermore, in both bias regions, the average localization length seems to follow the general scaling law $\bar{\xi} \propto N_C/{N_H}^{1/2}$, provided that the hydrogenation is not too high. This relation appears reasonable by recalling the meaning of an effective confinement length that has been attributed to $N_C/{N_H}^{1/2}$, and the fact that the confinement is two-dimensional, thus including also the transport direction. By comparing the value of ξ with l_ϕ, one can estimate if the localization regime can persist in the presence of dephasing effects: for this to happen, the condition $\xi \ll l_\phi$ must be satisfied. The value of l_ϕ varies with temperature, since the various scattering mechanisms that are responsible for it are temperature dependent. Magnetotransport experiments indicate that the phase-relaxation length in graphene decreases from about 100 to 30 nm when the temperature is raised from 0.4 to 70 K [55]. The values reported in Fig. 4.11 therefore suggest that transport through the band states is likely to become diffusive at room temperature. However, since the values of the localization length in the off state are much lower, there is a chance that transport through the gap states will remain localized.

4.5 Summary

In conclusion, in this work, a realistic modeling of pattern-hydrogenated graphene, based on a simple TB Hamiltonian, has been presented. The model has been validated by direct comparison of the calculated k-resolved density of states in energy with the experimental ARPES. The bandgap opening has been studied as a function of the parameters describing the patterned hydrogenation. Transport simulations at zero temperature have confirmed the bandgap opening and clarified the localization nature of transport through both gap and band states. The results indicate that the off state could be preserved even at room temperature.

Conclusions

In this thesis, graphene nanoribbons and patter-hydrogenated graphene, two alternatives for opening an energy gap in graphene, have been investigated through numerical simulations.

A code has been developed for the simulation of GNR-FETs, employing a full-quantum TB NEGF model. To speed up the simulations, the NPEM model and the MS TB method have been developed and extensively validated against the full TB model. The accuracy and efficiency of the two approaches have been shown to be very good. The code has been used for simulation studies of both conventional and tunneling FETs. The simulations have shown that conventional narrow GNR-FETs outperform silicon devices in terms of ON current capability; on the other hand, the OFF state is degraded by leakage related to tunneling mechanisms. When the width of the devices is made larger, the problem become more severe due to the smaller band gap, resulting in low ON/OFF current ratios. The tunneling FET architecture can partially solve these problems thanks to the improved subthreshold slope; however, it has also been shown that a very good control of edge roughness is needed for preserving the OFF state performance. The code can be improved with the inclusion of incoherent scattering mechanisms, such as electron-phonon interactions, in order to achieve more realistic simulation results.

In the second part of this thesis, patter-hydrogenated graphene has been simulated by means of a TB model. A realistic model for patterned hydrogenation, including disorder, has been developed. The model has been validated by direct comparison of the k-resolved density of states in energy with the experimental ARPES. The scaling of the energy gap and the localization length on the parameters determining the pattern geometry have been also presented. The results have suggested that a transport gap of 1 eV should be attainable with experimentally achievable hydrogen concentration. The study presented here can also be relevant to graphene nanomesh, which shares similar properties with patterned hydrogenation.

Appendices

Appendix *A*

Details on the modeling of patterned hydrogenation

In this appendix, more details regarding the study of pattern-hydrogenated graphene are given. In Sect. A.1, the conditions for obtaining a honeycomb superlattice are discussed. In Sect. A.2, the model for the generation of the hydrogen atoms is explained in detail. Finally, in Sect. A.3, the procedure followed for the extraction of the bandgap (and the broadening) from the $A(\mathbf{k}, \mathbf{k}; E)$ plots is presented.

A.1 Triangular versus honeycomb superlattice

Figs. A.1a and b show the unit cell for the honeycomb graphene lattice and the typical triangular substrate surface layer, respectively. The substrate layer could be an Ir(111) [48] or Ru(0001) [56] surface, as both could accomodate a monolayer graphene on their surface. The composite system forms a highly ordered Moiré pattern, i.e. a superlattice, which can be of the honeycomb or triangular type. In this paper, we are interested in the former, and this section outlines the necessary criterion for its generation.

We assume that a $m \times m$ graphene supercell is commensurate with a $n \times n$ substrate supercell. Therefore, denoting the lattice vectors of graphene, substrate and superlattice by $\mathbf{a}_j$, $\mathbf{b}_j$, and $\mathbf{c}_j$ $(j = 1, 2)$, respectively (see Fig. A.1), we have

$$\mathbf{c}_j = m\mathbf{a}_j = n\mathbf{b}_j \,, \tag{A.1}$$

where $m, n \in \mathbb{Z}^+$. Each pair (m, n) and its multiples map to a unique composite system, e.g. $(4, 3)$ is the same as $(8, 6)$. Hence, we consider only the case where m and n are prime to each other, so that $\mathbf{c}_j$ are the primitive lattice vectors of the superlattice.

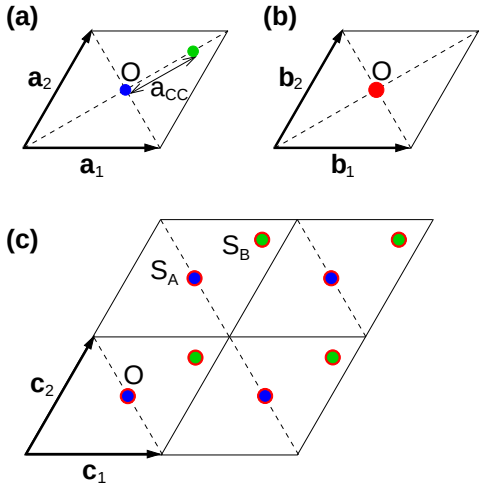

Figure A.1: (a) Graphene unit cell: the two carbon atoms are indicated with different colors. (b) Substrate unit cell. (c) Honeycomb superlattice generated by the superposition of the graphene and substrate lattices. S_A (S_B) is the point inside the supercell where a carbon atom of the A (B) graphene sublattice sits on top of an iridium atom.

We further assume that, at some point O inside the supercell, a carbon atom sits directly on top of a substrate atom: such arrangement was found to be an energetically stable configuration [48]. The superlattice points that are equivalent to O are denoted as S_A in Fig. A.1c.

In order to generate a honeycomb superlattice, there must be another point S_B inside the supercell, where a carbon atom belonging to the opposite sublattice sits on top of a substrate atom. Also, for the superlattice to be regular, it can be derived that the distance between S_A and S_B must be equal to $|\mathbf{c}_1 + \mathbf{c}_2|/3$. Inspecting the graphene lattice tells us that S_A and S_B have to be separated by a distance of $(3M+1)a_{\mathrm{CC}}$, where $M \in \mathbb{Z}^+$ and a_{CC} is the carbon-carbon distance. Hence, we can write

$$\begin{aligned} \tfrac{1}{3}|\mathbf{c}_1 + \mathbf{c}_2| = \tfrac{m}{3}|\mathbf{a}_1 + \mathbf{a}_2| = (3M+1)a_{\mathrm{CC}} \\ \Rightarrow m = 3M+1, \quad M \in \mathbb{Z}^+ . \end{aligned} \tag{A.2}$$

In a similar fashion for the substrate, the S_A and S_B have to be separated by a distance of Na_{SS}, where $N \in \mathbb{Z}^+$ and a_{SS} is the interatomic distance of the substrate. We can then write

$$\begin{aligned} \tfrac{1}{3}|\mathbf{c}_1 + \mathbf{c}_2| = \tfrac{n}{3}|\mathbf{b}_1 + \mathbf{b}_2| = Na_{\mathrm{SS}} \\ \Rightarrow n = 3N, \quad N \in \mathbb{Z}^+ . \end{aligned} \tag{A.3}$$

In conclusion, the superlattice with the similar honeycomb structure as graphene, shown in Fig. A.1c, can be generated by satisfying Eqs. A.2-A.3. Otherwise, the

superlattice would produce a triangular structure instead, with only repeated units of S_A.

A.2 Model for patterned hydrogenation

Let every carbon atom be denoted by the pair of indexes (l, i), where l is the index of the *half* supercell to which it belongs and i is the atom index inside the supercell. We consider a supercell alignment such as the one represented in Fig. 4.2, where the points S_A and S_B (see Sect. A.1) lie on symmetric points of the supercell, so that the half supercells are the triangular regions around S_A and S_B. We introduce a binary random variable $Z_{l,i} \in \{0, 1\}$ to describe the hydrogenation of each carbon atom: the atom is hydrogenated when $Z_{l,i} = 1$. We then write $Z_{l,i}$ as the product of other two binary random variables X_l and Y_i, whose probability distribution is given below.

X_l is used to generate the superlattice disorder, that is to make sure that some clusters of hydrogens are randomly missing from the superlattice. The probability $P(X_l = 1)$ is set equal to the input parameter n_c, which therefore assumes the meaning of the ratio between the average number of generated clusters and the number of half supercells.

Y_i, instead, controls the cluster formation inside each supercell. We propose the following *ansatz* for the probability $P(Y_i = 1)$ that the carbon atom of index i is hydrogenated:

$$P(Y_i = 1) \equiv f(w_i)\,, \quad f(w_i = 0) = 0\,, \quad \frac{df}{dw_i} \geq 0\,, \tag{A.4}$$

w_i being a quantity defined for each carbon atom as

$$w_i = \frac{d_i \left| d_i - \frac{1}{3} \sum_{\langle j \rangle} d_j - c \right|}{a_{\mathrm{CC}}^2}\,, \tag{A.5}$$

where d_i is the xy-plane distance between the carbon atom of index i and its nearest-neighbor substrate atom (let $\mathbf{r}$ be the position vector in the xy-plane parallel to the surface),

$$d_i = \min_k \left| \mathbf{r}_{C_i} - \mathbf{r}_{S_k} \right|\,, \tag{A.6}$$

the summation over j is restricted to the three carbon atoms that are nearest neighbor to the carbon atom of index i, and c is simply a constant,

$$c = \frac{a_{\mathrm{SS}}}{\sqrt{3}} - \sqrt{\frac{a_{\mathrm{SS}}^2}{3} + a_{\mathrm{CC}}^2 - \frac{a_{\mathrm{SS}} a_{\mathrm{CC}}}{\sqrt{3}}}\,. \tag{A.7}$$

Eqs. (A.4–A.5) can be justified by the following considerations. Experimentally, the hydrogen clusters tend to form around the regions where one graphene

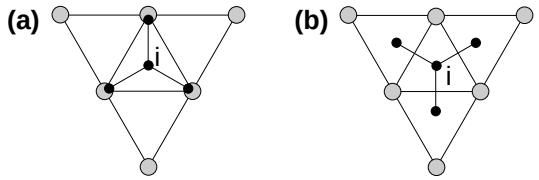

Figure A.2: Best (a) and worst (b) cases for the probability of hydrogenation of a carbon atom of index i located at a distance $d_i = a_{SS}/\sqrt{3}$ from the nearest substrate atoms. Carbon (substrate) atoms are represented with gray (black) balls.

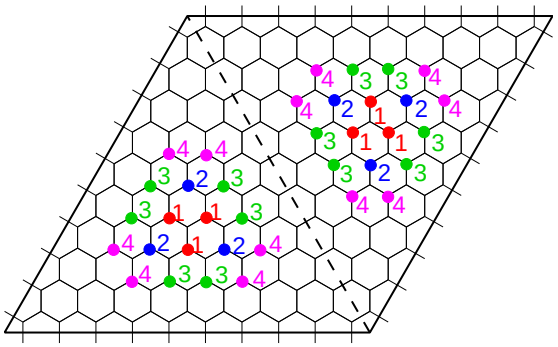

Figure A.3: Supercell of graphene on iridium: location of the carbon atoms with the four largest values of w_i, i.e. $w_i = w^{(1)}$, $w_i = w^{(2)}$, etc.

sublattice is located on top of substrate atoms, while the other sublattice is far from substrate atoms and can bind to hydrogen atoms on the top face. This translate in two conditions for the generic carbon atom to be hydrogenated. First, it should be located in between substrate lattice sites. The probability for adsorption whould then increase as its distance d_i from the nearest-neighbor substrate atom increases. This effect is captured by the prefactor in Eq. (A.5). However, if the considered carbon atom is located at the maximum distance from substrate atoms, equal to $a_{SS}/\sqrt{3}$, the probability for adsorption should distinguish between the case in which the three nearest-neighbor carbon atoms are located close to substrate atoms (high probability, Fig. A.2a) and the case in which also the three nearest neighbors are between substrate atoms (low probability, Fig. A.2b). We can note that in the first case $d_i \gg \frac{1}{3}\sum_{\langle j \rangle} d_j$, while in the second case $d_i \sim \frac{1}{3}\sum_{\langle j \rangle} d_j$. This explains the second factor in Eq. (A.5), where the constant c serves only to set the probability to 0 for the worst case (Fig. A.2b).

In Eq. (A.4) we have omitted the actual functional dependence of $P(Y_i = 1)$ on w_i. Since this relationship depends on the physical hydrogenation process and it is unknown, we choose here a simple cut-off model. For a given superlattice

unit cell, all the possible values of w_i are computed and labeled in decreasing order as $w^{(1)}, w^{(2)}, \ldots$ (the location of the corresponding carbon atoms is shown in Fig. A.3 for the case of iridium substrate). Then, the probability $P(Y_i = 1)$ is assigned as

$$P(Y_i = 1) \equiv f(w_i) = \begin{cases} 1 & \text{if } w_i = w^{(j)} \text{ with } j < N_w, \\ 0.5 & \text{if } w_i = w^{(j)} \text{ with } j = N_w, \\ 0 & \text{if } w_i = w^{(j)} \text{ with } j > N_w. \end{cases} \tag{A.8}$$

With this method, a cluster of hydrogen is formed around the sites where the quantity w_i tends to grow (i.e. around S_A and S_B). The input parameter N_w controls the size of this cluster. The disorder is only located at the cluster edges.

The hydrogenation model described above produces clusters inside which only one graphene sublattice is hydrogenated. This leads to the formation of midgap states in the electronic structure, associated with dangling bonds. However, these states are believed to be an artefact of the TB model, due to the fact that bond relaxation is neglected. To avoid this, after hydrogen atoms are generated according to the method described above, a final step is introduced: additional hydrogen atoms are placed on top of the carbon atoms that have two or three nearest neighbors being hydrogenated.

A.3 Procedure for bandgap extraction

The bandgap is extracted from each (ensemble-averaged) $A(\mathbf{k}, \mathbf{k}; E)$ plot using a fitting technique. We recall that the path in k-space is the one shown in the inset of Fig. 4.4, so that $\mathbf{k} = (k_x, K_y)$, where K_y is the k_y coordinate of the K point. Hence, we use the simplified notation $A(k_x, k_x; E)$. The fitting procedure is composed of the following steps.

1. Manually choose a range of energies $[E_1, E_2]$ where to apply the fitting.

2. Find for each energy $E \in [E_1, E_2]$ the k_x coordinate where the intensity is maximum, separately for positive and negative k_x:

$$k_x^+(E) \quad \text{such that} \quad A(k_x^+, k_x^+; E) = \max_{k_x \geq 0} A(k_x, k_x; E)\,, \tag{A.9}$$

$$k_x^-(E) \quad \text{such that} \quad A(k_x^-, k_x^-; E) = \max_{k_x \leq 0} A(k_x, k_x; E)\,. \tag{A.10}$$

3. Compute for each $E \in [E_1, E_2]$ the values $w^+(E)$ and $w^-(E)$ as follows

$$w^+(E) = \frac{A\left(k_x^+(E), k_x^+(E); E\right)}{\max_{E' \in [E_1, E_2]} A\left(k_x^+(E), k_x^+(E); E'\right)}\,, \tag{A.11}$$

$$w^-(E) = \frac{A\left(k_x^-(E), k_x^-(E); E\right)}{\max_{E' \in [E_1, E_2]} A\left(k_x^-(E), k_x^-(E); E'\right)}\,. \tag{A.12}$$

4. Apply a least-square fitting to the set of points $\{(E, k_x^+(E))\}_{E\in[E_1,E_2]} \cup \{(E, k_x^-(E))\}_{E\in[E_1,E_2]}$, by using $w^+(E)$ and $w^-(E)$ as weights and one of the following dispersion relations as fitting curve:

$$E = \pm\left(\hbar v|k_x| + \frac{E_g}{2}\right), \tag{A.13}$$

$$E = \pm\left(\frac{\hbar^2 k_x^2}{2m} + \frac{E_g}{2}\right), \tag{A.14}$$

$$E = \pm\sqrt{\frac{\hbar^2 E_g k_x^2}{2m} + \left(\frac{E_g}{2}\right)^2}. \tag{A.15}$$

For each $A(\mathbf{k}, \mathbf{k}; E)$ plot, a measure of the broadening is also extracted. We consider a specific k_x value, k_x^B, and compute the quantity $2B$ as the difference between the two energies at which the function $A(k_x^B, k_x^B; E)$ decreases to half of its maximum value.

The input and output parameters of the bandgap and broadening extraction are collected in Table A.1 for each set of sample: L, P, and LP refer to the fitting curves (A.13), (A.14) and (A.15), respectively; $v_F = (3/2)a_{CC}|\gamma|/\hbar$ is the graphene Fermi velocity, while m_0 is the electron rest mass. The result of the fitting for negative E is shown in Fig. A.4, superimposed to the original $A(\mathbf{k}, \mathbf{k}; E)$ plot.

set	SL	n_c	N_w	E_1 (eV)	E_2 (eV)	fit.	$E_g/2$ (eV)	v/v_F	$m/m0$	k_x^B (Å^{-1})	$2B$ (eV)
(a)	13	0.75	2	0.05	0.6	LP	0.285		0.035	0.101	0.14
(b)	13	0.75	3	0.2	0.55	L	0.507	0.537		0.101	0.15
(c)	13	0.75	4	0.25	0.6	LP	0.555		0.094	0.101	0.28
(d)	13	1	2	0.1	0.6	LP	0.365		0.046	0.101	0.13
(e)	13	1	3	0.3	0.6	L	0.594	0.491		0.101	0.18
(f)	13	1	4	0.25	0.7	LP	0.633		0.110	0	0.12
(g)	10	0.75	2	0.1	1	LP	0.396		0.048	0.098	0.18
(h)	10	0.75	3	0.4	0.7	L	0.736	0.465		0.098	0.18
(i)	10	0.75	4	0.4	0.8	P	0.876		0.236	0	0.23
(j)	10	1	2	0.3	0.7	LP	0.650		0.087	0.098	0.22
(k)	10	1	3	0.35	0.7	L	0.868	0.393		0.098	0.19
(l)	10	1	4	0.35	0.8	LP	0.979		0.192	0	0.23

Table A.1:

Parameters of the $A(\mathbf{k}, \mathbf{k})$ fitting and broadening extraction.

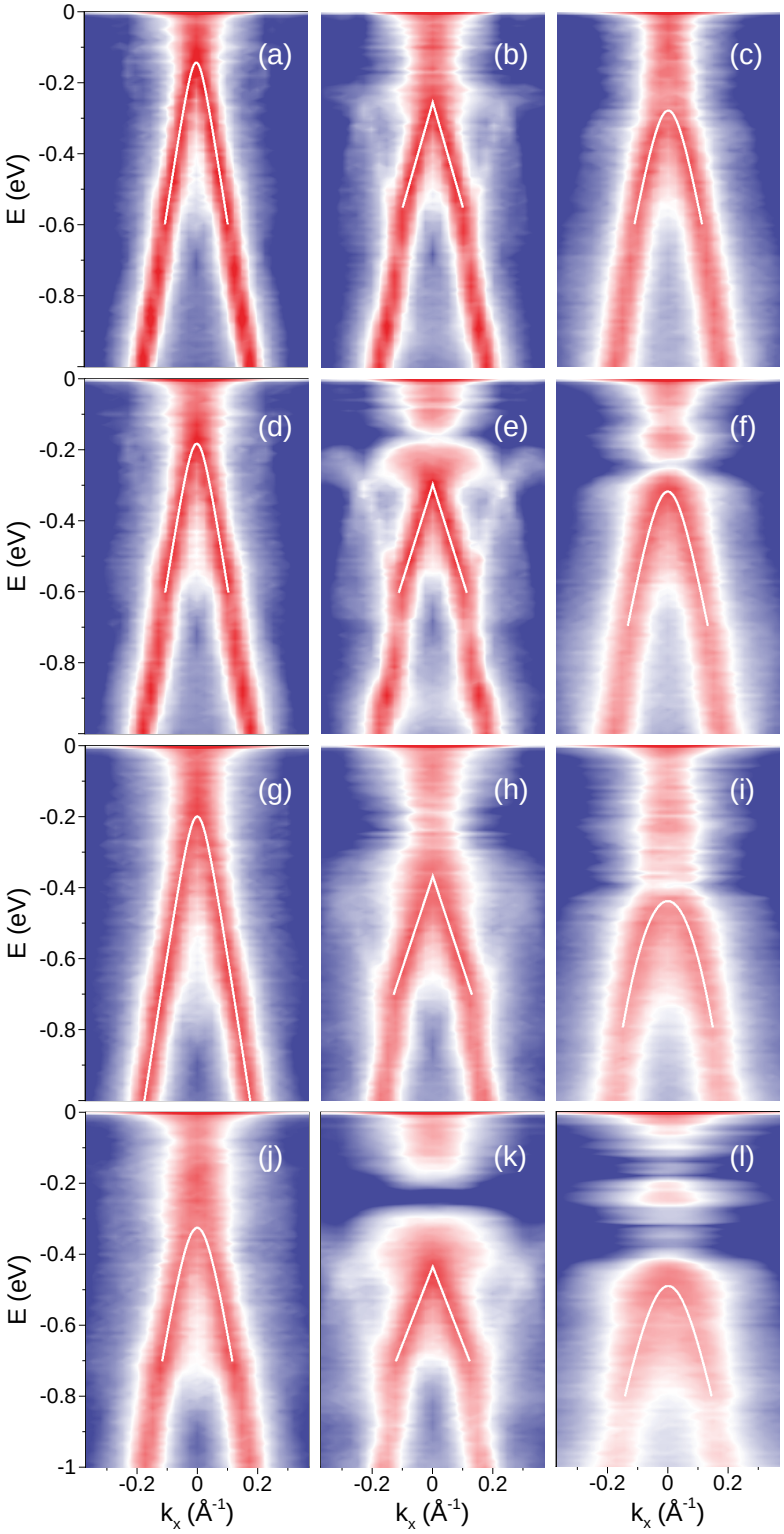

Figure A.4: Plot of $A(\mathbf{k}, \mathbf{k}; E)$ and fitting curve, for all the set of samples studied in this work. The color scale, which is not shown, is the same as in Figs. 4.4 and 4.5. (i) and (l) coincide with the plots in Figs. 4.4, (j) and (k) with the ones in Figs. 4.5.

Appendix *B*

Local density of states in k-space

In Chap. 4, it has been demonstrated that the calculation of the density of states in energy and momentum is a powerful tool to investigate the electronic properties of disordered systems, going beyond the usual bandstructure calculation and providing a quantity that can be directly compared with the ARPES measurement. Although the results of similar calculations were already presented in [45], a detailed introduction to this concept is missing in the literature. This has been the motivation for writing these notes.

The discussion starts for simplicity from the case in which the particle position can be described by a continuous vector $\mathbf{r}$ (Sect. B.1). Then, the concepts are generalized to a TB description (Sect. B.2). The analytical calculation of $A(\mathbf{k}, \mathbf{k}; E)$ for pristine graphene is presented as an exercise at the end (Sect. B.3).

B.1 Continuous case

Consider a particle described by the Hamiltonian H. The retarded Green's function in real space (r-space) at the energy E is defined as

$$G^r(\mathbf{r}_1, \mathbf{r}_2; E) = \langle \mathbf{r}_1 | \frac{1}{(E + \mathrm{i}\eta)I - H} | \mathbf{r}_2 \rangle \,, \tag{B.1}$$

with η an infinitesimal positive quantity, which is necessary if H is Hermitian. The advanced Green's function is instead given by $G^a = G^{r\dagger}$, so in r-space we have $G^a(\mathbf{r}_1, \mathbf{r}_2; E) = [G^r(\mathbf{r}_2, \mathbf{r}_1; E)]^*$.

The spectral function is defined as $A = \mathrm{i}(G^r - G^a)$ and therefore is a Hermitian quantity. The local density of states in r-space is given by the diagonal elements

of the spectral function,

$$\mathrm{LDOS}_r(\mathbf{r};E) = \frac{1}{2\pi}A(\mathbf{r},\mathbf{r};E) = -\frac{1}{\pi}\Im[G^r(\mathbf{r},\mathbf{r};E)]\,, \tag{B.2}$$

while the density of states by its trace,

$$\mathrm{DOS}(E) = \frac{1}{2\pi}\mathrm{Tr}\,[A(E)] = \frac{1}{2\pi}\int d\mathbf{r}A(\mathbf{r},\mathbf{r};E) = -\frac{1}{\pi}\int d\mathbf{r}\Im[G^r(\mathbf{r},\mathbf{r};E)]\,. \tag{B.3}$$

One could also work in k-space, where the retarded Green's function is defined as

$$G^r(\mathbf{k}_1,\mathbf{k}_2;E) = \langle\mathbf{k}_1|\frac{1}{(E+\mathrm{i}\eta)I-H}|\mathbf{k}_2\rangle\,, \tag{B.4}$$

with $\langle\mathbf{r}|\mathbf{k}\rangle = e^{\mathrm{i}\mathbf{k}\cdot\mathbf{r}}/\sqrt{V}$ and assuming a finite volume V with periodic boundary conditions. The local density of states in k-space is then given by

$$\mathrm{LDOS}_k(\mathbf{k};E) = \frac{1}{2\pi}A(\mathbf{k},\mathbf{k};E) = -\frac{1}{\pi}\Im[G^r(\mathbf{k},\mathbf{k};E)]\,. \tag{B.5}$$

In turn, the diagonal element of the spectral function (and similarly of G^r) in k-space can be expanded as

$$\begin{aligned} A(\mathbf{k},\mathbf{k};E) &= \int d\mathbf{r}_1\int d\mathbf{r}_2\langle\mathbf{k}|\mathbf{r}_1\rangle A(\mathbf{r}_1,\mathbf{r}_2;E)\langle\mathbf{r}_2|\mathbf{k}\rangle \\ &= \frac{1}{V}\int d\mathbf{r}_1\int d\mathbf{r}_2 e^{-\mathrm{i}\mathbf{k}\cdot(\mathbf{r}_1-\mathbf{r}_2)}A(\mathbf{r}_1,\mathbf{r}_2;E)\,. \end{aligned} \tag{B.6}$$

Since $A(\mathbf{r}_1,\mathbf{r}_2;E)$ is Hermitian, $A(\mathbf{k},\mathbf{k};E)$ is real:

$$\begin{aligned} [A(\mathbf{k},\mathbf{k};E)]^* &= \frac{1}{V}\int d\mathbf{r}_1\int d\mathbf{r}_2 e^{\mathrm{i}\mathbf{k}\cdot(\mathbf{r}_1-\mathbf{r}_2)}A(\mathbf{r}_2,\mathbf{r}_1;E) \\ &= \frac{1}{V}\int d\mathbf{r}_2\int d\mathbf{r}_1 e^{\mathrm{i}\mathbf{k}\cdot(\mathbf{r}_2-\mathbf{r}_1)}A(\mathbf{r}_1,\mathbf{r}_2;E) \\ &= A(\mathbf{k},\mathbf{k};E)\,. \end{aligned} \tag{B.7}$$

By defining $\mathbf{r} = \mathbf{r}_1 - \mathbf{r}_2$, (B.6) can be rewritten as

$$A(\mathbf{k},\mathbf{k};E) = \frac{1}{V}\int d\mathbf{r}_1\int d\mathbf{r}e^{-\mathrm{i}\mathbf{k}\cdot\mathbf{r}}A(\mathbf{r}_1,\mathbf{r}_1-\mathbf{r};E)\,. \tag{B.8}$$

Thus, the diagonal element of the spectral function in k-space can be thought of as the Fourier transform of $A(\mathbf{r}_1,\mathbf{r}_2;E)$ with respect to the relative variable $\mathbf{r}_1-\mathbf{r}_2$, averaged over $\mathbf{r}_1$. We note that, if H is symmetric under time reversal, then $G^r = (G^r)^T$ and thus $A(\mathbf{r}_1,\mathbf{r}_1-\mathbf{r};E) = -2\Im[G^r(\mathbf{r}_1,\mathbf{r}_1-\mathbf{r};E)]$, which means that $A(\mathbf{k},\mathbf{k};E)$ is even in $\mathbf{k}$:

$$\begin{aligned} A(-\mathbf{k},-\mathbf{k};E) &= \frac{1}{V}\int d\mathbf{r}_1\int d\mathbf{r}e^{\mathrm{i}\mathbf{k}\cdot\mathbf{r}}A(\mathbf{r}_1,\mathbf{r}_1-\mathbf{r};E) \\ &= \left[\frac{1}{V}\int d\mathbf{r}_1\int d\mathbf{r}e^{-\mathrm{i}\mathbf{k}\cdot\mathbf{r}}A(\mathbf{r}_1,\mathbf{r}_1-\mathbf{r};E)\right]^* \\ &= [A(\mathbf{k},\mathbf{k};E)]^* \\ &= A(\mathbf{k},\mathbf{k};E)\,. \end{aligned} \tag{B.9}$$

Since the first identity in (B.3) is valid in every representation, we have

$$\mathrm{DOS}(E) = \frac{1}{2\pi}\sum_{\mathbf{k}} A(\mathbf{k},\mathbf{k};E) = -\frac{1}{\pi}\sum_{\mathbf{k}} \Im[G^r(\mathbf{k},\mathbf{k};E)]\,, \tag{B.10}$$

which can also be proved from (B.8) using the property $V^{-1}\sum_{\mathbf{k}} e^{-\mathrm{i}\mathbf{k}\cdot\mathbf{r}} = \delta(\mathbf{r})$.

Consider now the case of a Hermitian H, that is with no self-energy in it. Using the resolution of the identity in terms of the orthonormal eigenstates $\{|\psi_\alpha\rangle\}$ of H (ϵ_α being the real eigenvalue corresponding to $|\psi_\alpha\rangle$), we can express the retarded Green's function in r-space as

$$G^r(\mathbf{r}_1,\mathbf{r}_2;E) = \sum_\alpha \frac{1}{E+\mathrm{i}\eta-\epsilon_\alpha}\psi_\alpha(\mathbf{r}_1)\psi^*_\alpha(\mathbf{r}_2)\,, \tag{B.11}$$

with $\psi_\alpha(\mathbf{r}) = \langle\mathbf{r}|\psi_\alpha\rangle$ the generic eigenfunction in r-space. Therefore the spectral function in r-space takes the form

$$A(\mathbf{r}_1,\mathbf{r}_2;E) = \sum_\alpha \frac{2\eta}{(E-\epsilon_\alpha)^2+\eta^2}\psi_\alpha(\mathbf{r}_1)\psi^*_\alpha(\mathbf{r}_2) \overset{\eta\to 0}{\longrightarrow} 2\pi\sum_\alpha \delta(E-\epsilon_\alpha)\psi_\alpha(\mathbf{r}_1)\psi^*_\alpha(\mathbf{r}_2) \tag{B.12}$$

and (B.2), (B.3), and (B.8) become, respectively,

$$\mathrm{LDOS}_r(\mathbf{r};E) = \sum_\alpha \delta(E-\epsilon_\alpha)|\psi_\alpha(\mathbf{r})|^2\,, \tag{B.13}$$

$$\mathrm{DOS}(E) = \sum_\alpha \delta(E-\epsilon_\alpha)\,, \tag{B.14}$$

$$A(\mathbf{k},\mathbf{k};E) = 2\pi\sum_\alpha \delta(E-\epsilon_\alpha)\frac{1}{V}\int d\mathbf{r}_1 F_\alpha(\mathbf{k},\mathbf{r}_1)\,, \tag{B.15}$$

where we have defined

$$F_\alpha(\mathbf{k};\mathbf{r}_1) = \int d\mathbf{r} e^{-\mathrm{i}\mathbf{k}\cdot\mathbf{r}}\psi_\alpha(\mathbf{r}_1)\psi^*_\alpha(\mathbf{r}_1-\mathbf{r})\,. \tag{B.16}$$

In the translationally invariant case, we have

$$\psi_\alpha(\mathbf{r}) = \frac{1}{\sqrt{V}}e^{\mathrm{i}\mathbf{k}_\alpha\cdot\mathbf{r}}\,, \tag{B.17}$$

thus F_α is independent on $\mathbf{r}_1$,

$$F_\alpha(\mathbf{k};\mathbf{r}_1) = \delta(\mathbf{k}-\mathbf{k}_\alpha)\,, \tag{B.18}$$

and

$$A(\mathbf{k},\mathbf{k};E) = 2\pi\sum_\alpha \delta(E-\epsilon_\alpha)\delta(\mathbf{k}-\mathbf{k}_\alpha)\,. \tag{B.19}$$

It is clear from (B.15) that the local density of states in k-space is a meaningful concept if the particle under study moves in a large sample that can be divided

in smaller regions which are more or less similar to each other, so that by shifting the origin the same structure is seen, even if the wavefunctions are not plane waves. Indeed, if F_α is only slightly dependent on $\mathbf{r}_1$, there is a chance that the average over $\mathbf{r}_1$ will not destroy an eventual dependence on $\mathbf{k}$. Otherwise, if the dependence on $\mathbf{k}$ is destroyed, the spectral function will be simply proportional to the density of states, as stated by (B.10).

If H is not Hermitian, one must consider the bi-orthonormal basis formed of the eigenvectors of H and $H^\dagger$. The main difference is the broadening of the peaks caused by the eigenvalues of H being no more real numbers.

B.2 Lattice case

Consider now the case of motion in a discretized r-space, that is in a Bravais lattice, described by the primitive vectors $\mathbf{a}_i$ ($i = 1, \ldots, d$, being d the number of dimensions). The position of each node with respect to a specific node, taken as the origin, can be represented by a lattice vector $\mathbf{l} = \sum_i n_i \mathbf{a}_i$, with $n_i = 1, \ldots, N_i$, where we have assumed a finite number of cells $N_c = \prod_i N_i$. This is the case, for example, of an orthogonal tight-binding representation: a certain number of atomic orbitals $|\mathbf{l}, q\rangle$, with $q = 1, \ldots, Q$, is associated to each lattice site (or unit cell). In what follows, we assume that the number of orbitals Q is the same in each unit cell.

The retarded Green's function in r-space now reads

$$G^r(\mathbf{l}_1, q_1; \mathbf{l}_2, q_2; E) = \langle \mathbf{l}_1, q_1 | \frac{1}{(E + \mathrm{i}\eta)I - H} | \mathbf{l}_2, q_2 \rangle \,. \tag{B.20}$$

The local density of states in r-space (number of states per unit energy in each unit cell) is

$$\mathrm{LDOS}_r(\mathbf{l}; E) = \frac{1}{2\pi} \sum_q A(\mathbf{l}, q; \mathbf{l}, q; E) = -\frac{1}{\pi} \sum_q \Im[G^r(\mathbf{l}, q; \mathbf{l}, q; E)] \,, \tag{B.21}$$

and the density of states,

$$\mathrm{DOS}(E) = \frac{1}{2\pi} \mathrm{Tr}\,[A(E)] = \frac{1}{2\pi} \sum_{\mathbf{l},q} A(\mathbf{l}, q; \mathbf{l}, q; E) = -\frac{1}{\pi} \sum_{\mathbf{l},q} \Im[G^r(\mathbf{l}, q; \mathbf{l}, q; E)] \,. \tag{B.22}$$

The k-space representation is obtained by using as basis the set $|\mathbf{k}, q\rangle$ defined by $\langle \mathbf{l}, q_1 | \mathbf{k}, q_2 \rangle = \delta_{q_1,q_2} e^{\mathrm{i}\mathbf{k}\cdot\mathbf{l}} / \sqrt{N_c}$. If $\mathbf{b}_i$ are the primitive vectors of the reciprocal lattice, $\mathbf{a}_i \cdot \mathbf{b}_j = 2\pi\delta_{i,j}$, we have for a generic reciprocal lattice vector $\mathbf{g} = \sum_i m_i \mathbf{b}_i$

$$\exp[\mathrm{i}(\mathbf{k} + \mathbf{g}) \cdot \mathbf{l}] = \exp(\mathrm{i}\mathbf{k} \cdot \mathbf{l}) \exp(\mathrm{i}2\pi \sum_i m_i n_i) = \exp(\mathrm{i}\mathbf{k} \cdot \mathbf{l}) \,, \tag{B.23}$$

so the $\mathbf{k}$ vectors to be considered are only those lying within the first Brillouin zone. The local density of states in k-space is given by

$$\mathrm{LDOS}_k(\mathbf{k};E) = \frac{1}{2\pi}\sum_q A(\mathbf{k},q;\mathbf{k},q;E) = -\frac{1}{\pi}\sum_q \Im[G^r(\mathbf{k},q;\mathbf{k},q;E)]\,. \quad \text{(B.24)}$$

with

$$\begin{aligned} A(\mathbf{k},q;\mathbf{k},q;E) &= \sum_{\mathbf{l}_1,q_1}\sum_{\mathbf{l}_2,q_2}\langle\mathbf{k},q|\mathbf{l}_1,q_1\rangle A(\mathbf{l}_1,q_1;\mathbf{l}_2,q_2;E)\langle\mathbf{l}_2,q_2|\mathbf{k},q\rangle \\ &= \frac{1}{N_c}\sum_{\mathbf{l}_1}\sum_{\mathbf{l}_2} e^{-\mathrm{i}\mathbf{k}\cdot(\mathbf{l}_1-\mathbf{l}_2)}A(\mathbf{l}_1,q;\mathbf{l}_2,q;E) \\ &= \frac{1}{N_c}\sum_{\mathbf{l}_1}\sum_{\mathbf{l}} e^{-\mathrm{i}\mathbf{k}\cdot\mathbf{l}}A(\mathbf{l}_1,q;\mathbf{l}_1-\mathbf{l},q;E)\,, \end{aligned} \quad \text{(B.25)}$$

where we recognize a discrete Fourier transform with respect to the relative variable $\mathbf{l} = \mathbf{l}_1 - \mathbf{l}_2$.

B.3 Example: pure graphene

Here we calculate the local density of states in k-space for pure graphene. The graphene sheet is represented in Fig. B.1. The primitive vectors of the direct lattice are $\mathbf{a}_1 = a(1,0)$ and $\mathbf{a}_2 = a(1/2,\sqrt{3}/2)$; the corresponding vectors of the reciprocal lattice are instead $\mathbf{b}_1 = 4\pi/(\sqrt{3}a)(\sqrt{3}/2,-1/2)$ and $\mathbf{b}_2 = 4\pi/(\sqrt{3}a)(0,1)$. The unit cell is made of two carbon atoms A and B. We consider the simple tight-binding model with one orbital for each carbon atom (thus $q = 1,2$) and hopping parameter γ between first nearest neighbor atoms. For simplicity, we consider the case of a finite sample, composed of N_1 and N_2 unit cells along the directions of $\mathbf{a}_1$ and $\mathbf{a}_2$, respectively, with periodic boundary conditions. The result for an infinite sheet is obtained in the limit where $N_1, N_2 \to \infty$.

Let H be the tight-binding Hamiltonian matrix of the system (without η in it). We start from the expression for the spectral function in r-space expanded in terms of the eigenvectors of H (ϵ_α being the corresponding eigenvalues):

$$A(\mathbf{l}_1,q;\mathbf{l}_2,q;E) = \sum_\alpha \frac{2\eta}{(E-\epsilon_\alpha)^2+\eta^2}\psi_\alpha(\mathbf{l}_1,q)\psi^*_\alpha(\mathbf{l}_2,q)\,. \quad \text{(B.26)}$$

For brevity, we introduce the notation

$$\psi_\alpha(\mathbf{l}) = \begin{pmatrix} \psi_\alpha(\mathbf{l},1) \\ \psi_\alpha(\mathbf{l},2) \end{pmatrix}, \quad \text{(B.27)}$$

so that (B.26) corresponds to the diagonal elements of the 2×2 matrix

$$A(\mathbf{l}_1,\mathbf{l}_2;E) = \sum_\alpha \frac{2\eta}{(E-\epsilon_\alpha)^2+\eta^2}\psi_\alpha(\mathbf{l}_1)\psi^\dagger_\alpha(\mathbf{l}_2)\,. \quad \text{(B.28)}$$

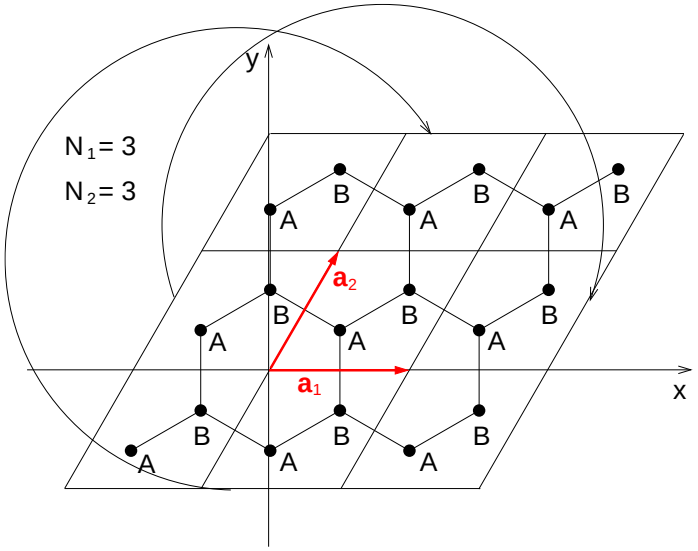

Figure B.1: Sample made of $N_1 \times N_2$ graphene unit cells, with periodic boundary conditions on both $\mathbf{a}_1$ and $\mathbf{a}_2$ directions.

By using the *ansatz* $\psi(\mathbf{l}) \propto e^{\mathrm{i}\mathbf{k}\cdot\mathbf{l}} v$, it is straightforward to obtain the eigenvalue equation

$$\begin{pmatrix} \epsilon & -f(\mathbf{k}) \\ -f(\mathbf{k})^* & \epsilon \end{pmatrix} v = 0\,, \tag{B.29}$$

with $f(\mathbf{k}) = \gamma\left(1 + e^{-\mathrm{i}k_x a} + e^{-\mathrm{i}k_x a/2} e^{-\mathrm{i}k_y \sqrt{3}a/2}\right)$ and $\mathbf{k} = (m_1/N_1)\mathbf{b}_1 + (m_2/N_2)\mathbf{b}_2$, where $m_1, m_2 \in \mathbb{N}$. Since (B.23) holds, only a number $N_c = N_1 N_2$ of $\mathbf{k}$ vectors gives rise to independent eigenvectors. From (B.29), we get the eigenvalues

$$\epsilon_\pm(\mathbf{k}) = \pm|f(\mathbf{k})| = \pm|\gamma| \sqrt{1 + 4\cos\left(k_x \frac{a}{2}\right)\cos\left(k_y \frac{\sqrt{3}a}{2}\right) + 4\cos^2\left(k_x \frac{a}{2}\right)} \tag{B.30}$$

and normalized eigenvectors

$$\psi_\pm(\mathbf{k}, \mathbf{l}) = \frac{1}{\sqrt{N_c}} e^{\mathrm{i}\mathbf{k}\cdot\mathbf{l}} v_\pm(\mathbf{k}) = \frac{1}{\sqrt{N_c}} e^{\mathrm{i}\mathbf{k}\cdot\mathbf{l}} \frac{1}{\sqrt{2}} \begin{pmatrix} 1 \\ \pm e^{-\mathrm{i}\theta(\mathbf{k})} \end{pmatrix}, \tag{B.31}$$

with $e^{\mathrm{i}\theta(\mathbf{k})} = f(\mathbf{k})/|f(\mathbf{k})|$. Therefore, by setting $\alpha \equiv (\mathbf{k}', b)$ with $b \in \{+, -\}$, (B.28) becomes

$$A(\mathbf{l}_1, \mathbf{l}_2; E) = \frac{1}{2N_c} \sum_{\mathbf{k}'} e^{\mathrm{i}\mathbf{k}'\cdot(\mathbf{l}_1 - \mathbf{l}_2)} \left\{ \frac{2\eta}{[E - \epsilon_+(\mathbf{k}')]^2 + \eta^2} \begin{pmatrix} 1 & e^{\mathrm{i}\theta(\mathbf{k}')} \\ e^{-\mathrm{i}\theta(\mathbf{k}')} & 1 \end{pmatrix} + \right.$$
$$\left. + \frac{2\eta}{[E - \epsilon_-(\mathbf{k}')]^2 + \eta^2} \begin{pmatrix} 1 & -e^{\mathrm{i}\theta(\mathbf{k}')} \\ -e^{-\mathrm{i}\theta(\mathbf{k}')} & 1 \end{pmatrix} \right\}. \tag{B.32}$$

By extracting the diagonal entries of this matrix, we get

$$A(\mathbf{l}_1, q; \mathbf{l}_2, q; E) = \frac{1}{2N_c} \sum_{\mathbf{k}'} e^{\mathrm{i}\mathbf{k}'\cdot(\mathbf{l}_1-\mathbf{l}_2)} \left\{ \frac{2\eta}{[E-\epsilon_+(\mathbf{k}')]^2+\eta^2} + \frac{2\eta}{[E-\epsilon_-(\mathbf{k}')]^2+\eta^2} \right\}. \tag{B.33}$$

Finally, the local density of states in k-space is easily calculated as

$$\begin{aligned}
\mathrm{LDOS}_k(\mathbf{k}; E) &= \frac{1}{2\pi} \sum_q A(\mathbf{k}, q; \mathbf{k}, q; E) \\
&= \frac{1}{2\pi} \sum_q \frac{1}{N_c} \sum_{\mathbf{l}_1} \sum_{\mathbf{l}} e^{-\mathrm{i}\mathbf{k}\cdot\mathbf{l}} A(\mathbf{l}_1, q; \mathbf{l}_1 - \mathbf{l}, q; E) \\
&= \frac{1}{2\pi} \sum_{\mathbf{k}'} \left\{ \frac{2\eta}{[E-\epsilon_+(\mathbf{k}')]^2+\eta^2} + \frac{2\eta}{[E-\epsilon_-(\mathbf{k}')]^2+\eta^2} \right\} \times \\
&\quad \times \left[\frac{1}{N_c} \sum_{\mathbf{l}} e^{\mathrm{i}(\mathbf{k}'-\mathbf{k})\cdot\mathbf{l}} \left(\frac{1}{N_c} \sum_{\mathbf{l}_1} 1 \right) \right] \\
&= \frac{1}{2\pi} \left\{ \frac{2\eta}{[E-\epsilon_+(\mathbf{k})]^2+\eta^2} + \frac{2\eta}{[E-\epsilon_-(\mathbf{k})]^2+\eta^2} \right\},
\end{aligned} \tag{B.34}$$

where we have used the property $(1/N_c)\sum_{\mathbf{l}} e^{\mathrm{i}(\mathbf{k}'-\mathbf{k})\cdot\mathbf{l}} = \delta(\mathbf{k}'-\mathbf{k})$.

Appendix *C*

Novel numerical algorithms

In this chapter, two novel numerical algorithms for calculating Green's functions are presented. Both algorithms exploit the block-tridiagonal property of the Hamiltonian, i.e. the fact that the structure under study can be thought as being made by a linear chain of slabs, each slabs being coupled through the Hamiltonian only to the previous slab and the next one.

The first algorithm (Sect. C.1) is used to calculate the retarded Green's function for a closed structure made of a linear chain of slabs with a periodic closure at the two ends. This is for example the situation considered in the "ARPES" simulation of Sect. 4.3 and App. B. The second algorithm (Sect. C.2) is instead intended to be used in transport simulations to compute the lead self-energies: it is an improved version of the algorithm in [24] for the case in which the lead unit cell is composed of several slabs. It can be applied, for example, to a lead made of an armchair GNR, since, if a 1NN model is used, the unit cell can be viewed as being formed of four slabs, each one corresponding to one row of carbon atoms.

C.1 Recursive Green's function algorithm for periodic structures

C.1.1 General formulation

We consider a particle described by a Hamiltonian matrix H having the form

$$H = \begin{pmatrix} H_{1,1} & H_{1,2} & & & H_{1,N} \\ H_{2,1} & H_{2,2} & H_{2,3} & & \\ & H_{3,2} & \ddots & \ddots & \\ & & \ddots & \ddots & H_{N-1,N} \\ H_{N,1} & & & H_{N,N-1} & H_{N,N} \end{pmatrix} \tag{C.1}$$

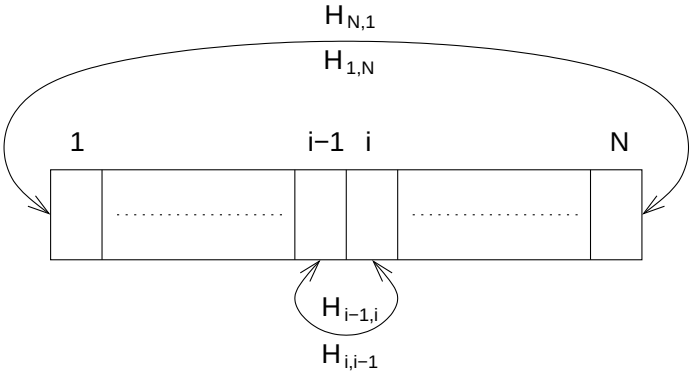

Figure C.1: Structure corresponding to H.

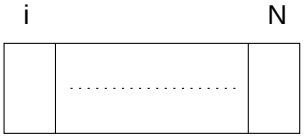

Figure C.2: Structure corresponding to $H^{\mathcal{R},(i)}$.

and thus representing a layered structure with periodic boundary conditions (Fig. C.1). We suppose here that $N \geq 2$. The retarded Green's function G^r at the energy E is defined as $AG^r = I$, where $A = (E + \mathrm{i}\eta)I - H$ being η an infinitesimal positive quantity (the quantity A should not be confused with the spectral function, for which the same symbol has been used in other chapters of this thesis). Here we present an algorithm for calculating selected elements of G^r extending the one in [23] for the case of $H_{1,N}$ and $H_{N,1} \neq 0$.

Let $g^{r\mathcal{R},(i)}$ be the retarded Green's function corresponding to the Hamiltonian

$$H^{\mathcal{R},(i)} = \begin{pmatrix} H_{i,i} & H_{i,i+1} & \\ H_{i+1,i} & \ddots & \ddots \\ & \ddots & H_{N,N} \end{pmatrix}, \tag{C.2}$$

which describes the structure composed of only the nodes from i to N without the periodic closure (Fig. C.2). $H^{\mathcal{R},(i)}$ can be written as the sum of an unperturbed Hamiltonian $H^{0\mathcal{R},(i)}$,

$$H^{0\mathcal{R},(i)} = \begin{pmatrix} H_{i,i} & & & \\ & H_{i+1,i+1} & H_{i+1,i+2} & \\ & H_{i+2,i+1} & \ddots & \ddots \\ & & \ddots & \ddots \end{pmatrix}, \tag{C.3}$$

and a perturbation Hamiltonian $H^{1\mathcal{R},(i)}$,

$$H^{1\mathcal{R},(i)} = \begin{pmatrix} & H_{i,i+1} & \\ H_{i+1,i} & & \\ & & \end{pmatrix} . \tag{C.4}$$

We note that the retarded Green's function corresponding to $H^{0\mathcal{R},(i)}$ is simply given by

$$\begin{pmatrix} A_{i,i}^{-1} & \\ & g^{r\mathcal{R},(i+1)} \end{pmatrix} , \tag{C.5}$$

so $g^{r\mathcal{R},(i)}$ can be related to $g^{r\mathcal{R},(i+1)}$ by means of the Dyson equations

$$g^{r\mathcal{R},(i)} = \begin{pmatrix} A_{i,i}^{-1} & \\ & g^{r\mathcal{R},(i+1)} \end{pmatrix} + \begin{pmatrix} A_{i,i}^{-1} & \\ & g^{r\mathcal{R},(i+1)} \end{pmatrix} H^{1\mathcal{R},(i)} g^{r\mathcal{R},(i)} \tag{C.6}$$

and

$$g^{r\mathcal{R},(i)} = \begin{pmatrix} A_{i,i}^{-1} & \\ & g^{r\mathcal{R},(i+1)} \end{pmatrix} + g^{r\mathcal{R},(i)} H^{1\mathcal{R},(i)} \begin{pmatrix} A_{i,i}^{-1} & \\ & g^{r\mathcal{R},(i+1)} \end{pmatrix} . \tag{C.7}$$

From (C.6–C.7), we can derive the following algorithm for calculating certain elements of $g^{r\mathcal{R},(i)}$ that will be needed later for the calculation of G^r:

- initialize
$$g_{N,N}^{r\mathcal{R},(N)} = (A_{N,N})^{-1} ; \tag{C.8}$$
- for $i = N-1, \ldots, 1$ compute
$$g_{i,i}^{r\mathcal{R},(i)} = (A_{i,i} - A_{i,i+1} g_{i+1,i+1}^{r\mathcal{R},(i+1)} A_{i+1,i})^{-1} , \tag{C.9}$$
$$g_{i,N}^{r\mathcal{R},(i)} = -g_{i,i}^{r\mathcal{R},(i)} A_{i,i+1} g_{i+1,N}^{r\mathcal{R},(i+1)} , \tag{C.10}$$
$$g_{N,i}^{r\mathcal{R},(i)} = -g_{N,i+1}^{r\mathcal{R},(i+1)} A_{i+1,i} g_{i,i}^{r\mathcal{R},(i)} , \tag{C.11}$$
$$g_{N,N}^{r\mathcal{R},(i)} = g_{N,N}^{r\mathcal{R},(i+1)} - g_{N,i+1}^{r\mathcal{R},(i+1)} A_{i+1,i} g_{i,N}^{r\mathcal{R},(i)} . \tag{C.12}$$

We now consider H as the sum of an unperturbed Hamiltonian $H^{0,(i)}$,

$$H^{0,(i)} = \begin{pmatrix} \ddots & \ddots & & & & & \\ \ddots & \ddots & H_{i-2,i-1} & & & & \\ & H_{i-1,i-2} & H_{i-1,i-1} & & & & \\ & & & H_{i,i} & H_{i,i+1} & & \\ & & & H_{i+1,i} & \ddots & \ddots & \\ & & & & \ddots & \ddots & \end{pmatrix} , \tag{C.13}$$

and a perturbation Hamiltonian $H^{1,(i)}$,

$$H^{1,(i)} = \begin{pmatrix} & & & & H_{1,N} \\ & & & H_{i-1,i} & \\ & & H_{i,i-1} & & \\ & & & & \\ H_{N,1} & & & & \end{pmatrix}, \tag{C.14}$$

The retarded Green's function corresponding to $H^{0,(i)}$ is given by

$$\begin{pmatrix} g^{r\mathcal{L},(i-1)} & \\ & g^{r\mathcal{R},(i)} \end{pmatrix}, \tag{C.15}$$

with an obvious definition of $g^{r\mathcal{L},(i-1)}$, so we have the Dyson equations

$$G^r = \begin{pmatrix} g^{r\mathcal{L},(i-1)} & \\ & g^{r\mathcal{R},(i)} \end{pmatrix} + \begin{pmatrix} g^{r\mathcal{L},(i-1)} & \\ & g^{r\mathcal{R},(i)} \end{pmatrix} H^{1,(i)} G^r \tag{C.16}$$

and

$$G^r = \begin{pmatrix} g^{r\mathcal{L},(i-1)} & \\ & g^{r\mathcal{R},(i)} \end{pmatrix} + G^r H^{1,(i)} \begin{pmatrix} g^{r\mathcal{L},(i-1)} & \\ & g^{r\mathcal{R},(i)} \end{pmatrix}. \tag{C.17}$$

From (C.16–C.17), we can derive the following algorithm for calculating the diagonal elements of G^r given the previously calculated quantities:

- initialize

$$\begin{aligned} G^r_{1,1} = &\left[I + g^{r\mathcal{R},(1)}_{1,N} A_{N,1} - g^{r\mathcal{R},(1)}_{1,1} \left(I + A_{1,N} g^{r\mathcal{R},(1)}_{N,1} \right)^{-1} A_{1,N} g^{r\mathcal{R},(1)}_{N,N} A_{N,1} \right]^{-1} \times \\ &\times \left[g^{r\mathcal{R},(1)}_{1,1} - g^{r\mathcal{R},(1)}_{1,1} \left(I + A_{1,N} g^{r\mathcal{R},(1)}_{N,1} \right)^{-1} A_{1,N} g^{r\mathcal{R},(1)}_{N,1} \right]; \end{aligned} \tag{C.18}$$

- for $i = 2, \ldots, N$ compute

$$G^r_{1,i} = -G^r_{1,i-1} A_{i-1,i} g^{r\mathcal{R},(i)}_{i,i} - G^r_{1,1} A_{1,N} g^{r\mathcal{R},(i)}_{N,i}, \tag{C.19}$$

$$G^r_{i,1} = -g^{r\mathcal{R},(i)}_{i,i} A_{i,i-1} G^r_{i-1,1} - g^{r\mathcal{R},(i)}_{i,N} A_{N,1} G^r_{1,1}; \tag{C.20}$$

- for $i = 2, \ldots, N$
  - if $i > 2$ then compute

$$G^r_{i-1,i} = -G^r_{i-1,i-1} A_{i-1,i} g^{r\mathcal{R},(i)}_{i,i} - G^r_{i-1,1} A_{1,N} g^{r\mathcal{R},(i)}_{N,i}, \tag{C.21}$$

– compute

$$G^r_{i,i} = g^{r\mathcal{R},(i)}_{i,i} - g^{r\mathcal{R},(i)}_{i,i} A_{i,i-1} G^r_{i-1,i} - g^{r\mathcal{R},(i)}_{i,N} A_{N,1} G^r_{1,i} \,. \tag{C.22}$$

Note that we do not need to store $g^{r\mathcal{R},(i)}_{N,N}$ for $i > 1$.

In addition, if we are interested in calculating the row of index j in the upper triangular part of G^r, we can use the following algorithm, also derived from (C.16–C.17) (note that we obtain again Eq. C.19 for $j = 1$ and Eq. C.21 for $i = j + 1$):

- for $i = j + 1, \ldots, N$ compute

$$G^r_{j,i} = -G^r_{j,i-1} A_{i-1,i} g^{r\mathcal{R},(i)}_{i,i} - G^r_{j,1} A_{1,N} g^{r\mathcal{R},(i)}_{N,i} \,. \tag{C.23}$$

Analogously, for calculating the column of index j in the lower triangular part of G^r, we have (note that we obtain again Eq. C.20 for $j = 1$):

- for $i = j + 1, \ldots, N$ compute

$$G^r_{i,j} = -g^{r\mathcal{R},(i)}_{i,i} A_{i,i-1} G^r_{i-1,j} - g^{r\mathcal{R},(i)}_{i,N} A_{N,1} G^r_{1,j} \,. \tag{C.24}$$

If the Hamiltonian is symmetric under time reversal, (C.11, C.20, C.24) can be replaced with $g^{r\mathcal{R},(i)}_{N,i} = (g^{r\mathcal{R},(i)}_{i,N})^T$, $G^r_{i,1} = (G^r_{1,i})^T$, $G^r_{i,j} = (G^r_{j,i})^T$, respectively. We note that the method presented here has the advantage, compared to the diagonalization of C.1, that the blocks of G^r can be calculated one after the other, thus saving memory.

C.1.2 Application to "ARPES" simulation

The algorithm presented above is used for the calculation of the spectral function in real space in the "ARPES" simulation. The structure under study is composed of $N_1 \times N_2$ graphene unit cells with periodic boundary conditions, as shown in Fig. C.3. The sample can be viewed as a linear chain of $2N_2$ slab in the $\mathbf{a}_2$ direction (or, equivalently, of $2N_1$ slab in the $\mathbf{a}_1$ direction), each slab corresponding to a row of carbon atoms. If the sample is hydrogenated, each slab contains also the hydrogen atoms that attach to carbon atoms within that slab. The structure is therefore of the type represented in Fig. C.1 and the algorithm above is directly applicable. Since the Hamiltonian model (4.1) is symmetrical under time reversal, only half of the matrix elements of G^r need to be calculated.

A further simplification arises from the fact that only the elements of the spectral function (and thus of G^r) that connect orbitals belonging to the same graphene sublattice are needed (see Eq. 4.3). From Fig. C.3, it can be seen that there is a corrispondence between the A and B sublattice and the odd and even slabs, respectively. Therefore, only the matrix elements of G^r connecting slabs

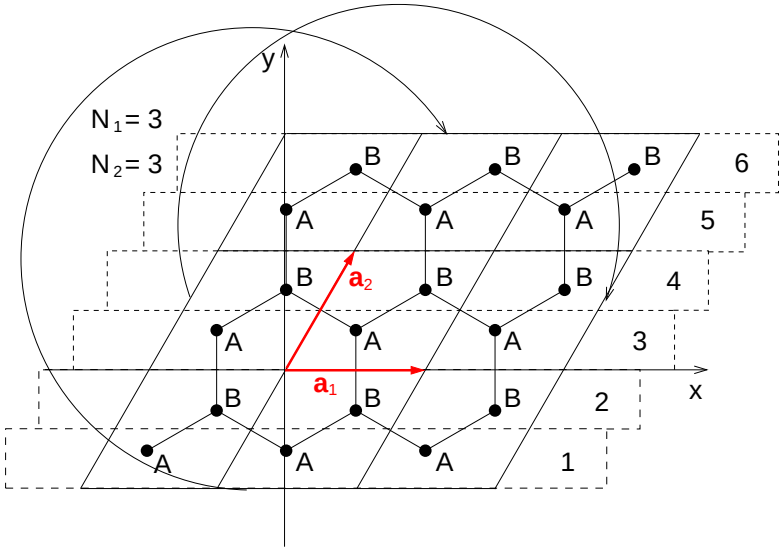

Figure C.3: Sample made of $N_1 \times N_2$ graphene unit cells, with periodic boundary conditions on both $\mathbf{a}_1$ and $\mathbf{a}_2$ directions. The boxes indicate the slab subdivision.

with the same parity need to be calculated. To exploit this property, that is to avoid the calculation of the matrix elements between slabs with different parity, the decimation method [57] is employed: an equivalent A matrix, $A^{\rm odd}$, for the odd slabs only is computed by decimating the even slabs. The same procedure is applied to the even slabs by decimating the odd ones to obtain $A^{\rm even}$.

We recall here the basic idea of the decimation method. Given the block-tridiagonal matrix $A = (E + \mathrm{i}\eta)I - H$,

$$A = \begin{pmatrix} \ddots & \ddots & & & \\ \ddots & A_{i-1,i-1} & A_{i-1,i} & & \\ & A_{i,i-1} & A_{i,i} & A_{i,i+1} & \\ & & A_{i+1,i} & A_{i+1,i+1} & \ddots \\ & & & \ddots & \ddots \end{pmatrix}, \tag{C.25}$$

the purpose is to construct a new block-tridiagonal matrix $\tilde{A}$ such that

$$\begin{pmatrix} \ddots & \ddots & & \\ \ddots & \tilde{A}_{i-1,i-1} & \tilde{A}_{i-1,i+1} & \\ & \tilde{A}_{i+1,i-1} & \tilde{A}_{i+1,i+1} & \ddots \\ & & \ddots & \ddots \end{pmatrix} \begin{pmatrix} \ddots & \ddots & \ddots & \ddots \\ \ddots & G^r_{i-1,i-1} & G^r_{i-1,i+1} & \ddots \\ \ddots & G^r_{i+1,i-1} & G^r_{i+1,i+1} & \ddots \\ \ddots & \ddots & \ddots & \ddots \end{pmatrix} = I\,. \tag{C.26}$$

The problem consists in eliminating the node i, while leaving unchanged the solution for all the remaining nodes by a proper renormalization of the matrix blocks of H or equivalently of A. This is accomplished with the equations [57]

$$\begin{aligned}
\tilde{A}_{i-1,i-1} &= A_{i-1,i-1} - A_{i-1,i}(A_{i,i})^{-1}A_{i,i-1}\,,\\
\tilde{A}_{i-1,i+1} &= -A_{i-1,i}(A_{i,i})^{-1}A_{i,i+1}\,,\\
\tilde{A}_{i+1,i-1} &= -A_{i+1,i}(A_{i,i})^{-1}A_{i,i-1}\,,\\
\tilde{A}_{i+1,i+1} &= A_{i+1,i+1} - A_{i+1,i}(A_{i,i})^{-1}A_{i,i+1}\,.
\end{aligned} \tag{C.27}$$

Note that the renormalization illustrated in (Fig. 4.1) for the case of a hydrogen atom attached to a carbon atom is a special application of these formulas.

Here, we start from an A matrix with the form (same as C.1)

$$A = \begin{pmatrix}
A_{1,1} & A_{1,2} & & & A_{1,N}\\
A_{2,1} & A_{2,2} & A_{2,3} & & \\
 & A_{3,2} & \ddots & \ddots & \\
 & & \ddots & \ddots & A_{N-1,N}\\
A_{N,1} & & & A_{N,N-1} & A_{N,N}
\end{pmatrix} \tag{C.28}$$

and apply iteratively (C.27) to decimate the even nodes, given the definitions $A_{N+1,N+1} = A_{1,1}$, $A_{N,N+1} = A_{N,1}$, $A_{N+1,N} = A_{1,N}$. The result is the matrix

$$A^{\mathrm{odd}} = \begin{pmatrix}
A^{\mathrm{odd}}_{1,1} & A^{\mathrm{odd}}_{1,2} & & & A^{\mathrm{odd}}_{1,\frac{N}{2}}\\
A^{\mathrm{odd}}_{2,1} & \ddots & \ddots & & \\
 & \ddots & \ddots & A^{\mathrm{odd}}_{\frac{N}{2}-1,\frac{N}{2}} & \\
A^{\mathrm{odd}}_{\frac{N}{2},1} & & A^{\mathrm{odd}}_{\frac{N}{2},\frac{N}{2}-1} & A^{\mathrm{odd}}_{\frac{N}{2},\frac{N}{2}} &
\end{pmatrix}. \tag{C.29}$$

The algorithm is the following:

- for $i = 1, \ldots, N/2$ initialize

$$A^{\mathrm{odd}}_{i,i} = A_{2i-1,2i-1}\,; \tag{C.30}$$

- for $i = 1, \ldots, N/2$
  - set $j = 2i$, $k = \mathrm{mod}(i, \frac{N}{2}) + 1$,
  - compute

$$\begin{aligned}
A^{\mathrm{odd}}_{i,i} &= A^{\mathrm{odd}}_{i,i} - A_{j-1,j}(A_{j,j})^{-1}A_{j,i-1}\,,\\
A^{\mathrm{odd}}_{k,k} &= A^{\mathrm{odd}}_{k,k} - A_{j+1,j}(A_{j,j})^{-1}A_{j,j+1}\,,\\
A^{\mathrm{odd}}_{i,k} &= -A_{j-1,j}(A_{j,j})^{-1}A_{j,j+1}\,,\\
A^{\mathrm{odd}}_{k,i} &= -A_{j+1,j}(A_{j,j})^{-1}A_{j,j-1}\,.
\end{aligned} \tag{C.31}$$

A similar algorithm can be derived for computing A^{even}. The recursive algorithm is then applied separately to the odd and even nodes by using A^{odd} and A^{even} as input, respectively. A value of $\eta = 10^{-3}$ eV has been used in the simulations to assure the stability of the overall algorithm.

C.2 Modified Sancho-Rubio algorithm

We consider a layered structure such as the one represented in C.4: a left lead lead is connected to a device region. The generalization to the case of a right lead is straightforward.

The self-energy due to the left lead is defined as

$$\Sigma^{r,L}_{1,1} = A_{1,0} g^r_{0,0} A_{0,1} \,, \tag{C.32}$$

where A is the matrix $(E + \mathrm{i}\eta)I - H$ and g^r is the retarded Green function for the case in which the coupling between the device and the leads is set to zero [18].

Suppose that the unit cell of the lead contains M slabs (for the case of an armchair graphene nanoribbon, $M = 4$). The matrix A of the isolated left lead has thus the structure

$$A^L = \begin{pmatrix} \ddots & \ddots & & \\ \ddots & \ddots & A_{-M,-M+1} & \\ & A_{-M+1,-M} & A^C & A_{-M,-M+1} \\ & & A_{-M+1,-M} & A^C \end{pmatrix} , \tag{C.33}$$

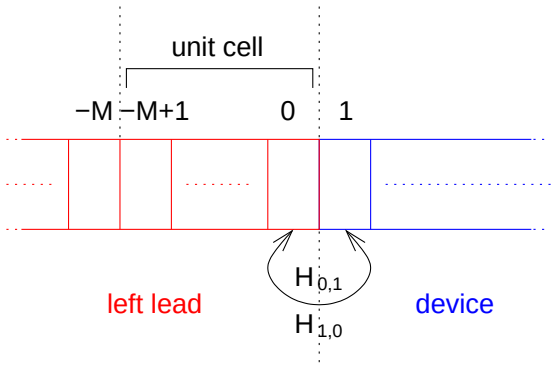

Figure C.4: Structure under consideration.

with

$$A^C = \begin{pmatrix} A_{-M+1,-M+1} & A_{-M+1,-M+2} & & \\ A_{-M+2,-M+1} & \ddots & \ddots & \\ & \ddots & A_{-1,-1} & A_{-1,0} \\ & & A_{0,-1} & A_{0,0} \end{pmatrix} . \tag{C.34}$$

Here, we propose an algorithm, based on the decimation method (see Sect. C.1.2), to reduce the size of the unit cell to only one slab, such that the usual Sancho-Rubio algorithm [24] can then be applied on matrices having a reduced size, thus saving computational time. Notice that, in the specific case considered in Chap. 4, analytical espressions for the self-energies could have been used [32]. However, the numerical technique presented here is more general: for example, it can be applied in the presence of a magnetic field.

As a first step, we consider A^C and decimate all the slabs from -1 backward to $-M+2$ (assuming $M > 2$). We define $d_1^{(0)} = A_{0,0}$, $d_2^{(0)} = A_{-1,-1}$, $a^{(0)} = A_{-1,0}$, $b^{(0)} = A_{0,-1}$. The generic iteration of index n ($n = 1, \ldots, M-2$) consists in eliminating the second last node from the matrix

$$\begin{pmatrix} \ddots & \ddots & & \\ \ddots & A_{-n-1,-n-1} & A_{-n-1,-n} & \\ & A_{-n,-n-1} & d_2^{(n-1)} & a^{(n-1)} \\ & & b^{(n-1)} & d_1^{(n-1)} \end{pmatrix} \tag{C.35}$$

with the equations

$$\begin{aligned} d_1^{(n)} &= d_1^{(n-1)} - b^{(n-1)} \left(d_2^{(n-1)}\right)^{-1} a^{(n-1)} , \\ d_2^{(n)} &= A_{-n-1,-n-1} - \\ &\quad - A_{-n-1,-n} \left(d_2^{(n-1)}\right)^{-1} A_{-n,-n-1} , \\ a^{(n)} &= -A_{-n-1,-n} \left(d_2^{(n-1)}\right)^{-1} a^{(n-1)} , \\ b^{(n)} &= -b^{(n-1)} \left(d_2^{(n-1)}\right)^{-1} A_{-n,-n-1} , \end{aligned} \tag{C.36}$$

which are simply an application of C.27. At the end, we obtain the renormalized A^L matrix

$$\tilde{A}^L = \begin{pmatrix} \ddots & \ddots & & & \\ \ddots & d_2^{(M-2)} & a^{(M-2)} & & \\ & b^{(M-2)} & d_1^{(M-2)} & A_{-M,-M+1} & \\ & & A_{-M+1,-M} & d_2^{(M-2)} & a^{(M-2)} \\ & & & b^{(M-2)} & d_1^{(M-2)} \end{pmatrix} . \tag{C.37}$$

As a second step, we consider $\tilde{A}^L$ and decimate all the even slabs (assuming $M > 1$). By using the formulas (again an application of C.27)

$$\begin{aligned}
\delta_1^{(0)} &= d_1^{(M-2)} - b^{(M-2)} \left(d_2^{(M-2)}\right)^{-1} a^{(M-2)} , \\
\delta_2^{(0)} &= \delta_1^{(0)} - A_{-M,-M+1} \left(d_2^{(M-2)}\right)^{-1} A_{-M+1,-M} , \\
\alpha^{(0)} &= -A_{-M,-M+1} \left(d_2^{(M-2)}\right)^{-1} a^{(M-2)} , \\
\beta^{(0)} &= -b^{(M-2)} \left(d_2^{(M-2)}\right)^{-1} A_{-M+1,-M} ,
\end{aligned} \tag{C.38}$$

we get a new renormalized A^L matrix,

$$\tilde{\tilde{A}}^L = \begin{pmatrix}
\ddots & \ddots & & & \\
\ddots & \delta_2^{(0)} & \alpha^{(0)} & & \\
 & \beta^{(0)} & \delta_2^{(0)} & \alpha^{(0)} & \\
 & & \beta^{(0)} & \delta_2^{(0)} & \alpha^{(0)} \\
 & & & \beta^{(0)} & \delta_1^{(0)}
\end{pmatrix} . \tag{C.39}$$

This matrix has the same structure as the one used in the Sancho-Rubio algorithm [24]. The generic iteration of index n ($n = 1, 2, \ldots$) of this algorithm actually consists in the decimation of the slabs with even indexes from the matrix

$$\begin{pmatrix}
\ddots & \ddots & & & \\
\ddots & \delta_2^{(n-1)} & \alpha^{(n-1)} & & \\
 & \beta^{(n-1)} & \delta_2^{(n-1)} & \alpha^{(n-1)} & \\
 & & \beta^{(n-1)} & \delta_2^{(n-1)} & \alpha^{(n-1)} \\
 & & & \beta^{(n-1)} & \delta_1^{(n-1)}
\end{pmatrix} , \tag{C.40}$$

by using the formulas (again from C.27)

$$\begin{aligned}
\delta_1^{(n)} &= \delta_1^{(n-1)} - \beta^{(n-1)} \left(\delta_2^{(n-1)}\right)^{-1} \alpha^{(n-1)} , \\
\delta_2^{(n)} &= \delta_2^{(n-1)} - \beta^{(n-1)} \left(\delta_2^{(n-1)}\right)^{-1} \alpha^{(n-1)} - \\
&\quad - \alpha^{(n-1)} \left(\delta_2^{(n-1)}\right)^{-1} \beta^{(n-1)} , \\
\alpha^{(n)} &= -\alpha^{(n-1)} \left(\delta_2^{(n-1)}\right)^{-1} \alpha^{(n-1)} , \\
\beta^{(n)} &= -\beta^{(n-1)} \left(\delta_2^{(n-1)}\right)^{-1} \beta^{(n-1)} ,
\end{aligned} \tag{C.41}$$

until convergence, i.e. until the coupling matrices $\alpha^{(n)}$ and $\beta^{(n)}$ become sufficiently small. At the end, we can approximate $g^r_{0,0} = (\delta_1^{(n)})^{-1}$, where n stands for the index of the last iteration.

Bibliography

[1] R. Saito, G. Dresselhaus, and M. S. Dresselhaus. *Physical Properties of Carbon Nanotubes*. Imperial College Press, 1998. [cited at p. 1, 5]

[2] K. S. Novoselov, A. K. Geim, S. V. Morozov, D. Jiang, Y. Zhang, S. V. Dubonos, I. V. Grigorieva, and A. A. Firsov. Electric field effect in atomically thin carbon films. *Science*, 306:666, 2004. [cited at p. 1]

[3] K. S. Novoselov, A. K. Geim, S. V. Morozov, D. Jiang, M. I. Katsnelson, I. V. Grigorieva, S. V. Dubonos, and A. A. Firsov. Two-dimensional gas of massless dirac fermions in graphene. *Nature*, 438:197, 2005. [cited at p. 2]

[4] Y. Zhang, Y.-W. Tan, H. L. Stormer, and P. Kim. Experimental observation of the quantum hall effect and berry's phase in graphene. *Nature*, 438:201, 2005. [cited at p. 2]

[5] C. Berger, Z. Song, X. Li, X. Wu, N. Brown, C. Naud, D. Mayou, T. Li, J. Hass, A. N. Marchenkov, E. H. Conrad, P. N. First, and W. A. de Heer. Electronic confinement and coherence in patterned epitaxial graphene. *Science*, 312:1191, 2006. [cited at p. 2]

[6] X. Li, Y. Zhu, W. Cai, M. Borysiak, B. Han, D. Chen, R. D. Piner, L. Colombo, and R. S. Ruoff. *Nano Lett.*, 9:4359, 2009. [cited at p. 2, 61]

[7] A. K. Geim and K. S. Novoselov. The rise of graphene. *Nature Materials*, 6:183, 2007. [cited at p. 2]

[8] M. C. Lemme, T. J. Echtermeyer, M. Baus, and H. Kurz. A graphene field-effect device. *IEEE Elec. Dev. Lett.*, 28:282, 2007. [cited at p. 4]

[9] X. Wang, Y. Ouyang, X. Li, H. Wang, J. Guo, and H. Dai. Room-temperature all-semiconducting sub-10-nm graphene nanoribbon field-effect transistors. *Phys. Rev. Lett.*, 100:206803, 2008. [cited at p. 4, 44]

[10] K. Nakada, M. Fujita, G. Dresselhaus, and M. S. Dresselhaus. Edge state in graphene ribbons: Nanometer size effect and edge shape dependence. *Phys. Rev. B*, 54:17954, 1996. [cited at p. 4]

[11] M. Y. Han, B. Özyilmaz, Y. Zhang, and P. Kim. Energy band-gap engineering of graphene nanoribbons. *Phys. Rev. Lett.*, 98:206805, 2007. [cited at p. 4]

[12] R. Balog, B. Jørgensen, L. Nilsson, M. Andersen, E. Rienks, M. Bianchi, M. Fanetti, E. Lægsgaard, A. Baraldi, S. Lizzit, Z. Sljivancanin, F. Besenbacher, B. Hammer, T. G. Pedersen, P. Hofmann, and L. Hornekær. *Nature Materials*, 9:315, 2010. [cited at p. 4, 54, 56, 58]

[13] F. Xia, D. B. Farmer, Y. Lin, and P. Avouris. *Nano Lett.*, 10:715, 2010. [cited at p. 4]

[14] F. Guinea, M. I. Katsnelson, and A. K. Geim. Energy gaps and a zero-field quantum hall effect in graphene by strain engineering. *Nature Physics*, 6:30, 2010. [cited at p. 4]

[15] Y. Ouyang, Y. Yoon, J. K. Fodor, and J. Guo. Comparison of performance limits for carbon nanoribbon and carbon nanotube transistors. *Appl. Phys. Lett.*, 89:203107, 2006. [cited at p. 5]

[16] G. Fiori and G. Iannaccone. Simulation of graphene nanoribbon field-effect transistors. *IEEE Elec. Dev. Lett.*, 28:760, 2007. [cited at p. 5]

[17] J. C. Slater and G. F. Koster. Simplified lcao method for the periodic potential problem. *Phys. Rev.*, 94:1498, 1954. [cited at p. 5]

[18] S. Datta. *Electronic Transport in Mesoscopic Systems*. Cambridge University Press, 1997. [cited at p. 6, 15, 17, 58, 62, 94]

[19] A. L. Fetter and J. D. Walecka. *Quantum theory of many-particle systems*. McGraw-Hill, 1971. [cited at p. 6]

[20] Y.-W. Son, M. L. Cohen, and S. G. Louie. Energy gaps in graphene nanoribbons. *Phys. Rev. Lett.*, 97:216803, 2006. [cited at p. 13, 14, 15, 61]

[21] D. Gunlycke and C. T. White. Tight-binding energy dispersions of armchair-edge graphene nanostrips. *Phys. Rev. B*, 77:115116, 2008. [cited at p. 14, 36, 37]

[22] W. Kohn and L. J. Sham. Self-consistent equations including exchange and correlation effects. *Phys. Rev.*, 140:A1133, 2007. [cited at p. 14]

[23] R. Lake, G. Klimeck, R. C. Bowen, and D. Jovanovic. Single and multiband modeling of quantum electron transport through layered semiconductor devices. *J. Appl. Phys.*, 81:7845, 1997. [cited at p. 15, 17, 88]

[24] M. P. Lopez Sancho, J. M. Lopez Sancho, and J. Rubio. Highly convergent schemes for the calculation of bulk and surface green functions. *J. Phys. F: Met. Phys.*, 15:851, 1985. [cited at p. 16, 62, 87, 95, 96]

[25] M. Brandbyge, J.-L. Mozos ans P. Ordejón, J. Taylor, and K. Stokbro. Density-functional method for nonequilibrium electron transport. *Phys. Rev. B*, 65:165401, 2002. [cited at p. 16]

[26] S. Poli, S. Reggiani, A. Gnudi, E. Gnani, and G. Baccarani. Computational study of the ultimate scaling limits of CNT tunneling devices. *IEEE Trans. Electron Devices*, 55:313, 2008. [cited at p. 17, 18]

[27] Y.-M. Lin, J. Appenzeller, J. Knoch, and P. Avouris. High-performance carbon nanotube field-effect transistor with tunable polarities. *IEEE Trans. on Nanotechnology*, 40:481, 2005. [cited at p. 22]

[28] J. Wang, E. Polizzi, and M. Lundstrom. A three-dimensional quantum simulation of silicon nanowire transistors with the effective-mass approximation. *J. Appl. Phys.*, 96:2192, 2004. [cited at p. 26]

[29] M. Luisier, A. Schenk, and W. Fichtner. Quantum transport in two- and three-dimensional nanoscale transistors: Coupled mode effects in the nonequilibrium Green's function formalism. *J. Appl. Phys.*, 100:043713, 2006. [cited at p. 26]

[30] J. Guo, S. Datta, M. Lundstrom, and M. P. Anantram. Towards multiscale modeling of carbon nanotube transistors. *Int. J. Mult. Comp. Eng.*, 2:257, 2004. [cited at p. 26]

[31] G. Fiori, G. Iannaccone, and G. Klimeck. Coupled mode space approach for the simulation of realistic carbon nanotube field-effect transistors. *IEEE Trans. Nanotech.*, 6:475, 2007. [cited at p. 26]

[32] P. Zhao and J. Guo. *J. Appl. Phys.*, 105:034503, 2009. [cited at p. 26, 33, 95]

[33] J. Appenzeller, Y. Lin, J. Knoch, Z. Chen, and P. Avouris. Comparing carbon nanotube transistors - the ideal choice: A novel tunneling device design. *IEEE Trans. Electron Devices*, 52:2568, 2005. [cited at p. 34, 43]

[34] C. Papadopoulos, A. Rakitin, J. Li, A. S. Vedeneev, and J. M. Xu. Electronic transport in Y-junction carbon nanotubes. *Phys. Rev. Lett.*, 85:3476, 2000. [cited at p. 35]

[35] G. Kim, S. B. Lee, H. Lee, and J. Ihm. Electron orbital valves made of multiply connected armchair carbon nanotubes with mirror-reflection symmetry: tight-binding study. *J. Phys.: Condens. Matter*, 19:026217, 2007. [cited at p. 35]

[36] Y. Yoon, G. Fiori, S. Hong, G. Iannaccone, and J. Guo. Performance comparison of graphene nanoribbon FETs with Schottky contacts and doped reservoirs. *IEEE Trans. Electron Devices*, 55:2314, 2008. [cited at p. 37, 44]

[37] P. Zhao, J. Chauhan, and J. Guo. Computational study of tunneling transistor based on graphene nanoribbon. *Nano Lett.*, 9:684, 2009. [cited at p. 44]

[38] Y. Yoon and J. Guo. Effect of edge roughness in graphene nanoribbon transistors. *Appl. Phys. Lett.*, 91:073103, 2007. [cited at p. 48]

[39] J. O. Sofo, A. S. Chaudhari, and G. D. Barber. *Phys. Rev. B*, 75:153401, 2007. [cited at p. 53]

[40] A. K. Singh and B. I. Yakobson. *Nano Lett.*, 9:1540, 2009. [cited at p. 53]

[41] D. C. Elias, R. R. Nair, T. M. G. Mohiuddin, S. V. Morozov, P. Blake, M. P. Halsall, A. C. Ferrari, D. W. Boukhvalov, M. I. Katsnelson, A. K. Geim, and K. S. Novoselov. *Science*, 323:610, 2009. [cited at p. 53]

[42] J. P. Robinson, H. Schomerus, L. Oroszlány, and V. I. Fal'ko. *Phys. Rev. Lett.*, 101:196803, 2008. [cited at p. 54, 55]

[43] J. Bang and K. J. Chang. *Phys. Rev. B*, 81:193412, 2010. [cited at p. 54, 55]

[44] D. A. Abanin, A. V. Shytov, and L. S. Levitov. *Phys. Rev. Lett.*, 105:086802, 2010. [cited at p. 54]

[45] D. Haberer, D. V. Vyalikh, S. Taioli, B. Dora, M. Farjam, J. Fink, D. Marchenko, T. Pichler, K. Ziegler, S. Simonucci, M. S. Dresselhaus, M. Knupfer, B. Büchner, and A. Grüneis. *Nano Lett.*, 10:3360, 2010. [cited at p. 54, 58, 79]

[46] T. G. Pedersen, C. Flindt, J. Pedersen, N. A. Mortensen, A.-P. Jauho, and K. Pedersen. *Phys. Rev. Lett.*, 100:136804, 2008. [cited at p. 54, 59]

[47] J. Bai, X. Zhong, S. Jiang, Y. Huang, and X. Duan. *Nature Nanotechnology*, 5:190, 2010. [cited at p. 54, 61]

[48] A. T. N'Diaye, S. Bleikamp, P. J. Feibelman, and T. Michely. *Phys. Rev. Lett.*, 97:215501, 2006. [cited at p. 56, 71, 72]

[49] V. M. Pereira, J. M. B. Lopes dos Santos, and A. H. Castro Neto. *Phys. Rev. B*, 77:115109, 2008. [cited at p. 59]

[50] R. Petersen, T. G. Pedersen, and A.-P. Jauho. *ACS Nano*, 5:523, 2011. [cited at p. 59]

[51] P. W. Anderson, D. J. Thouless, E. Abrahams, and D. S. Fisher. *Phys. Rev. B*, 22:3519, 1980. [cited at p. 62]

[52] T. Low, S. Hong, J. Appenzeller, S. Datta, and M. S. Lundstrom. *IEEE Trans. Elec. Dev.*, 56:1292, 2009. [cited at p. 62]

[53] P. A. Lee and T. V. Ramakrishnan. *Rev. Mod. Phys.*, 57:287, 1985. [cited at p. 63]

[54] D. Gunlycke, D. A. Areshkin, and C. T. White. *Appl. Phys. Lett.*, 90:142104, 2007. [cited at p. 65]

[55] T. Shen, Y. Q. Wu, M. A. Capano, L. P. Rokhinson, L. W. Engel, and P. D. Ye. *Appl. Phys. Lett.*, 93:122102, 2008. [cited at p. 65]

[56] A. L. Vázquez de Parga, F. Calleja, B. Borca, M. C. G. Passeggi Jr., J. J. Hinarejos, F. Guinea, and R. Miranda. *Phys. Rev. Lett.*, 100:056807, 2008. [cited at p. 71]

[57] G. Grosso, S. Moroni, and G. Pastori Parravicini. *Phys. Rev. B*, 40:12328, 1989. [cited at p. 92, 93]

Curriculum Vitae

Roberto Grassi was born in Cesena, Italy, in 1982. He received the M.S. (summa cum laude) in Electrical Engineering from the University of Bologna, Italy, in 2007. In the same year he joined the Advanced Research Center on Electronic Systems (ARCES) of the University of Bologna. In 2008 he started the Ph.D. program at the Department of Electronics, Computer Science and Systems (DEIS) of the University of Bologna. From October 2009 to September 2010 he was visiting scholar at the Network for Computational Nanotechnology, Purdue University, West Lafayette, IN (USA). He is in the field of numerical simulation of carbon-based devices.

List of Publications

Conference Publications

[1] R. Grassi, S. Poli, S. Reggiani, A. Gnudi, M. Rudan, and G. Baccarani, "Phonon-scattering effects in CNT-FETs with different dimensions and dielectric materials", 37-th European Solid-State Device Research Conference, Munich, Germany, September 2007.

[2] R. Grassi, S. Poli, E. Gnani, A. Gnudi, S. Reggiani, and G. Baccarani, "Tight-Binding and Effective-mass modeling of armchair carbon nanoribbon FETs", 9-th International Conference on Ultimate Integration on Silicon, Udine, Italy, March 2008.

[3] R. Grassi, A. Gnudi, E. Gnani, S. Reggiani, G. Cinacchi, and G. Baccarani, "Hierarchical modeling of carbon nanoribbon devices for CNR-FETs engineering", 66-th Device Research Conference, Santa Barbara, CA, June 2008.

[4] R. Grassi, A. Gnudi, S. Reggiani, E. Gnani, and G. Baccarani, "Simulation Study of Graphene Nanoribbon Tunneling Transistors Including Edge

Roughness Effects", 10-th International Conference on Ultimate Integration on Silicon, Aachen, Germany, March 2009.

[5] R. Grassi, A. Gnudi, E. Gnani, S. Reggiani, and G. Baccarani, "Mode Space Approach for Tight-Binding Transport Simulation in Graphene Nanoribbon FETs", 13-th International Workshop on Computational Electronics, Beijing, China, May 2009.

[6] I. Imperiale, R. Grassi, A. Gnudi, S. Reggiani, E. Gnani, and G. Baccarani, "Full-Quantum Calculations of Low-Field Channel Mobility in Graphene Nanoribbon FETs Including Acoustic Phonon Scattering and Edge Roughness Effects", 11-th International Conference on Ultimate Limits of Integration in Semiconductors, Glasgow, UK, March 2010.

Journal Publications

[1] R. Grassi, S. Poli, S. Reggiani, E. Gnani, A. Gnudi, and G. Baccarani, "Phonon-scattering effects in CNT-FETs with different dimensions and dielectric materials", Solid-State Electronics, vol. 52, Issue 9, p. 1329, 2008.

[2] R. Grassi, S. Poli, E. Gnani, A. Gnudi, S. Reggiani, and G. Baccarani, "Tight-binding and effective mass modeling of armchair graphene nanoribbon FETs", Solid-State Electronics, vol. 53, Issue 4, p. 462, 2009.

[3] R. Grassi, A. Gnudi, E. Gnani, S. Reggiani, and G. Baccarani, "An investigation of performance limits of conventional and tunneling graphene-based transistors", Journal of Computational Electronics, vol. 8, Issue 3, p. 441, 2009.

[4] R. Grassi, A. Gnudi, E. Gnani, S. Reggiani, and G. Baccarani, "Mode Space Approach for Tight-Binding Transport Simulation in Graphene Nanoribbon FETs", accepted for publication on IEEE Transactions on Nanotechnology.